Politecnico di Milano

Scuola di Ingegneria Industriale e dell'Informazione

Energy exchanges in one-dimensional flows of ideal and non-ideal gases

Relatore: Prof. Alberto Guardone
Relatore: Prof. Emile Touber

Tesi di Laurea di:
Luca Mancuso
Matricola: 833577

A.A. 2016-2017

Sommario

In questo lavoro vengono studiate le correnti monodimensionali di fluidi ideali e non ideali. Questi ultimi avvengono in una particolare regione termodinamica in cui la velocità del suono diminuisce attraverso una compressione isoentropica. Il modello termodinamico impiegato è quello del gas di van der Waals politropico con un elevato valore del calore specifico a volume costante, caratteristico di fluidi di elevata complessità molecolare.
Si mostra come per tali correnti monodimensionali, nell'ipotesi di piccole perturbazioni, profili di velocità o pressione inizialmente regolari tendano ad assumere un profilo a dente di sega, proprio come quanto accade nel caso della soluzione all'equazione di Burgers. Tuttavia, nel caso di fluidi non ideali in prossimità del punto critico, tale comportamento viene fortemente influenzato dal valore della derivata fondamentale della gas dinamica. La forma della soluzione asintotica è diversa a seconda della posizione dello stato termodinamico iniziale nel diagramma $p - \vartheta$. Si illustra, inoltre, come la particolare forma del profilo di velocità influenzi il modo in cui l'energia cinetica è redistribuita tra le varie scale. In particolare, lo spettro di energia cinetica risulta essere inversamente proporzionale al quadrato del numero d'onda. Il ruolo fondamentale è rivestito dalle onde d'urto—siano esse di compressione o di espansione—nel cui spessore l'energia cinetica viene dissipata.
Riducendo le equazioni di Navier-Stokes ad una sola dimensione e considerando inizialmente trascurabili gli effetti della viscosità e della conducibilità termica, è possibile studiare nel dettaglio gli scambi tra energia cinetica ed energia interna, che avvengono per mezzo della parte di dilatazione della velocità. Ancora una volta, lo stato termodinamico iniziale determinerà la frequenza e l'entità di tali scambi. In particolare, si illustra come una diversa equazione di stato del fluido modifichi i trasferimenti energetici, benché la medesima condizione iniziale venga imposta al flusso.
Si discute infine l'effetto della viscosità di volume, da cui dipende direttamente lo spessore delle onde d'urto e, di conseguenza, la forma dello spettro di energia cinetica. Per concludere, si mostra come gli stessi scambi tra energia cinetica ed energia interna siano influenzati dalla viscosità di volume.

Ringraziamenti

Vorrei innanzitutto ringraziare i miei genitori per aver sempre creduto in me, anche nei momenti più difficili. Grazie per le meravigliose opportunità che mi avete regalato e per avermi sostenuto durante i due anni e mezzo passati all'estero: non vi sarò mai abbastanza riconoscente. Vorrei inoltre esprimere tutta la mia gratitudine a ciascun membro della mia famiglia, in particolare a mia sorella e ai miei nonni.
Ringrazio il professor Emile Touber e il professor Alberto Guardone. Il primo per avermi trasmesso tanta passione e per avermi spinto ad un costante miglioramento durante tutto l'arco del soggiorno a Londra; il secondo per avermi dato la strepitosa occasione di svolgere ricerca in Inghilterra.
Ringrazio Cristina per essermi stata accanto, nonostante la lontananza ci separasse. Sei stata il punto di riferimento a cui ho costantemente guardato, vista anche l'enorme determinazione con cui affronti la vita e la gioia che ti contraddistingue.
Un ringraziamento speciale ai miei amici di sempre: Giorgio, che tante volte mi è stato da esempio e di cui ammiro l'estrema forza di volontà, Davide, per i tanti discorsi e i proficui scambi di idee, soprattutto durante i cinque mesi vissuti insieme, ed Antonio, semplicemente il mio migliore amico, per il suo grande cuore.
Negli anni di università ho conosciuto moltissime persone che mi hanno aiutato a crescere e ad allargare i miei orizzonti. Al Politecnico ho condiviso tanti momenti con Pietro e Marco, due amici meravigliosi e pieni di entusiasmo.
Durante l'esperienza in Francia ho invece avuto l'onore di fare parte di una seconda famiglia: un grazie a Francesco, Alessio, Lorenzo e Matteo per le tante risate che mi avete regalato durante i progetti insieme; grazie ad Antonio di cui condivido le aspirazioni; grazie a Paolo e ad Andrea per le cene, i viaggi e tanto tanto altro; grazie a Daniel per tutto l'affetto dimostrato e a Loris per l'infinita disponibilità. Infine ringrazio Anthea per la tanta fiducia riposta in me.

Contents

Introduction **11**

One-dimensional flows and fundamentals of non-classical gasdynamics 11

Thesis goal and outline 12

1 Governing equations and non-ideal gases thermodynamics **13**

1.1 The Navier-Stokes equations 13

1.1.1 Differential form of the Navier-Stokes equations 13

1.1.2 The transport equation for kinetic and internal energy 14

1.1.3 One-dimensional compressible Navier-Stokes equations 14

1.1.4 The transport equation for entropy 15

1.1.5 The Euler equations 16

1.2 Thermodynamics of non-ideal gases 16

1.2.1 The fundamental derivative of gasdynamics 17

1.2.2 Van der Waals gases 17

1.2.3 Non-ideal gases classification based on molecular complexity 19

2 The Burgers equation **21**

2.1 Theoretical background 21

2.1.1 Exact solution 21

2.1.2 Burgers inertial range 25

2.2 Numerical approach 26

2.2.1 Numerical estimation of the exact solution: validation 26

2.2.2 Numerical estimation of the exact solution: initial condition imposed . . . 27

2.2.3 The energy spectrum of the Burgers equation 29

3 Dynamic and spectral properties of one-dimensional ideal flows **35**

3.1 From the one-dimensional Navier-Stokes equations to the Burgers equation: theoretical background 35

3.2 `Compreal`: main features of the code 38

3.2.1 Numerical schemes and boundary conditions 38

3.2.2 How to build the input of the code 39

3.3 From the one-dimensional Navier-Stokes equations to the Burgers equation: inviscid numerical simulations 40

3.3.1 Velocity perturbation . . . 41
3.3.2 Thermodynamic perturbations . . . 47
3.3.3 Is the non-linear acoustics approximation justified? . . . 51
3.4 From the one-dimensional Navier-Stokes equations to the Burgers equation: viscous numerical simulations . . . 55

4 Dynamic and spectral properties of one-dimensional non-ideal flows 59
4.1 From the one-dimensional Navier-Stokes equations to the Burgers equation: theoretical background . . . 59
4.2 From the one-dimensional Navier-Stokes equations to the Burgers equation: inviscid numerical simulations . . . 62
4.2.1 Inviscid flow: dynamic and energetic features . . . 62
4.2.2 Formation time of the first shock wave . . . 81
4.2.3 Is the non-linear acoustics approximation justified? . . . 82
4.3 From the one-dimensional Navier-Stokes equations to the Burgers equation: viscous numerical simulations . . . 82

5 Energy exchanges in ideal and real gases 87
5.1 Inviscid flows . . . 87
5.2 Comparison of ideal and non-ideal gases behaviours . . . 95
5.3 Viscous flows . . . 100

Conclusion 109

List of Figures

1.1 $\Gamma = 1$ loci for different values of N 20
1.2 $\Gamma = 0$ loci for different values of N 20

2.1 Geometric solution to the minimisation of $Z(\xi)$ 23
2.2 A sequence of parabolas in contact with s and the corresponding velocity field . . 25
2.3 Comparison of analytic solution with estimated solution 28
2.4 Initial condition 28
2.5 Evolution in time of $u_0(x)$ for different values of μ 29
2.6 Evolution in time of $E(k,t)$ for different values of μ 30
2.7 Phase as a function of k for increasing viscosity, $t = 1000$ 31
2.8 Time decay of Δu and $E_{mean}(t)$ for $\mu = 10^{-5}$ 32
2.9 33

3.1 Test signal, sampling wave number $k_s = 512$ 40
3.2 Fast Fourier transform of the test signal 40
3.3 Inverse Fourier transform vs. original signal 41
3.4 Initial condition 42
3.5 *Simulation 1*: velocity evolution in the $x - t$ diagram for $t \in [0; 10]$ 43
3.6 *Simulation 1*: sectional views of the $x - t$ diagram 43
3.7 *Simulation 1*: energy spectrum times k^2 at $t = 1000$ 44
3.8 *Simulation 1*: mean spectrum as a function of time for $t \in [0; 1000]$ 45
3.9 *Simulation 1*: zoom on the *Burgers range* 46
3.10 Phase as a function of k at $t = 1000$ 46
3.11 $E(k,t)$ at $t = 10$ for different N_x 47
3.12 *Simulation 2A*: initial state in the $p - \vartheta$ diagram 48
3.13 *Simulation 2A*: velocity evolution in the $x - t$ diagram for $t \in [0; 10]$ 49
3.14 *Simulation 2A*: sectional views of the $x - t$ diagram 50
3.15 *Simulation 2A*: spectrum times k^2 at $t = 1000$ 50
3.16 *Simulation 2A*: mean spectrum as a function of time for $t \in [0; 1000]$ 51
3.17 *Simulation 2B*: initial state in the $p - \vartheta$ diagram 52
3.18 *Simulation 2B*: velocity evolution in the $x - t$ diagram for $t \in [0; 10]$ 52
3.19 *Simulation 2B*: velocity as a function of x at $t = 1.4$ 53

3.20 *Simulation 2B*: mean value of the inertial range as a function of time for $t \in [0; 1000]$ 53
3.21 *Simulation 1*: two-dimensional Fourier transform 54
3.22 *Simulation 1*: velocity evolution in the $x - t$ diagram for $t \in [0; 10]$ and $Re_b = 6000$ 56
3.23 Velocity as a function of time at $t = 10$ for different values of Re_b 56
3.24 Energy spectrum times k^2 at $t = 10$ for different values of Re_b 57

4.1 63
4.2 Initial thermodynamic conditions of the three simulations 64
4.3 65
4.4 *Simulation 1A*: $x - t$ diagram for $\Gamma_0 = 1$, the colour scale represents the velocity 66
4.5 *Simulation 1B*: $x - t$ diagram for $\Gamma_0 = -1$, the colour scale represents the velocity 66
4.6 *Simulation 1C*: $x - t$ diagram for $\Gamma_0 = 0$, the colour scale represents the velocity 67
4.7 *Simulation 1*: energy spectrum times k^2 as a function of k at $t = 1000$ 68
4.8 *Simulation 1*: time evolution of the mean spectrum $E_{mean}(t)$ 69
4.9 Phase as a function of k for $\Gamma_0 = 1$, $t = 1000$ 70
4.10 Phase as a function of k for $\Gamma_0 = -1$, $t = 1000$ 71
4.11 Phase as a function of k for $\Gamma_0 = 0$, $t = 1000$ 72
4.12 Λ contour from -10 to $+10$ for $\delta = 0.001$ 74
4.13 $x - t$ diagram for $\Gamma_0 = 0$ and $\Lambda_0 = 0$, the colour scale represents the velocity . . . 74
4.14 Velocity as a function of time at $t = 370$ 75
4.15 Mean spectrum as a function of time 75
4.16 Initial thermodynamic conditions of the three simulations 77
4.17 *Simulation 2A*: $x - t$ diagram for $\Gamma_0 = 1$, the colour scale represents the velocity 77
4.18 *Simulation 2B*: $x - t$ diagram for $\Gamma_0 = -1$, the colour scale represents the velocity 78
4.19 *Simulation 2C*: $x - t$ diagram for $\Gamma_0 = 0$, the colour scale represents the velocity 78
4.20 79
4.21 *Simulation 2*: time evolution of the mean spectrum $E_{mean}(t)$ 80
4.22 *Simulation 1A*: two-dimensional Fourier transform 82
4.23 *Simulation 1B*: two-dimensional Fourier transform 83
4.24 *Simulation 1C*: two-dimensional Fourier transform 83
4.25 *Simulation 1B*: velocity evolution in the $x-t$ diagram for $t \in [0; 10]$ and $Re_b = 6000$ 84
4.26 *Simulation 1B*: velocity as a function of time at $t = 10$ for different values of Re_b 84
4.27 *Simulation 1B*: energy spectrum times k^2 at $t = 10$ for different values of Re_b . . 85

5.1 Mean-kinetic-energy balance for an ideal gas, $t \in [0; 10]$ 89
5.2 Mean-internal-energy balance for an ideal gas, $t \in [0; 10]$ 90
5.3 Velocity perturbation for an ideal gas: mean internal energy vs. mean kinetic energy, $t \in [0; 1000]$ 90

5.4 Velocity perturbation for an ideal gas: mean total energy as a function of time . 91
5.5 Velocity perturbation for an ideal gas: mean kinetic energy as a function of time 92
5.6 Velocity perturbation for an ideal gas: mean internal energy as a function of time 92
5.7 Velocity perturbation for an ideal gas: mean kinetic energy as a function of time, $t \in [0;10]$ . . . 93
5.8 Velocity perturbation for an ideal gas: $x-t$ diagram of velocity, $t \in [0;10]$ 93
5.9 Thermodynamic perturbation for an ideal gas: mean internal energy vs. mean kinetic energy, $t \in [0;1000]$ . . . 94
5.10 Thermodynamic perturbation for an ideal gas: mean total energy as a function of time . . . 95
5.11 Initial velocity signal . . . 97
5.12 Initial spectra . . . 97
5.13 Initial state in the $\widehat{p}-\widehat{\vartheta}$ diagram . . . 98
5.14 Thermodynamic states at $t=\Delta t$ in the $\widehat{p}-\widehat{\vartheta}$ diagram . . . 99
5.15 Comparison of ideal and real gas: mean internal energy vs. mean kinetic energy, $t \in [0;10]$ . . . 100
5.16 Ideal and non-ideal gas comparison: mean total energy as a function of time . . . 101
5.17 Ideal and non-ideal gas comparison: specific-kinetic-energy-derivative *rms* . . . 101
5.18 Ideal and non-ideal gas comparison: specific-internal-energy-derivative *rms* . . . 102
5.19 Ideal and non-ideal gas comparison: specific-kinetic-energy *rms* . . . 102
5.20 Ideal and non-ideal gas comparison: specific-internal-energy *rms* . . . 103
5.21 Mean-kinetic-energy balance for an ideal gas: contribution of each term . . . 104
5.22 Mean-internal-energy balance for an ideal gas: contribution of each term . . . 105
5.23 Viscous term for different values of Re_b . . . 105
5.24 Mean-total-energy diminution in time for different values of Re_b . . . 106
5.25 Mean internal energy vs. mean kinetic energy for different values of Re_b, $t \in [0;10]$ 106
5.26 Mean kinetic energy as a function of time for different values of Re_b . . . 107
5.27 Mean internal energy as a function of time for different values of Re_b . . . 108

List of Tables

2.1 Parameters used to draw the analytic solution to the Burgers equation 27

2.2 Estimated solution: parameters employed. N_x number of points in space, N_t time instants 29

3.1 *Simulation 1*: parameters employed 42

3.2 Homoentropic perturbation for a perfect gas: parameters employed 49

3.3 Specific volume perturbation for a perfect gas: parameters employed 51

4.1 Velocity perturbation for a non-ideal gas: parameters employed 63

4.2 *Simulation 1*: formation times of the first shock wave 67

4.3 Homoentropic perturbation for a non-ideal gas: parameters employed 76

4.4 *Simulation 2*: formation times of the first shock wave 78

4.5 Formation times of the first shock wave 81

5.1 Comparison of ideal and real gas 96

Introduction

One-dimensional flows and fundamentals of non-classical gasdynamics

One-dimensional flows have been studied for a long time. In early fundamental studies, the one-dimensional Navier-Stokes equations were simplified into the Burgers equation, which describes a pressure-less gas dynamics. By applying the Cole-Hopf transform (see Cole [1] and Hopf [2]) to the viscous Burgers equation, the heat equation, whose solution is well-known, can be retrieved. Burgers [3] and Kida [4] proved that, for vanishing viscosity and large times, velocity profile evolves in a sawtooth. Given this peculiar feature, Gotoh [5] studied the energy spectrum of the asymptotic solution and found that it is inversely proportional to the square of the wave number. When viscosity is taken into account, a correction to the -2 exponent is needed. Chorin [6] provided a correction for a specific initial condition. He showed that high-frequency content is filtered out by increasing viscosity.
Indeed, these results can be extended to one-dimensional flows. In the framework of non-linear acoustics and ideal gases, Crighton [7], [8], [9] demonstrated the mapping between the one-dimensional Navier-Stokes equations and the Burgers equation.
When it comes to non-ideal gases–defined as deformable substances in which the speed of sound can decrease following an isentropic compression–the mapping was proved by Kluwick [10], [11] and Cramer and Kluwick [12]. In fact, in the dense-vapour regime, close to the liquid-vapour equilibrium, the classical ideal-gas assumption has to be reconsidered to account for the so-called non-ideal-gas effects. The early works of Bethe [13], Zel'dovich [14], Thompson [15] and Thompson and Lambrakis [16] discovered the conditions under which such non-classical effects can be observed in a single phase fluid. The governing parameter to address non-ideal gases is the fundamental derivative of gas dynamics, that was first defined by Bethe [13] as:

$$\Gamma(\vartheta, s) = \frac{\vartheta^3}{2c^2}\left(\frac{\partial p}{\partial \vartheta}\right)_s$$

where ϑ, s, p and c are the specific volume, the specific entropy, the pressure and the isentropic speed of sound of the fluid. Classical gas dynamics occurs when $\Gamma > 0$ (positive non-linearity); the isentropes in the $p - \vartheta$ diagram are convex and the only shock waves satisfying the entropy-increase condition are compression shock waves, whereas isentropic fans are of expansion type. When $\Gamma < 0$ (negative non-linearity), the isentropes are concave in the $p - \vartheta$ diagram and the only admissible shockwaves are rarefaction shockwaves, also called expansion shockwaves, and the isentropic fans are of compression type. The shock-formation process is much more complex for fluids featuring both $\Gamma > 0$ and $\Gamma < 0$ regions (mixed nonlinearity), where both compression and expansion shock waves can form. Other non-ideal phenomena are sonic shocks of compression and expansion type and double-sonic shocks, for which both the upstream and the downstream flows are sonic (see Cramer and Sen [17]). One-dimensional refraction properties of shocks in non-ideal gases were investigated by Alferez and Touber [18].
The sufficient condition for the $\Gamma < 0$ region to exist is that ratio between the specific heat capacity at constant volume and the gas constant, c_v/R, is greater than a critical value, which

depends on the equation of state. Gases that feature this region are often referred to as BZT fluids. Some molecules, such as siloxane, have attracted the interest of researchers (see Thompson and Lambrakis [16], Guardone and Argrow [19] and Guardone and Colonna [20]), since they exhibit high values of c_v/R.
In this work, the van der Waals polytropic equation of state has been used to model non-ideal gas behaviours. The complexity of the molecules constituting the gas is taken into account exclusively by the parameter c_v/R (Guardone and Argrow [19]).

Thesis goal and outline

This work aims at studying the main features of one-dimensional flows of ideal and non-ideal gases in the vicinity of the critical point. More specifically, the goal is to understand how velocity and thermodynamic perturbations evolve in time–depending on the equation of state that describes the fluid–and how this affects the way kinetic energy is redistributed across scales.
Furthermore, the reduction to one dimension gives easy access to internal- and kinetic-energy exchanges, which are driven by the pressure-dilatation term (when viscosity and heat exchange are neglected). Once more, the differences between ideal and non-ideal gases will be investigated. Eventually, the bulk viscosity, that is often assumed to be null, is taken into account. The objective is to assess how it modifies the kinetic-internal energy transfers.

This thesis is organised as follows. In chapter 1 the governing equations are briefly recalled and the thermodynamics of non-ideal gases is introduced, notably, the fundamental derivative and the van der Waals equation of state.
Chapter 2 addresses the Burgers equation. Firstly, major theoretical results (see Burgers [3], Kida [4] and Gotoh [5]) are detailed. Then, from a given initial condition, a numerical estimation of the exact solution is performed. The value of viscosity is showed to affect the evolution of the velocity profile, as well as the way kinetic energy is redistributed across scales.
Chapter 3 focuses on one-dimensional flows of ideal gases. In the first instance, the mapping between the Navier-Stokes equations and the Burgers equation–under the hypothesis of small perturbation–is proved theoretically (see Crigthon [7] and Karpman [21]). Consequently, simulations with different initial conditions are carried out to verify this statement. Indeed, the velocity profile features a peculiar shape, in the same way as the solution to the Burgers equation. The energy spectrum (as well as the phase spectrum) is seen to be strongly affected by shock waves. The last section is dedicated to bulk viscosity, which determines the thickness of the shock waves occurring inside the domain, hence, the energy spectrum shape.
Chapter 4 pivots on one-dimensional flows of non-ideal gases. Theoretical results and simulations highlight the role of the fundamental derivative of gasdynamics. Indeed, it is shown to determine the velocity-profile shape at large times, in accordance with Kluwick [10]. The way kinetic energy is redistributed across scales is addressed for several initial conditions. Furthermore, the properties of a peculiar point on the thermodynamic diagram are shown. The last section is dedicated to bulk viscosity.
Eventually, in chapter 5 the energy exchanges between kinetic and internal energy are investigated, in particular, ideal and non-ideal gas behaviours are compared. In addition, bulk viscosity is seen to affect the kinetic-internal energy transfers.

Part 1

Governing equations and non-ideal gases thermodynamics

In this first chapter, the governing equations of fluid dynamics are recalled; the one-dimensional compressible version will be dealt with in detail since it represents the basic analytic tool to study the exchanges between internal and kinetic energy. Moreover, section 1.2 briefly summarises the basic thermodynamic concepts suitable to describe non-ideal gases behaviour.

1.1 The Navier-Stokes equations

1.1.1 Differential form of the Navier-Stokes equations

The Navier-Stokes equations state the conservation of mass, momentum and total energy for a generic flow under the hypothesis that the fluid is a continuum, i.e. the geometric length scale is much bigger than a suitable characteristic dimension of the fluid: the mean free path. These conservation laws can be expressed either in an integral or in a differential form. The differential form of the Navier-Stokes equations necessitates additional hypotheses, namely the derivability of the density, pressure, velocity and temperature fields. It means that no shocks nor slip lines are allowed inside the domain for the differential equations to stand valid:

$$\begin{cases} \dfrac{\partial \rho}{\partial t} + \operatorname{div}(\rho \boldsymbol{u}) = 0 \\ \dfrac{\partial \rho \boldsymbol{u}}{\partial t} + \operatorname{div}(\rho \boldsymbol{u} \otimes \boldsymbol{u}) = \operatorname{div}[-p\boldsymbol{I} + \boldsymbol{\Pi}] + \rho \boldsymbol{g} \\ \dfrac{\partial \rho e_t}{\partial t} + \operatorname{div}(\rho e_t \boldsymbol{u}) = \operatorname{div}[-p\boldsymbol{u} + \boldsymbol{\Pi}\,\boldsymbol{u} + k\,\mathbf{grad}(T)] + \rho \boldsymbol{g} \cdot \boldsymbol{u} \end{cases} \tag{1.1}$$

where Π is the viscous stress tensor and $k = k(p,T)$ the thermal conductivity. The viscous stress tensor could be written as follows:

$$\boldsymbol{\Pi} = 2\mu \boldsymbol{D}^{\bullet} + \mu_b \operatorname{div}(\boldsymbol{u})\, \boldsymbol{I} \tag{1.2}$$

where:

$$\boldsymbol{D}^{\bullet} = \boldsymbol{D} - \frac{1}{3}\operatorname{Tr}(\boldsymbol{D})\, \boldsymbol{I} \tag{1.3}$$

and $\boldsymbol{D} = \left(\mathbf{grad}(\boldsymbol{u}) + \mathbf{grad}(\boldsymbol{u})^T\right)/2$ is the deformation tensor, $\mu = \mu(p,T)$ is the shear viscosity and $\mu_b = \mu_b(p,T)$ is the bulk viscosity. Indeed, the viscous stress tensor (1.2) has two contributions: shear and bulk viscosity. Any fluid obeying the above relationship for the viscous stress tensor is said to be Newtonian. Thermodynamics is based on the fundamental assumption of

local thermodynamic equilibrium: the time of motion is much higher than the relaxation time, which the time required for a quantity (e.g., specific volume, pressure, temperature) to regain its equilibrium after a disturbance.

1.1.2 The transport equation for kinetic and internal energy

One can write the transport equation for kinetic energy $e_k = \boldsymbol{u}^2/2$ by pre-multiplying the momentum equation by $\boldsymbol{u}$:

$$\boldsymbol{u} \cdot \frac{\partial \rho \boldsymbol{u}}{\partial t} + \boldsymbol{u} \cdot \operatorname{div}(\rho \boldsymbol{u} \otimes \boldsymbol{u}) = \boldsymbol{u} \cdot \operatorname{div}[-p\boldsymbol{I} + \boldsymbol{\Pi}] + \rho \boldsymbol{g} \cdot \boldsymbol{u},$$

which can be recast as follows:

$$\frac{\partial(\rho e_k)}{\partial t} + \operatorname{div}(\rho e_k \boldsymbol{u}) = \boldsymbol{u} \cdot \operatorname{div}[-p\boldsymbol{I} + \boldsymbol{\Pi}] + \rho \boldsymbol{g} \cdot \boldsymbol{u}. \tag{1.4}$$

The difference between the energy equation of system (1.1) and equation (1.4) yields the transport equation for the specific internal energy e:

$$\frac{\partial \rho e}{\partial t} + \operatorname{div}(\rho e \boldsymbol{u}) = -p \operatorname{div}(\boldsymbol{u}) + \boldsymbol{\Pi} : \mathbf{grad}(\boldsymbol{u}) + \operatorname{div}(k\, \mathbf{grad}(T)). \tag{1.5}$$

Equation 1.5 is none other than the first law of thermodynamics, where:

- The left-hand side term is the variation of internal energy;
- The first and second term on the right-hand side add up to give the work;
- The last term on the right-hand side is the heat exchange.

The viscous stress tensor $\boldsymbol{\Pi}$ could be expanded in its two contributions:

$$\frac{\partial \rho e}{\partial t} + \operatorname{div}(\rho e \boldsymbol{u}) = -p \operatorname{div}(\boldsymbol{u}) + [2\mu \boldsymbol{D}^{\bullet} + \mu_b \operatorname{div}(\boldsymbol{u})\, \boldsymbol{I}] : \mathbf{grad}(\boldsymbol{u}) + \operatorname{div}(k\, \mathbf{grad} T). \tag{1.6}$$

1.1.3 One-dimensional compressible Navier-Stokes equations

In one dimension, the velocity vector $\boldsymbol{u} = (u, v, w)$ reduces to $\boldsymbol{u} = (u, 0, 0)$; furthermore, $\partial u/\partial y = \partial u/\partial z = 0$ and $\partial T/\partial y = \partial T/\partial z = 0$. System (1.1) thus becomes:

$$\begin{cases} \dfrac{\partial \rho}{\partial t} + \dfrac{\partial \rho u}{\partial x} = 0 \\ \dfrac{\partial \rho u}{\partial t} + u\dfrac{\partial \rho u}{\partial x} + \rho u \dfrac{\partial u}{\partial x} = -\dfrac{\partial p}{\partial x} + \left(\dfrac{4}{3}\mu + \mu_b\right) \dfrac{\partial^2 u}{\partial x^2} \\ \dfrac{\partial \rho e_t}{\partial t} + \dfrac{\partial}{\partial x}(\rho e_t u) = -\dfrac{\partial p u}{\partial x} + \left(\dfrac{4}{3}\mu + \mu_b\right) \dfrac{\partial}{\partial x}\left(u \dfrac{\partial u}{\partial x}\right) + \dfrac{\partial}{\partial x}\left(k \dfrac{\partial T}{\partial x}\right) \end{cases} \tag{1.7}$$

The transport equation for the specific kinetic energy becomes:

$$\frac{\partial \rho e_k}{\partial t} + \frac{\partial}{\partial x}\left(\rho e_k u\right) = -u\frac{\partial p}{\partial x} + \left(\frac{4}{3}\mu + \mu_b\right) u\frac{\partial^2 u}{\partial x^2}, \tag{1.8}$$

whereas the transport equation for the specific internal energy is:

$$\frac{\partial \rho e}{\partial t} + \frac{\partial}{\partial x}\left(\rho e u\right) = -p\frac{\partial u}{\partial x} + \left(\frac{4}{3}\mu + \mu_b\right)\left(\frac{\partial u}{\partial x}\right)^2 + \frac{\partial}{\partial x}\left(k\frac{\partial T}{\partial x}\right). \tag{1.9}$$

1.1.4 The transport equation for entropy

Equation (1.5) can be recast in terms of entropy. It is well-known from the Gibbs equation that states:

$$\rho\frac{De}{Dt} - \frac{p}{\rho}\frac{D\rho}{Dt} = \rho T\frac{Ds}{Dt}. \tag{1.10}$$

If the internal energy equation (1.6) is rewritten as follows:

$$\rho\frac{De}{Dt} + p\,\mathrm{div}(\boldsymbol{u}) = \mathrm{div}\left(k\,\mathbf{grad}(T)\right) + \Phi \tag{1.11}$$

where:

$$\Phi = \boldsymbol{\Pi} : \mathbf{grad}(\boldsymbol{u}),$$

then, by substitution of the continuity equation into (1.11), one infers:

$$\rho\frac{De}{Dt} - \frac{p}{\rho}\frac{D\rho}{Dt} = \mathrm{div}\left(k\,\mathbf{grad}(T)\right) + \Phi \tag{1.12}$$

and finally, from equations (1.10) and (1.12):

$$\rho T\frac{Ds}{Dt} = \mathrm{div}\left(k\,\mathbf{grad}(T)\right) + \Phi \tag{1.13}$$

which in one-dimension becomes:

$$\rho T\left(\frac{\partial s}{\partial t} + u\frac{\partial s}{\partial x}\right) = \left(\frac{4}{3}\mu + \mu_b\right)\left(\frac{\partial u}{\partial x}\right)^2 + \frac{\partial}{\partial x}\left(k\frac{\partial T}{\partial x}\right). \tag{1.14}$$

1.1.5 The Euler equations

When viscosity and heat exchange are neglected. The governing equations reduce according to the Euler equations:

$$\begin{cases} \dfrac{\partial \rho}{\partial t} + \operatorname{div}(\rho \boldsymbol{u}) = 0 \\ \dfrac{\partial \rho \boldsymbol{u}}{\partial t} + \operatorname{div}(\rho \boldsymbol{u} \otimes \boldsymbol{u} + p\boldsymbol{I}) = 0 \\ \dfrac{\partial \rho e_t}{\partial t} + \operatorname{div}[(\rho e_t + p)\,\boldsymbol{u}] = 0 \end{cases} \tag{1.15}$$

in one dimension, they reduce to:

$$\begin{cases} \dfrac{\partial \rho}{\partial t} + \dfrac{\partial \rho u}{\partial x} = 0 \\ \dfrac{\partial \rho u}{\partial t} + u\dfrac{\partial \rho u}{\partial x} + \rho u \dfrac{\partial u}{\partial x} + \dfrac{\partial p}{\partial x} = 0 \\ \dfrac{\partial \rho e_t}{\partial t} + \dfrac{\partial}{\partial x}(\rho e_t u) + \dfrac{\partial p u}{\partial x} = 0 \end{cases} \tag{1.16}$$

From equations (1.8) and (1.9), the kinetic and internal energy equations for an inviscid flow are simply retrieved:

$$\frac{\partial \rho e_k}{\partial t} + \frac{\partial}{\partial x}(\rho e_k u) + u\frac{\partial p}{\partial x} = 0 \tag{1.17}$$

and:

$$\frac{\partial \rho e}{\partial t} + \frac{\partial}{\partial x}(\rho e u) + p\frac{\partial u}{\partial x} = 0 \tag{1.18}$$

Shock waves could indeed occur. The computation of a flow through a shock is a complex task since all the variables undergo a sharp change. The Euler equations can't be used to model a flow where discontinuities appear, unless one uses a shock-capturing scheme, which adds an artificial dissipative contribution to the inviscid model. `Compreal`, indeed, has a defined shock-capturing scheme.

1.2 Thermodynamics of non-ideal gases

This section firstly introduces the fundamental derivative of gasdynamics, referred to as Γ. In non-ideal gases, expansion shock waves may appear inside a narrow region of the thermodynamic diagram where Γ is negative. Then, the van der Waals equation of state is used as a simple model that accounts for non-ideal gas behaviours.

1.2.1 The fundamental derivative of gasdynamics

The fundamental derivative–which is the governing parameter to be used to address non-classical gasdynamics–was first introduced by Hayes [22]:

$$\Gamma(\vartheta, s) = \frac{\vartheta^3}{2c^2}\left(\frac{\partial^2 p}{\partial \vartheta^2}\right)_s = \frac{1}{c}\left(\frac{\partial \rho c}{\partial \rho}\right)_s \tag{1.19}$$

where ρ, ϑ, s, p and c are the density, the specific volume, the specific entropy, the pressure and the isentropic speed of sound, which is defined as:

$$c^2(\vartheta, p) = -\vartheta^2\left(\frac{\partial p}{\partial \vartheta}\right)_s. \tag{1.20}$$

The square of the speed of sound defines the slope of the tangent to the isentrope in the $p-\vartheta$ diagram.
As pointed out by Bethe [13] and Thompson [15], the fundamental derivative is positive (positive nonlinearity) for classical gasdynamics: the isentropes in the $p-\vartheta$ diagram are convex, the only shockwaves satisfying the entropy-increase condition are compression shockwaves; on the contrary, when $\Gamma < 0$ (negative nonlinearity), the only admissible shockwaves are of expansion type. These pioneering works showed that a small region where $\Gamma < 0$–also referred to as BZT region–could exist in the vapour region surrounding the thermodynamic critical point. A sufficient condition of existence is that the ratio between the specific heat capacity at constant volume and the gas constant c_v/R is greater than a critical value which depends on the equation of state.
This work often refers to dense gases, for which $c_v/R \to \infty$. It is well-known that, in this case, the isentropes converge towards the isotherms in the $p-\vartheta$ diagram. Indeed, as showed by Bethe [13] and Thompson and Lambrakis [16], one could write:

$$\left(\frac{\partial p}{\partial \vartheta}\right)_s = \left(\frac{\partial p}{\partial \vartheta}\right)_T - \frac{T}{R}\frac{R}{c_v}\left(\frac{\partial p}{\partial T}\right)_\vartheta^2. \tag{1.21}$$

When $c_v/R \to \infty$, its inverse goes to zero thus justifying the convergence of the isentropes towards the isotherms.

1.2.2 Van der Waals gases

The van der Waals model (see [23]) provides a simple correction to the ideal gas equation of state which becomes:

$$p(T, \vartheta) = \frac{RT}{\vartheta - b} - \frac{a}{\vartheta^2}. \tag{1.22}$$

The corrections concern the molecules, which are not anymore considered as point-wise particles, and the existence of intermolecurlar forces. The thermal equation of state $p(T, \vartheta)$ and the caloric equation $e(T, \vartheta)$ characterise the van der Waals gases. These two equations of state are not fully independent and should satisfy the consistency condition as found by Callen [23]:

$$\left(\frac{\partial e}{\partial \vartheta}\right)_T = T\left(\frac{\partial p}{\partial T}\right)_\vartheta - p(T, \vartheta). \tag{1.23}$$

Therefore, the internal energy becomes:

$$e(T,\vartheta) = \phi(T) - \frac{a}{\vartheta}. \tag{1.24}$$

Despite quantitative inaccuracies, this trivial model allows to assess non-ideal features from a qualitative point of view. To this end, the speed of sound c and the fundamental derivative Γ are computed for polytropic van der Waals gases, i.e. a simplified case where the specific heat capacity is assumed to be constant (see Guardone and Vigevano [24] and Guardone and Colonna [20]). By substitution of (1.21) into (1.20) and using equation of state (1.22), the speed of sound for a polytropic van der Waals gas is:

$$c^2(T,\vartheta) = \left[RT\left(1+\frac{R}{c_v}\right)\left(\frac{\vartheta}{\vartheta-b}\right)^2 - \frac{2a}{\vartheta^2}\right]. \tag{1.25}$$

The second derivative in equation (1.19) is computed from the general expression given by Thompson and Lambrakis [25] where c_v is assumed to be constant:

$$\left(\frac{\partial^2 p}{\partial \vartheta^2}\right)_s = \left(\frac{\partial^2 p}{\partial \vartheta^2}\right)_T - \frac{3T}{c_v}\left(\frac{\partial p}{\partial T}\right)_\vartheta \frac{\partial^2 p}{\partial \vartheta \partial T} + \frac{T}{c_v^2}\left(\frac{\partial p}{\partial T}\right)_\vartheta^3 \tag{1.26}$$

therefore, one easily gets the expression of the fundamental derivative as a function of pressure and specific volume:

$$\Gamma(p,\vartheta) = \frac{(1+\delta)(2+\delta)\dfrac{p+a/\vartheta^2}{(\vartheta-b)^2} - \dfrac{6a}{\vartheta^4}}{2(1+\delta)\dfrac{p+a/\vartheta^2}{\vartheta(\vartheta-b)} - \dfrac{4a}{\vartheta^4}} \tag{1.27}$$

where $\delta = R/c_v$.
It is common practice to normalise thermodynamic quantities by their respective value at the critical point. In the case of a polytropic van der Waals gas, the critical point coordinates are:

$$p_C = \frac{a}{27b^2}, \quad \vartheta_C = 3b, \quad T_C = \frac{8a}{27Rb} \tag{1.28}$$

and the reduced quantities are defined as:

$$\widehat{p} = \frac{p}{p_C}, \quad \widehat{\vartheta} = \frac{\vartheta}{\vartheta_C}, \quad \widehat{T} = \frac{T}{T_C}, \quad \widehat{e} = \frac{e}{p_C\vartheta_C}, \quad \widehat{c}^2 = \frac{c^2}{p_C\vartheta_C}. \tag{1.29}$$

The two equations of state take the following form:

$$\begin{cases} \widehat{p} = \dfrac{8\widehat{T}}{3\widehat{\vartheta}-1} - \dfrac{3}{\vartheta^2} \\ \widehat{e} = \dfrac{8}{3}\dfrac{\widehat{T}}{\delta} - \dfrac{3}{\vartheta} \end{cases} \tag{1.30}$$

The reduced speed of sound is:

$$\widehat{c}^2(\widehat{T},\widehat{\vartheta}) = \frac{24(\delta+1)\widehat{T}\widehat{\vartheta}^2}{(3\widehat{\vartheta}-1)^2} - \frac{6}{\widehat{\vartheta}} \tag{1.31}$$

and the fundamental derivative of gasdynamics is written as a function of the reduced temperature and specific volume:

$$\Gamma(\widehat{T},\widehat{\vartheta}) = \frac{\frac{1}{2}(1+\delta)(2+\delta)\frac{3\widehat{T}\widehat{\vartheta}}{(3\widehat{\vartheta}-1)^3} - \frac{3}{8\widehat{\vartheta}^3}}{(1+\delta)\frac{\widehat{T}}{(3\widehat{\vartheta}-1)^2} - \frac{1}{4\widehat{\vartheta}^3}}. \tag{1.32}$$

It should be noted that at the critical point, for $\delta \to 0$, Γ is an indeterminate form (0/0). More precisely, Guardone and Nannan ([26]) showed that Γ diverges at the critical point for infinite dense gases.
By manipulating the last expression, it is possible to visualise that region in the $\widehat{p}-\widehat{\vartheta}$ diagram where Γ is negative and strongly non-ideal behaviours are observed, such as expansion shock waves, compression fans or double-sonic shocks. Furthermore, for the van der Waals equation of state, the *Bethe - Zel'dovich - Thompson* (BZT) region exists for values of δ smaller than $1/16,66$ (see Thompson and Lambrakis [16]).

1.2.3 Non-ideal gases classification based on molecular complexity

The molecular complexity as the number of the active degrees of freedom of a molecule N, whose value could be non-integer. Each fully activated degree of freedom contributes $R/2$ to the specific heat at constant volume c_v. Thus, δ could be easily related to N, namely:

$$\delta = \frac{2}{N}. \tag{1.33}$$

Eventually, the existence of expansion shock waves is linked to the value of N. Indeed, for van der Waals gases, there exists two relevant values of molecular complexity:

1. $N \simeq 7.57$: the $\Gamma = 1$ loci reduces to a point in the $\widehat{p}-\widehat{\vartheta}$ diagram (see Kluwick [27]). For *low-molecular-complexity* fluids (LMC) Γ always exceeds unity, whereas *high-molecular-complexity* fluids (HMC) could show $\Gamma < 1$. When the fundamental derivative takes a value below unity, the speed of sound decreases for an isentropic compression, nevertheless expansion shockwaves do not appear since the increase in local velocity compensate for this unusual effect (see Thompson [28]). Figure 1.2 shows the $\Gamma = 1$ contours for different values of molecular complexity;

2. $N \simeq 33.33$: the $\Gamma = 0$ loci reduces to a point in the $\widehat{p}-\widehat{\vartheta}$ diagram. For $N > 33.33$ a BZT region appears. Figure 1.2 shows the $\Gamma = 0$ contours for different values of molecular complexity.

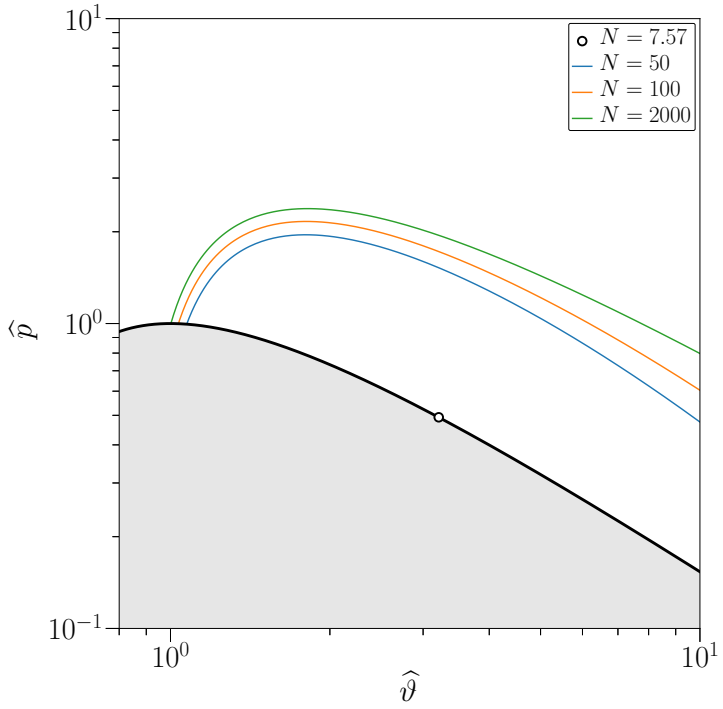

Figure 1.1: $\Gamma = 1$ loci for different values of N

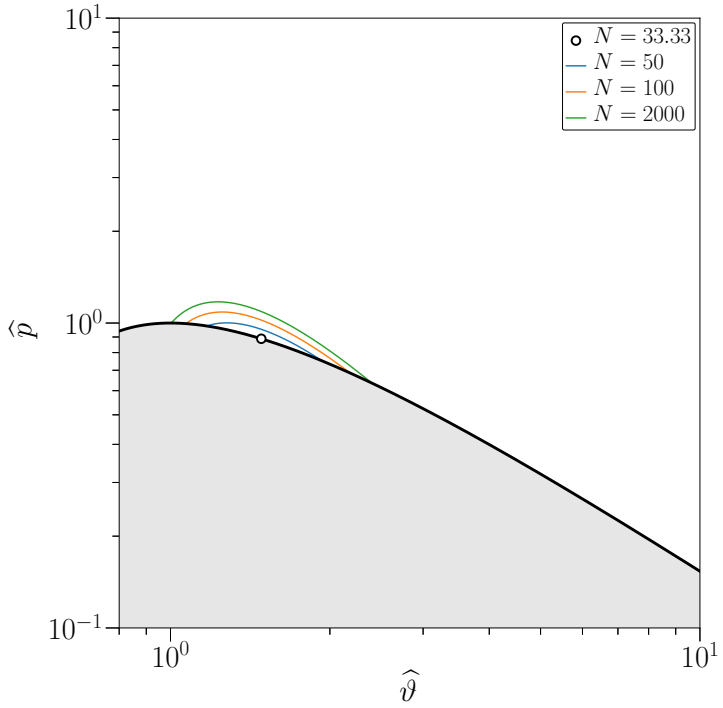

Figure 1.2: $\Gamma = 0$ loci for different values of N

Part 2

The Burgers equation

Historically, the Burgers equation was introduced as a one-dimensional model of the Navier-Stokes turbulence (as suggested by [5]). Indeed, this equation has the same quadratic non-linearity (also referred to as advective non-linearity) as the Navier-Stokes equation that is balanced by a diffusive term. Nevertheless, it describes a pressure-less gasdynamics. This model has been deeply studied over the years and it is crucial to understand the mechanism through which energy is redistributed across scales and the properties of the energy spectrum.
The one-dimensional Burgers equation is:

$$\frac{\partial u}{\partial t} + u\frac{\partial u}{\partial x} = \mu\frac{\partial^2 u}{\partial x^2} \tag{2.1}$$

where μ is the viscosity. This chapter issues the theoretical background of the Burgers equation (section 2.1). Not only how to retrieve the analytical solution is thoroughly described, but also its asymptotic spectral features are shown. These tools constitute the foundation for a numerical approach, which is the topic of section 2.2.

2.1 Theoretical background

This section provides the analytic approach to the viscous Burgers equation. It consists of two parts: the first focuses on how to retrieve an exact solution from the partial differential equation; the second part focuses on the asymptotic energy spectrum.

2.1.1 Exact solution

The exact solution was independently found by Cole [1] and Hopf [2] thanks to the famous Cole-Hopf transformation. They show that the viscous Burgers equation:

$$\frac{\partial u}{\partial t} + u\frac{\partial u}{\partial x} = \mu\frac{\partial^2 u}{\partial x^2} \tag{2.2}$$

can be rewritten as the heat equation, under the hypothesis that the velocity $u(x,t)$ is continuous and twice differentiable in space, and that the initial condition $u(x,0) = u_0(x)$ is integrable.
Indeed, one can recast equation(2.2) in the form:

$$u_t = \left(\mu u_x - \frac{u^2}{2}\right)_x \tag{2.3}$$

where subscripts $(\cdot)_x$ and $(\cdot)_t$ indicate the derivatives with respect to x and t respectively. If we introduce into equation (2.3) the dependent variable $\varphi = \varphi(x,t)$, defined as:

$$\varphi = -\frac{1}{2\mu}\exp\left\{\int_0^x u(x,t)\mathrm{dx}\right\} \tag{2.4}$$

whose inverse is:

$$u = -2\mu(\log\varphi)_x = -2\mu\left(\frac{\varphi_x}{\varphi}\right) \tag{2.5}$$

then, equation (2.3) becomes:

$$-2\mu\left(\log\varphi\right)_{xt} = -2\mu\left(\log\varphi\right)_{tx} = -2\mu\left(\frac{\varphi_t}{\varphi}\right)_x = -2\mu^2\left(\frac{\varphi_{xx}}{\varphi}\right)_x \tag{2.6}$$

when swapping the space and time derivatives, assuming $u \in \mathscr{C}^2$. The right-hand-side term is the result of the following manipulation:

$$\begin{aligned}&\left[\mu\left(-2\mu(\log\varphi)_x\right)_x - \frac{1}{2}\left(-2\mu(\log\varphi)_x\right)^2\right]_x = -2\mu^2\left[\left(\frac{\varphi_x}{\varphi}\right)_x + \left(\frac{\varphi_x}{\varphi}\right)^2\right]_x = \\ &= -2\mu^2\left[\frac{\varphi_{xx}\varphi - \varphi_x^2}{\varphi^2} + \left(\frac{\varphi_x}{\varphi}\right)^2\right]_x = -2\mu^2\left(\frac{\varphi_{xx}}{\varphi}\right)_x.\end{aligned} \tag{2.7}$$

By integration of (2.6), one gets:

$$\varphi_t = \mu\varphi_{xx} + C(t)\varphi. \tag{2.8}$$

Introducing the new dependent variable:

$$\overline{\varphi} = \varphi\exp\left\{\int_0^{+\infty} -C\mathrm{dt}\right\}, \tag{2.9}$$

one finally obtains the heat equation:

$$\overline{\varphi}_t = \mu\overline{\varphi}_{xx} \tag{2.10}$$

whose solution is well-known. Indeed, the solution to the heat equation combined with the inverse Cole-Hopf transform–as suggested among others by Burgers [3]–gives the exact solution to the original equation (2.2):

$$u(x,t) = \frac{\displaystyle\int_{-\infty}^{+\infty}\frac{x-\xi}{t}\exp\left[-\frac{1}{2\mu}\left\{\frac{(x-\xi)^2}{2t} - \int_0^{\xi}a(\xi_1)\mathrm{d}\xi_1\right\}\right]\mathrm{d}\xi}{\displaystyle\int_{-\infty}^{+\infty}\exp\left[-\frac{1}{2\mu}\left\{\frac{(x-\xi)^2}{2t} - \int_0^{\xi}a(\xi_1)\mathrm{d}\xi_1\right\}\right]\mathrm{d}\xi} \tag{2.11}$$

where: $a(\xi) = -u_0(\xi)$.
For vanishing viscosity, i.e. $\mu \to 0$ (or alternatively $Re \to +\infty$), the most important contribution

to the integral will come from the immediate neighbourhood of the point ξ_m, which, for a fixed t and x gives the absolute minimum of expression:

$$Z(\xi) = \frac{(x-\xi)^2}{2t} - \int_0^{\xi} a(\xi')\mathrm{d}\xi'. \tag{2.12}$$

Then, the solution for vanishing viscosity will be expressed as follows:

$$\lim_{\mu \to 0} u(x,t) = \frac{x - \xi_m}{t}. \tag{2.13}$$

The solution in the form of (2.11) is not always uniquely determined, however there exists an unambiguous limit for $\mu \to 0$ (or alternatively $Re \to +\infty$), obtained from the absolute minimum condition for (2.12).
In [3], Burgers showed that the point that minimises expression (2.12)–also referred to as ξ_m–can be found by means of a geometrical method. To this end, two curves are introduced:

$$s(\xi) = \int_0^{\xi} a(\xi')\mathrm{d}\xi',$$
$$S(\xi) = \frac{(\xi - x)^2}{2t} + C.$$

The first contains a representation of the initial data, whereas the second is a parabola, whose axis–the line $x = x'$–changes at different locations x and times t.
It is convenient to start with a large positive C, then C is progressively decreased until the two curves touch one another. The abscissa of the point of contact determines ξ_m at a certain t and x (see figure 2.1).

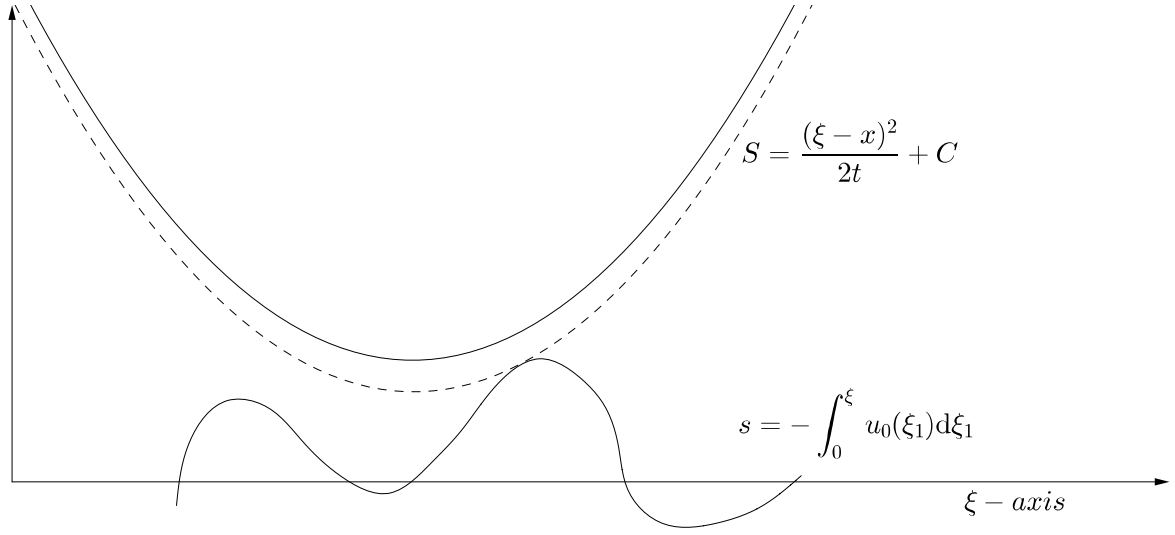

Figure 2.1: Geometric solution to the minimisation of $Z(\xi)$

The geometrical approach is now extended to find the shape of the asymptotic solution to the Burgers equation. In fact, several parabolas could be drawn at every location x and at a given

time t. It might occur that two parabolas touch simultaneously at two points. When $t \gg 1$–for the parabolas are spread out–the contact points come close to the tops of the $s(\xi)$ curve; these tops can be seen as local maxima of the initial condition (see figure 2.2). The hypothesis of large time is fundamental from this point forward and it adds to the vanishing-viscosity simplification. We denote η_i ($i = 0, \pm1, \pm2...$) the abscissa of the i-th top, furthermore we denote the abscissae of the two contact points by ξ_i and ξ_{i+1} (for a given t and x). The integrals in (2.11) are computed as the sum of contributions in the immediate neighbourhoods of ξ_i and ξ_{i+1}. Noting that $\xi_i \simeq \eta_i$ and $\xi_{i+1} \simeq \eta_{i+1}$, expanding $s(\xi)$ around η_i and η_{i+1}, one obtains (see Kida [4]):

$$u(x,t) = \frac{1}{t}\left(x - \frac{\eta_i + \eta_{i+1}}{2}\right) - \frac{1}{2t}\left(\eta_{i+1} - \eta_i\right)\tanh\left[\frac{1}{4\mu t}\left(\eta_{i+1} - \eta_i\right)\left(x - \chi_i\right)\right] \tag{2.14}$$

where:

$$\chi_i = \frac{\eta_i + \eta_{i+1}}{2} - \frac{s(\eta_{i+1}) - s(\eta_i)}{\eta_{i+1} - \eta_i}t + \frac{\mu t}{\left(\eta_{i+1} - \eta_i\right)}\log\left(\frac{1}{s(\eta_i)}\frac{\partial^2 s(\eta_{i+1})}{\partial \eta^2}\right). \tag{2.15}$$

Equations (2.14) and (2.15) are valid within the region $1/2\left(\chi_{i-1} + \chi_i\right) < x < 1/2\left(\chi_i + \chi_{i+1}\right)$. Once again, it should be recalled that two hypotheses have been considered: $\mu \to 0$ and $t \gg 1$. If the Reynolds number Re is so big that $Re \gg t \gg 1$, since the second term of equation (2.14) and the third term of equation (2.15) disappear, they become:

$$u(x,t) = \begin{cases} \dfrac{x - \eta_i}{t} & \text{for } \dfrac{\chi_{i-1} + \chi_i}{2} < x < \chi_i \\ \dfrac{x - \eta_{i+1}}{t} & \text{for } \chi_i < x < \dfrac{\chi_i + \chi_{i+1}}{2} \end{cases} \tag{2.16}$$

and:

$$\chi_i = \frac{\eta_i + \eta_{i+1}}{2} - \frac{s(\eta_{i+1}) - s(\eta_i)}{\eta_{i+1} - \eta_i}t. \tag{2.17}$$

Equation (2.16) represents a shock of strength μ_i/t located at χ_i, where:

$$\mu_i = \eta_{i+1} - \eta_i. \tag{2.18}$$

The shock moves with the velocity:

$$a_i = \frac{1}{t}\left(\chi_i - \frac{\eta_{i+1} + \eta_i}{2}\right). \tag{2.19}$$

From (2.17), one can infer that the coordinate χ_i coincides with the axis of the parabola passing through the two tops $(\eta_i, s(\eta_i))$ and $(\eta_{i+1}, s(\eta_{i+1}))$ of the s curve. Thus the velocity field in this circumstance is represented by a sequence of vertical lines (shocks) connected by oblique lines of slope l/t. The positions of shocks and the intersections of the oblique lines with the x-axis are given by χ_i and η_i respectively. It should be remarked that every shock has a different speed, therefore they collide with each other from time to time.

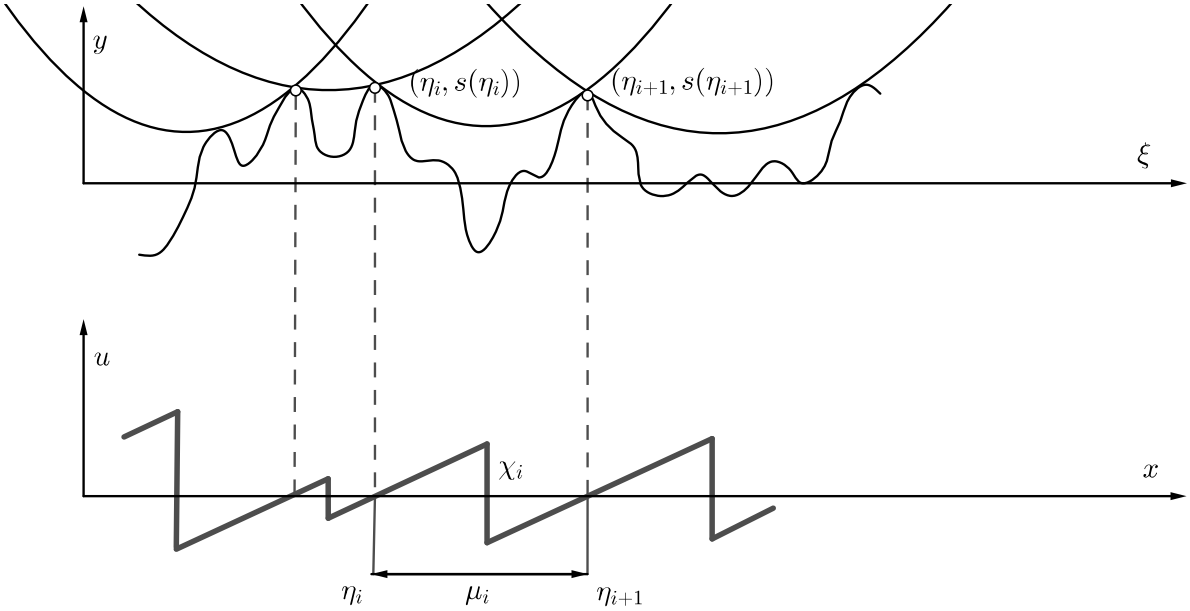

Figure 2.2: A sequence of parabolas in contact with s and the corresponding velocity field

2.1.2 Burgers inertial range

From the analytic solution (for $t \gg 1$ and vanishing viscosity), the structure function $|\delta u(x, x', t)|^q = |u(x,t) - u(x',t)|^q$ is computed (see [5]). Firstly, let us consider a large space periodicity L meaning that a large number of shocks is included in the domain. Let $\widetilde{N}_s(t)$ be the number of shocks included in L and $l = x - x'$ the distance between two points of the domain. If $\bar{l}(t)$ is the mean distance between shocks, then there exists several intervals $I_j(t)$ along the x axis such that l satisfies $l_s \ll l \ll \bar{l}(t)$, where l_s is the shock width.
Outside the shock, the velocity field has a slope of $1/t$, thus:

$$\lim_{L\to\infty} u(x,t) - u(x',t) = l/t \tag{2.20}$$

whereas in the I_j interval including the j-th shock:

$$\lim_{L\to\infty} u(x,t) - u(x',t) = \Delta u_j(t) \tag{2.21}$$

where $\Delta u_j(t)$ is the j-th shock strength. Therefore, the velocity structure function $|\delta u(x, x', t)|^q = |u(x,t) - u(x',t)|^q$ is:

$$|\delta u(x,x',t)|^q = \begin{cases} |\Delta u_j(t)|^q H\left(x' + l - x_j(t)\right) \times H\left(x_j(t) - l\right) + \mathcal{O}(l) & \text{in the interval including shock} \\ \mathcal{O}(l^q) & \text{in the interval not including shock} \end{cases} \tag{2.22}$$

where $H(x)$ is the Heaviside function and $x_j(t)$ is the position of the j-th shock. The ensemble

average of (2.22) is replaced by the spatial average as suggested by Gotoh [5]:

$$\begin{aligned}\langle|\delta u(x,x',t)|^q\rangle &= \frac{1}{L}\int_0^L \left|\delta u(x'+l,x',t)\right|^q \mathrm{d}x' \\ &\underset{\mathrm{L}\to\infty}{=} \frac{1}{L}\sum_j^{\widetilde{N}_s(t)} |\Delta u_j(t)|^q \int_{(x_{j-1}+x_j)/2}^{(x_j+x_{j+1})/2} H\left(x'+l-x_j(t)\right)\times H\left(x_j(t)-l\right)\mathrm{d}x' \\ &\underset{\mathrm{L}\to\infty}{=} \frac{\widetilde{N}_s(t)}{L}\frac{1}{\widetilde{N}_s(t)}\sum_j^{\widetilde{N}_s(t)} |\Delta u_j(t)|^q\, l.\end{aligned} \tag{2.23}$$

If one considers:

$$\lim_{L\to\infty}\frac{\widetilde{N}_s(t)}{L} = n(t),$$

then, one finally obtains (considering also negative l):

$$\left\langle\left|\delta u(x,x',t)\right|^q\right\rangle = n(t)\left\langle|\Delta u_j(t)|^q\right\rangle\,|l|. \tag{2.24}$$

The energy spectrum is computed from the velocity correlation function:

$$\begin{aligned}\langle u(x+l,t)u(x,t)\rangle &= \langle u(x,t)^2\rangle - \frac{1}{2}\langle|\delta u(x,x',t)|^2\rangle \\ &= \langle u(x,t)^2\rangle - \frac{1}{2}n(t)\langle|\Delta u_j(t)|^2\rangle\,|l|\end{aligned} \tag{2.25}$$

and it is equal to:

$$E(k,t) = \frac{1}{\pi}\int_0^\infty \langle u(x+l,t)u(x,t)\rangle\cos(kl)\mathrm{d}l. \tag{2.26}$$

By substitution of (2.22) into (2.26) and integrating by parts the resulting expression, one finally gets:

$$E(k,t) \sim \frac{n(t)\langle|\Delta u_j(t)|^2\rangle}{2\pi k^2}. \tag{2.27}$$

This expression is valid under the hypothesis that $L\to\infty$ or $k \gg k_0$, where k_0 is the wave number of the energy spectrum peak. In conclusion, the energy spectrum of the Burgers equation is proportional to k^{-2}.

2.2 Numerical approach

2.2.1 Numerical estimation of the exact solution: validation

Equation (2.11) provides an analytic expression of the solution to the Burgers equation. Nevertheless, improper integrals appear inside this formula, meaning that it is valid for an infinite

domain. A Matlab® function has been developed to estimate the value of (2.11) for each time and location in space. Integrals are computed with the Simpson's rule, a fourth-order scheme for numerical integration.

In order to demonstrate the validity of this approach, a comparison with a known solution is carried out. Indeed, we recall that the Burgers equation could be reduced to the heat equation by means of the Cole-Hopf transformation. Now, the heat equation has a specific solution for a given initial condition, namely, if one writes the differential problem as:

$$\begin{cases} \phi_t = \mu \phi_{xx} \\ \phi(x,0) = b + a\cos(kx) \end{cases} \tag{2.28}$$

then, the solution of the heat equation for the specified initial condition is given by:

$$\phi(x,t) = b + ae^{-\mu k^2 t}\cos(kx). \tag{2.29}$$

By applying the Cole-Hopf transform (2.5), velocity is obtained at every t and x:

$$u(x,t) = \frac{2\mu a k e^{-\mu k^2 t}\sin(kx)}{b + ae^{-\mu k^2 t}\cos(kx)} \tag{2.30}$$

where $b > |a|$ for u to be a $\mathscr{C}^2$ function. This expression is compared to the numerical estimation of equation (2.11) for the very same initial condition. Moreover, two different values of viscosity are imposed to investigate its effect; table 2.1 collects the parameters employed for the two cases. Finally, the finite domain from $x = -10$ to $x = 10$ is discretised with 512 points.

Table 2.1: Parameters used to draw the analytic solution to the Burgers equation

Case	μ	a	b	k	t_0	t_{final}
A	$2 \cdot 10^{-4}$	1.5	2	4π	0	1
B	$2 \cdot 10^{-2}$	1.5	2	4π	0	1

Figures 2.3a and 2.3b show the comparison between the exact solution and the estimated velocity at t_{final}. Despite a good overall matching, the estimated velocity is not well approximated at the boundaries of the domain. In particular, this effect is more intense at greater μ.
Indeed, equation (2.11) is valid for an infinite domain, whereas in practice this domain was clipped from -10 to 10. Nonetheless, since for vanishing viscosity the dominant contribution to the improper integrals is local (see Burgers [3] and Gotoh [5]), the deviation from the exact solution is substantial exclusively at the domain boundaries. Moreover, when viscosity increases, this effect becomes less and less local, thus explaining the greater deviation for case B.

2.2.2 Numerical estimation of the exact solution: initial condition imposed

In this section a specific initial condition is imposed to the Burgers equation and its time evolution is investigated along with the effect of viscosity. The main concern is to study the sawtooth structure described by Burgers, a theory largely developed for $\mu \to 0$, and how the occurrence of shock waves is modified by increasing μ.
The initial condition $u_0(x)$ is a zero-mean signal from $x = 0$ to $x = 1$ with a given spectrum content: it is a window in Fourier space of constant amplitude $2e^{-4}$ from wave number $k = 1$ to $k = 10$. In other words, the modes from $k = 1$ to $k = 10$ are equally excited, though a random

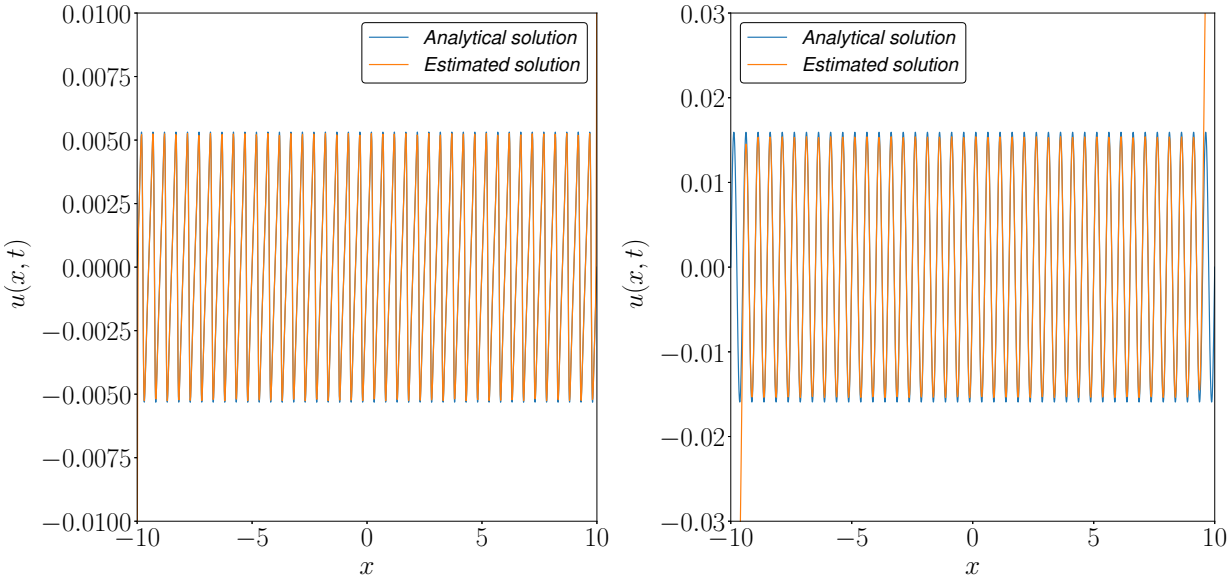

(a) Analytic solution compared to estimated solution at $t = 1$, case A

(b) Analytic solution compared to estimated solution at $t = 1$, case B

Figure 2.3: Comparison of analytic solution with estimated solution

phase is set. The spectrum amplitude $2e^{-4}$ is chosen for the numerical estimation to be accurate enough at the largest μ. Figure 2.4 shows the initial velocity signal and its spectrum; according to section 2.1, from such an initial condition, shockwaves will rapidly develop.

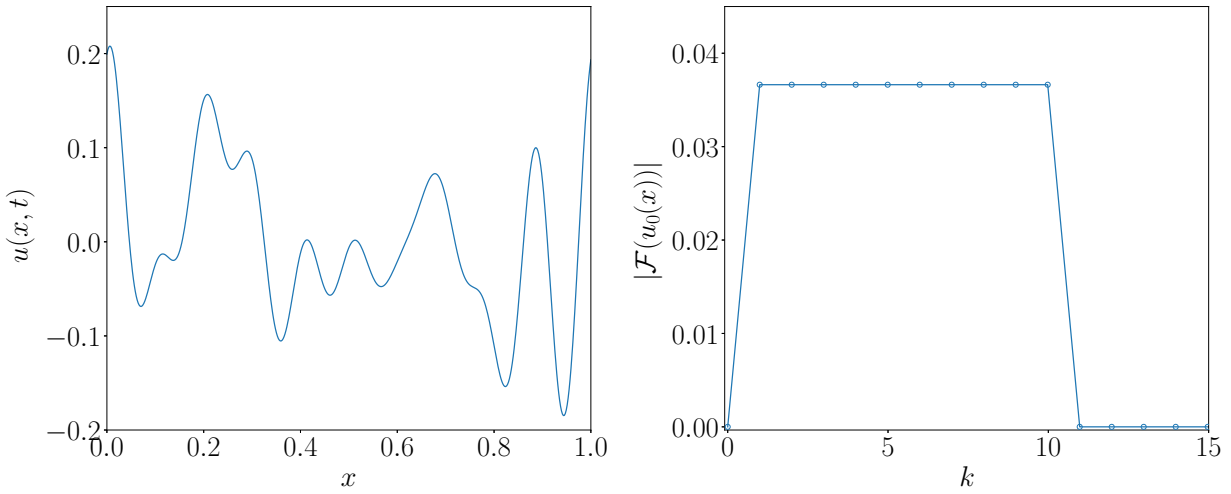

(a) Velocity as a function of space at $t = 0$

(b) $u_0(x)$ discrete spectrum

Figure 2.4: Initial condition

The estimation of $u(x,t)$ was carried out for different values of μ. Table 2.2 collects all the parameters employed.

Figure 2.5 shows how velocity evolves in time and the impact of viscosity on the solution. As

Table 2.2: Estimated solution: parameters employed. N_x number of points in space, N_t time instants

μ	$1 \cdot 10^{-5}$	$5 \cdot 10^{-5}$	$1 \cdot 10^{-4}$	$3 \cdot 10^{-3}$	$5 \cdot 10^{-4}$
N_x	512	512	512	512	512
t_{final}	15	15	15	15	15
N_t	500	500	500	500	500

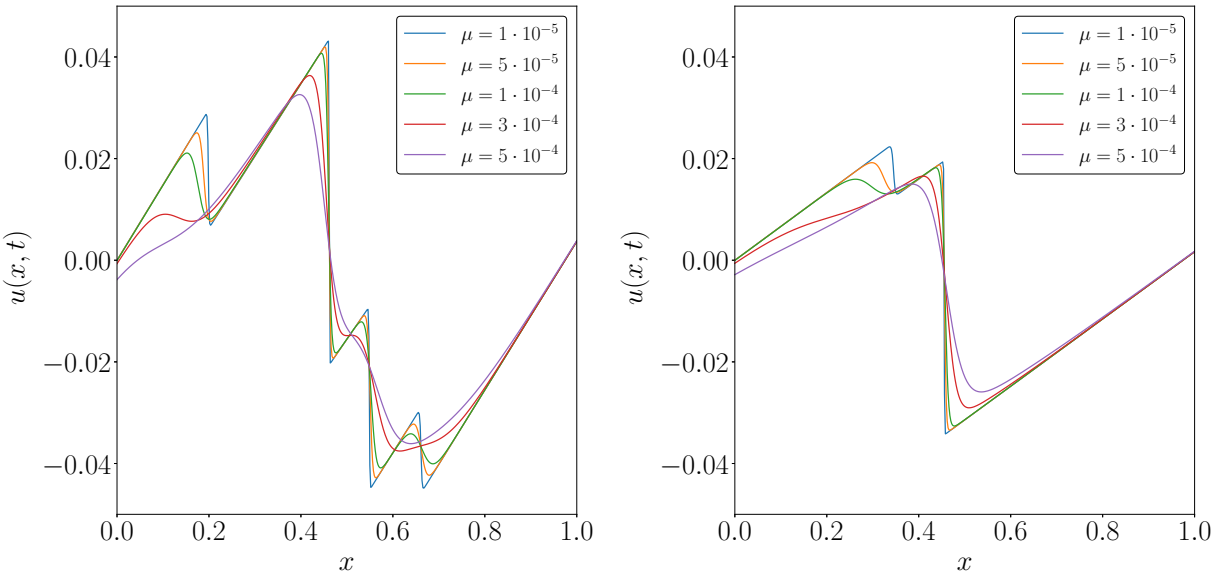

(a) Velocity as a function of space at $t = 7.5$

(b) Velocity as a function of space at $t = 15$

Figure 2.5: Evolution in time of $u_0(x)$ for different values of μ

anticipated, several shock fronts form from the initial conditions. As time passes, they merge into a unique shock front since their velocity of propagation is different; this feature justifies the fact that randomness decreases in time, as stated by Kida [4]. The effect of viscosity is manifest: shocks are smoothed out as μ increases.

2.2.3 The energy spectrum of the Burgers equation

The main objective of this section is to assess the energy spectrum $E(k,t)$ and its evolution in time for the given initial condition. As anticipated in section 2.1.2, $E(k,t)$ is proportional to k^{-2} at large times. It is straightforward to verify this statement from the results of section 2.2.2. We recall that the energy spectrum is defined as the square of the Fourier transform of $u(x,t)$:

$$E(k,t) = \mathcal{F}(u(x,t))^2 \tag{2.31}$$

where $\mathcal{F}(\cdot)$ indicates the Fourier transform. By applying this simple definition to section 2.2.2 results, one could draw the spectrum for different values of viscosity (see figures 2.6a and 2.6a).[1] At $t = 7.5$ the spectrum is noisier and does not align to the k^{-2} line yet, in accordance with Cole [29]. As time passes–at $t = 15$–the energy spectrum becomes proportional to k^{-2}, even though

[1] The vertical axis is clipped since the numerical error of the integration scheme becomes dominant below 10^{-10}.

higher frequencies are filtered out for increasing viscosity (for μ smooths out shock waves). Besides, the higher the viscosity, the more intense the filtering effect is. This phenomenon is depicted in figures 2.6a and 2.6b.

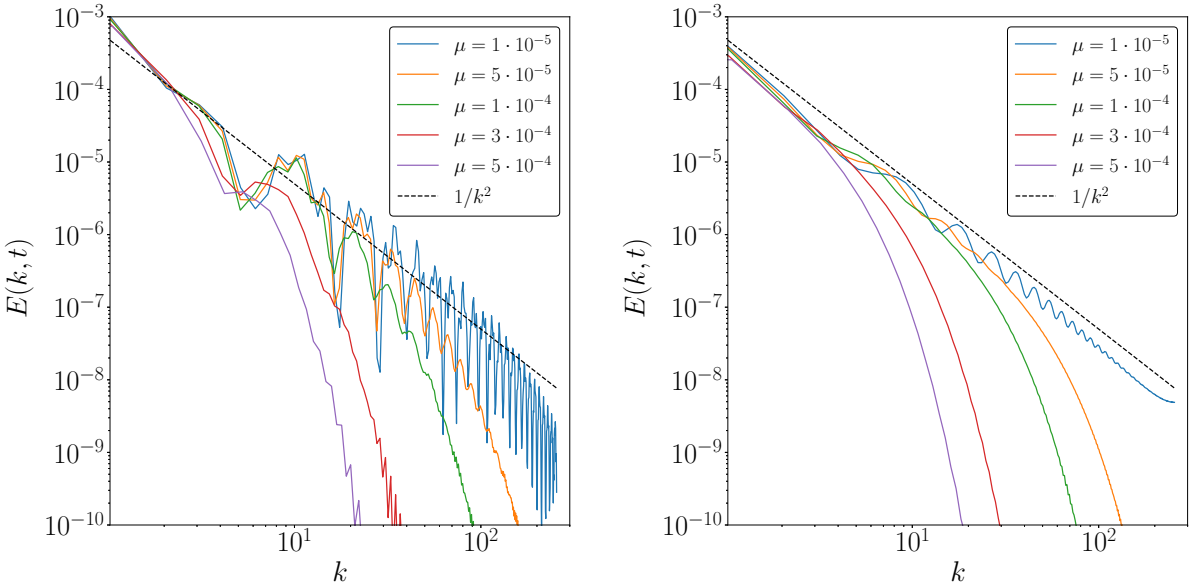

(a) Spectrum as a function of k at $t = 7.5$

(b) Spectrum as a function of k at $t = 15$

Figure 2.6: Evolution in time of $E(k,t)$ for different values of μ

However, the energy spectrum alone does not provide all the information about the velocity time evolution. Indeed, when the phase spectrum is looked at, it shows a peculiar behaviour since it is equal to either $-\pi/2$ or $\pi/2$, whatever the value of viscosity μ.

This peculiar feature of the phase spectrum has an analytical reason. Because of its periodicity, the sawtooth signal could be decomposed by means of the Fourier series, which is defined as:

$$f(x) = \frac{1}{2}a_0 + \sum_{k=1}^{\infty} a_k \cos kx + \sum_{k=1}^{\infty} b_k \sin kx \tag{2.32}$$

where:

$$a_0 = \frac{1}{\pi}\int_{-\pi}^{\pi} f(x)\mathrm{d}x \tag{2.33a}$$

$$a_k = \frac{1}{\pi}\int_{-\pi}^{\pi} f(x)\cos kx\mathrm{d}x \tag{2.33b}$$

$$b_k = \frac{1}{\pi}\int_{-\pi}^{\pi} f(x)\sin kx\mathrm{d}x \tag{2.33c}$$

In this specific case, the a_k components are zero-valued, whereas the b_k coefficients are propor-

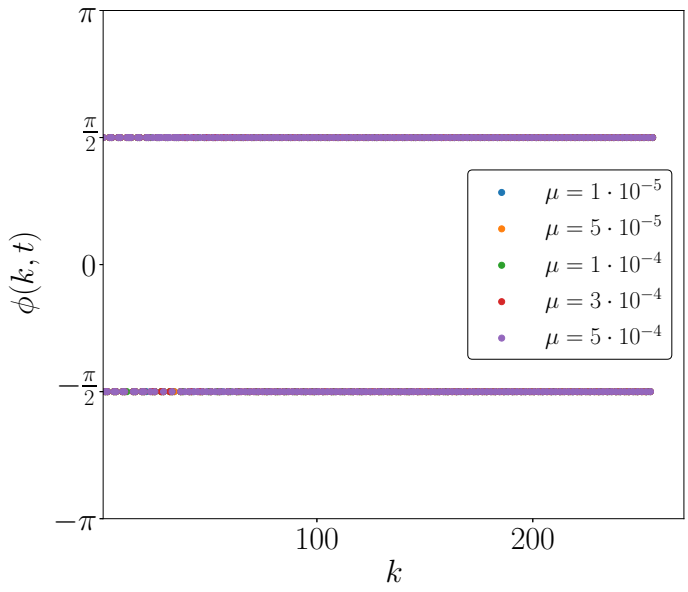

Figure 2.7: Phase as a function of k for increasing viscosity, $t = 1000$

tional to $\pm 1/k$. One can infer the amplitude and phase spectra from a_k and b_k, namely:

$$A(k) = \sqrt{a_k^2 + b_k^2} \tag{2.34a}$$

$$\phi(k) = \arctan \frac{b_k}{a_k} \tag{2.34b}$$

This provides a theoretical basis which justifies not only:

$$\lim_{t \to \infty} \phi(k,t) = \pm \frac{\pi}{2} \tag{2.35}$$

but also:

$$\lim_{t \to \infty} E(k,t) \propto \frac{1}{k^2} \tag{2.36}$$

since the energy spectrum is the amplitude spectrum squared.
Another feature to look at is the mean value of the energy spectrum as a function of time. Indeed, it is possible to compute a k-mean of the energy spectrum for every t and then plot it as a function of time itself. Therefore, the mean spectrum is defined as:

$$E_{mean}(t) = \frac{2}{N_x} \sum_{i=1}^{i=N_x/2} E(k_i, t) \tag{2.37}$$

where N_x is the number of grid points. The result–obtained for $\mu = 10^{-5}$–is plotted in figure 2.8b, where $E_{mean}(t)$ is shown to decay as t^{-2}.

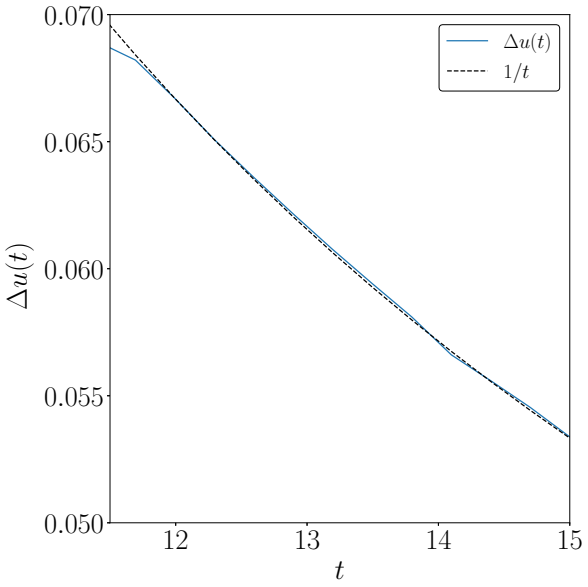

(a) Shockwave-strength decay from $t = 11.5$ to $t = 15$

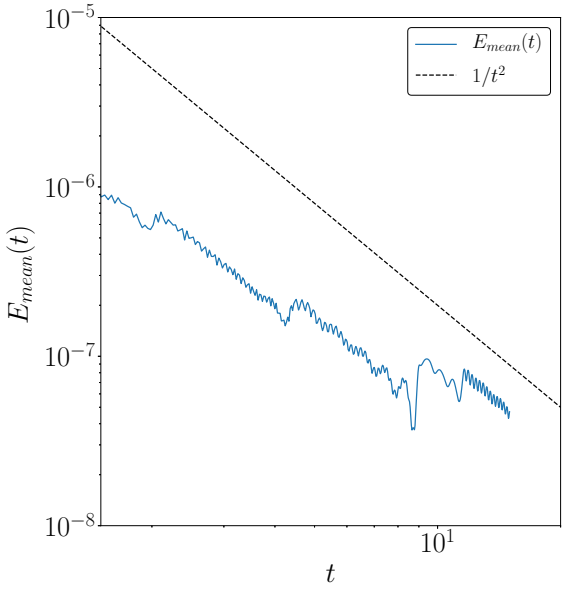

(b) Energy spectrum mean value as a function of t

Figure 2.8: Time decay of Δu and $E_{mean}(t)$ for $\mu = 10^{-5}$

Such observation is in accordance with the theoretical results issue of section 2.1, where it was found that (see Kida [4]):

$$\Delta u = \mu_i / t. \tag{2.38}$$

In other words, the shock strength decays as $1/t$ (see figure 2.8a, where the decrease of Δu for one shockwave is plotted as a function of time); since the energy spectrum is dominated by such discontinuities and the Fourier transform of u is raised to the power of 2 to obtain the energy spectrum, $E_{mean}(t)$ is proportional to t^{-2}.

Finally, the mean energy spectrum of figure 2.8b jumps at some times. This behaviour occurs when two shockwaves coalesce to form a unique discontinuity of greater strength. As a matter of example, let us consider $t = 11.5$, where $E_{mean}(t)$ undergoes a jump. Figures 2.9a and 2.9b depict the solution for $t - dt$ and $t + dt$: two shocks merge to form a unique discontinuity thus justifying the energy spectrum jump.

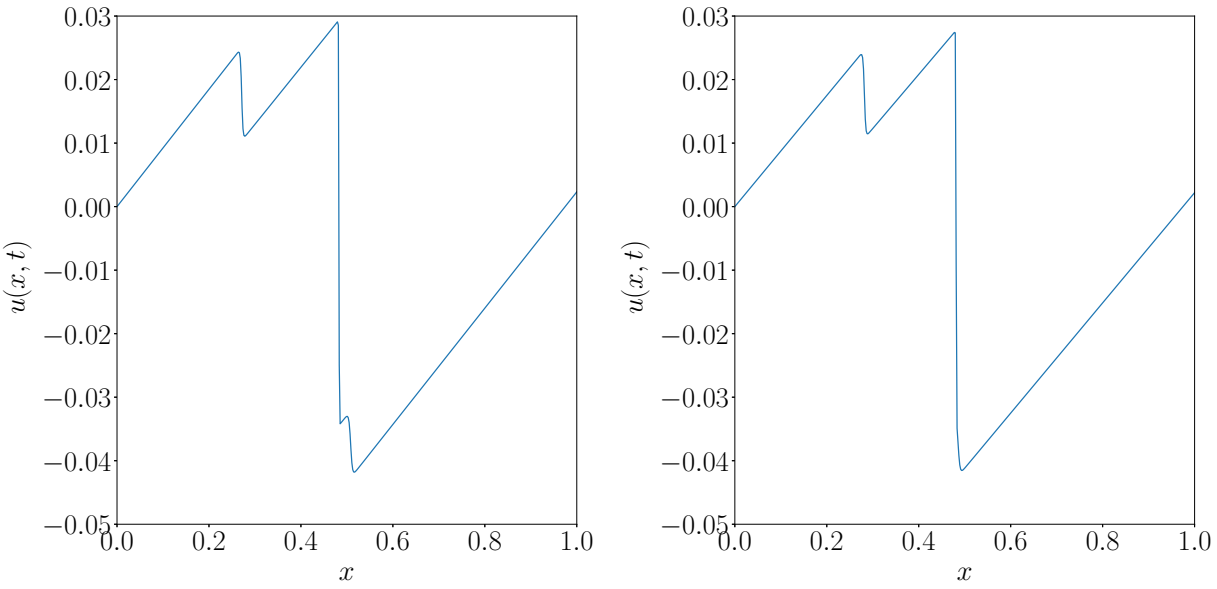

(a) Velocity as a function of space at $t = 11.5 - dt$ (b) Velocity as a function of space at $t = 11.5 + dt$

Figure 2.9

Part 3

Dynamic and spectral properties of one-dimensional ideal flows

This chapter demonstrates, analytically and numerically, that–under the assumption of small perturbation–a mapping between the Navier-Stokes equations and the Burgers equation exists. The velocity evolves in the well-known sawtooth. Therefore, the energy spectrum is inversely proportional to the square of the wave number. Discontinuities dominate the spectral properties of the flow.

3.1 From the one-dimensional Navier-Stokes equations to the Burgers equation: theoretical background

This section provides the theoretical tools needed to interpret numerical results. The gas is ideal. As shown in sections 2.1 and 2.1.2, the Burgers equation has an exact solution and its energy spectrum is proportional to k^{-2}. These results constitute a strong theoretical basis and something to compare numerical simulations to.
In fact, under the hypothesis of quasi-simple waves, the one-dimensional Navier-Stokes equations can be rewritten in a Burgers-like form, thus justifying similar asymptotic behaviours such as the convergence to the sawtooth. As a consequence, the one-dimensional Navier-Stokes energy spectrum is expected to be dominated by discontinuities.
As shown by Karpman [21] and Crighton [7], the Navier-Stokes equations (1.7) can be rewritten under the assumption of quasi-simple waves:

- Non-linear terms are retained up to second-order;
- Dissipation coefficients are considered small to first order, this means that non-linear dissipative terms may be neglected.

The perturbation propagates along the x axis. Therefore, system (1.7), where the total energy conservation has been replaced by the entropy equation (as shown in section 1.1.4), becomes:

$$\begin{cases} \dfrac{\partial \rho}{\partial t} + \dfrac{\partial \rho u}{\partial x} = 0 \\ \rho \left(\dfrac{\partial u}{\partial t} + u \dfrac{\partial u}{\partial x} \right) = -\dfrac{\partial p}{\partial x} + \left(\dfrac{4}{3}\mu + \mu_b \right) \dfrac{\partial^2 u}{\partial x^2} \\ \dfrac{\partial s}{\partial t} + u \dfrac{\partial s}{\partial x} = \dfrac{k}{\rho T} \dfrac{\partial^2 T}{\partial x^2} \end{cases} \tag{3.1}$$

The non-linear viscous terms have been neglected in the entropy equation.
Let us consider the first equation of system (3.1):

$$\frac{\partial \rho}{\partial t} + \rho \frac{\partial u}{\partial x} + u \frac{\partial \rho}{\partial x} = 0. \tag{3.2}$$

The chain rule applied to $\rho = \rho(p, s)$ gives:

$$\begin{aligned} \frac{\partial \rho}{\partial t} &= \left(\frac{\partial \rho}{\partial p}\right)_s \frac{\partial p}{\partial t} + \left(\frac{\partial \rho}{\partial s}\right)_p \frac{\partial s}{\partial t}, \\ \frac{\partial \rho}{\partial x} &= \left(\frac{\partial \rho}{\partial p}\right)_s \frac{\partial p}{\partial x} + \left(\frac{\partial \rho}{\partial s}\right)_p \frac{\partial s}{\partial x}. \end{aligned} \tag{3.3}$$

If one substitutes (3.3) into (3.2), it follows:

$$\frac{\partial p}{\partial t} + u \frac{\partial p}{\partial x} + \rho c^2 \frac{\partial u}{\partial x} = -\frac{c^2 k}{\rho T} \left(\frac{\partial \rho}{\partial s}\right)_p \frac{\partial^2 T}{\partial x^2} \tag{3.4}$$

or alternatively:

$$\frac{\partial p}{\partial t} + u \frac{\partial p}{\partial x} + \rho c^2 \frac{\partial u}{\partial x} = -\frac{c^2 k}{\rho T} \left(\frac{\partial \rho}{\partial s}\right)_p \left(\frac{\partial T}{\partial p}\right)_s \frac{\partial^2 p}{\partial x^2} \tag{3.5}$$

Since:

$$\frac{1}{T} \left(\frac{\partial p}{\partial \rho}\right)_s \left(\frac{\partial \rho}{\partial s}\right)_p \left(\frac{\partial T}{\partial p}\right)_s = \frac{1}{c_v} - \frac{1}{c_p},$$

equation (3.5) becomes:

$$\frac{\partial p}{\partial t} + u \frac{\partial p}{\partial x} + \rho c^2 \frac{\partial u}{\partial x} = -\frac{k}{\rho} \left[\frac{1}{c_v} - \frac{1}{c_p}\right] \frac{\partial^2 p}{\partial x^2}. \tag{3.6}$$

From (3.1), a new set of equations is found:

$$\begin{cases} \dfrac{\partial p}{\partial t} + u \dfrac{\partial p}{\partial x} + \rho c^2 \dfrac{\partial u}{\partial x} = -\dfrac{k}{\rho} \left[\dfrac{1}{c_v} - \dfrac{1}{c_p}\right] \dfrac{\partial^2 p}{\partial x^2} \\ \rho \left(\dfrac{\partial u}{\partial t} + u \dfrac{\partial u}{\partial x}\right) = -\dfrac{\partial p}{\partial x} + \left(\dfrac{4}{3}\mu + \mu_b\right) \dfrac{\partial^2 u}{\partial x^2} \\ \dfrac{\partial s}{\partial t} + u \dfrac{\partial s}{\partial x} = \dfrac{k}{\rho T} \dfrac{\partial^2 T}{\partial x^2} \end{cases} \tag{3.7}$$

In order to derive the differential equation for quasi-simple waves, the density and the pressure are assumed to be the sum of two terms:

$$\begin{aligned} p(x,t) &= p(u) + \psi(x,t) \\ \rho(x,t) &= \rho(u) + \phi(x,t) \end{aligned} \tag{3.8}$$

where $p(u)$ and $\rho(u)$ satisfy the simple wave equations[1]:

$$\begin{cases} c(u)\dfrac{\partial \rho}{\partial u} = \rho(u) \\ c(u) = c_u + \dfrac{\gamma - 1}{2}u \\ \dfrac{\mathrm{d}p}{\mathrm{d}u} = c^2(u)\dfrac{\partial \rho}{\partial u} = c(u)\rho(u) \end{cases} \tag{3.9}$$

where c_u is the speed of sound of the unperturbed flow. The system above derives from the Euler equations written for a simple wave travelling in an ideal gas. Consequently, from this point forward we lose generality. An alternative approach for non-ideal gases will be proposed in chapter 4.
Furthermore, we seek $\psi(x,t)$ and $\phi(x,t)$ in such a form that the corresponding solution is as close as possible to the simple wave. Let us assume that these functions are small to second order. They will satisfy the linear equation:

$$\frac{\partial \psi}{\partial t} + c_u \frac{\partial \psi}{\partial x} = \frac{\partial \phi}{\partial t} + c_u \frac{\partial \phi}{\partial x} = 0. \tag{3.10}$$

Substituting (3.8) into the first and second equation of system (3.7) and taking into account (3.10), we obtain with second-order accuracy:

$$\begin{cases} \dfrac{\partial u}{\partial t} + [u + c(u)]\dfrac{\partial u}{\partial x} = -\dfrac{1}{\rho_0}\left[\dfrac{\partial \psi}{\partial x} - \left(\dfrac{4}{3}\mu + \mu_b\right)\dfrac{\partial^2 u}{\partial x^2}\right] \\ \psi = \dfrac{1}{2}\left[2\mu + \lambda - k\left(\dfrac{1}{c_v} - \dfrac{1}{c_p}\right)\right]\dfrac{\partial u}{\partial x} \end{cases} \tag{3.11}$$

Finally, by eliminating ψ:

$$\frac{\partial u}{\partial t} + \left(c_u + \frac{\gamma + 1}{2}u\right)\frac{\partial u}{\partial x} = \bar{\mu}\frac{\partial^2 u}{\partial x^2} \tag{3.12}$$

where:

$$\bar{\mu} = \frac{1}{2\mu_0}\left[\frac{4}{3}\mu + \mu_b + k\left(\frac{1}{c_v} - \frac{1}{c_p}\right)\right]$$

With the following transformation:

$$\xi = x - c_u t, \qquad \bar{u} = c_u + \frac{\gamma + 1}{2}u$$

equation (3.12) is reduced to the Burgers equation:

$$\frac{\partial \bar{u}}{\partial t} + \bar{u}\frac{\partial \bar{u}}{\partial \bar{\xi}} = \bar{\mu}\frac{\partial^2 \bar{u}}{\partial \xi^2}. \tag{3.13}$$

There exists a mapping between the one-dimensional Navier-Stokes equations to the Burgers equation under certain assumptions. The DNS code `Compreal` will help us verify this statement.

[1] We recall that a simple wave is a wave travelling in a single direction, where all the thermodynamic quantities are represented in the form of functions of velocity.

3.2 `Compreal`: main features of the code

Before discussing the results from `Compreal`–an in-house code developed at *Imperial College London*–, we first describe the code main features and how to generate an input of given properties . This said, the main purpose of this work has not consisted in developing any parts of `Compreal`: it has been used as a tool to study physical phenomena.

3.2.1 Numerical schemes and boundary conditions

The dimensionless Navier-Stokes equations solved by `Compreal` are recalled below (see Touber [30]):

$$\begin{cases} \dfrac{\partial \widehat{\rho}}{\partial \widehat{t}} + \operatorname{div}\left(\rho \widehat{\boldsymbol{u}}\right) = 0 \\ \dfrac{\partial \widehat{\rho}\widehat{\boldsymbol{u}}}{\partial \widehat{t}} + \operatorname{div}\left(\widehat{\rho}\widehat{\boldsymbol{u}} \otimes \widehat{\boldsymbol{u}}\right) = -\mathbf{grad}(\widehat{p}) + \dfrac{1}{\mathrm{Re}}\operatorname{div}(\widehat{\boldsymbol{\Pi}}) \\ \dfrac{\partial \widehat{\rho}\widehat{e_t}}{\partial \widehat{t}} + \operatorname{div}\left(\widehat{\rho}\widehat{e_t}\widehat{\boldsymbol{u}}\right) = -\operatorname{div}(\widehat{p}\widehat{\boldsymbol{u}}) + \dfrac{1}{\mathrm{Re}}\operatorname{div}(\widehat{\boldsymbol{\Pi}}\widehat{\boldsymbol{u}}) - \dfrac{1}{(\gamma-1)\mathrm{RePrM}^2}\operatorname{div}\left[\mathbf{grad}(\widehat{T})\right] \\ \widehat{p} = \widehat{p}(\widehat{T}, \widehat{\vartheta}) \end{cases} \tag{3.14}$$

where Re , Pr and M correspond to the Reynolds, Prandtl and Mach numbers respectively. The notation $\widehat{\bullet}$ indicates a dimensionless quantity. The one-dimensional spatial domain goes from $x = 0$ to $x = 1$. However, all the variables are stored at:

$$x(i) = \frac{\Delta x}{2} + i\frac{\Delta x}{2} \quad \text{for } i = 1, N_x \tag{3.15}$$

where Δx is the spacing between two successive nodes and N_x is the number of grid points.[2]. The differential problem (3.14) is completed by boundary and initial conditions. Periodic boundary conditions are imposed, meaning that all quantities have to be equal at the two boundaries $x = 0$ and $x = 1$. In addition, the initial density, velocity and specific total energy are set over the spatial domain.

The code performs Direct Numerical Simulation (DNS), i.e. no turbulence models are implemented. As common practice when dealing with turbulent flows, the methods employed are explicit in space and time. Indeed, implicit methods requires more computational cost as nonlinear systems are solved at every time-step; on the other hand, they ensure larger stability regions thus larger time-steps. Turbulent flows entail small time-steps to be chosen. Consequently, one cannot exploit the benefits of an implicit method while having high computational cost.

More precisely, the compressible Navier–Stokes equations of system (3.14) are integrated in time explicitly using a third-order TVD Runge-Kutta scheme (see [30]). Spatial derivatives are evaluated with a fourth-order centred finite difference dispersion-relation-preserving scheme (see [31]) using a 13-point stencil (a 4 points per wavelength cut-off is used for the optimisation). Numerical stability is ensured using a centred 13-point eighth-order explicit discrete filter optimised in spectral space following the methodology developed by Bogey et al. [32] (a 5 points per wave-

[2]When a wall boundary condition is imposed, the solution is known at the boundaries and there is no need to store it

length cut-off is used). This allows for accurate propagation of large-wavelength content (both from a dispersion and dissipation point of view) whilst minimising small-scale dissipation.

The discontinuities are captured using a localised artificial diffusivity (LAD) method [33], [34]. A viscous term is added to the equations where strong shocks are detected. The success of the method is based on an efficient shock detection together with the ability to fix an appropriate viscosity magnitude to ensure a sufficient number of point in the artificial shock structure. The LAD method has been regularly improved since its first formulation (see [33],[34],[35], [36],[37]) and targeted as an efficient and accurate method for the computation of compressible turbulent flows [37]. One of the strength of the method is its ability to ensure at least 4 points in the viscous structure and limit the spurious noise to a reasonable level of 1% of the shock strength (i.e. when coupled with accurate finite difference operators).

3.2.2 How to build the input of the code

As mentioned in the previous section, the initial density, velocity and specific total energy are imposed over the spatial domain. For the purposes of this work, the input has always a specific energy content. To this end, two Python functions implementing the direct and inverse Fourier transforms were developed. According to [38], the direct Fourier transform of an integrable function $f : \mathbb{R} \to \mathbb{C}$ is:

$$\widehat{f}(s) = \int_{-\infty}^{\infty} f(x) e^{-i2\pi sx} dx \tag{3.16}$$

while the inverse Fourier transform is defined as:

$$f(x) = \frac{1}{2\pi} \int_{-\infty}^{\infty} \widehat{f}(s) e^{i2\pi sx} ds \tag{3.17}$$

where x could be either time or space and s either frequency or wave number.
By making use of the Python functions `fft` and `ifft`, two tools were specifically designed, suiting best the purpose of this work:

1. `Direct_fft`: it returns the spectrum and the wave number (or frequency) vector in addition to the phase from a signal in space (or time);

2. `Inverse_fft`: it returns the signal in space (or time) from a spectrum and a phase.

The test signal depicted in figure 3.1 was used to validate both functions; it was designed to have a specific energy content.

`Direct_fft` computes the signal spectrum which shows a peak at $k = 1$ (see figure 3.2). The energy content corresponds to the area underneath the spectrum.
Now, given phase and spectrum, one should be able to reconstruct the original signal. This task is accomplished by `Inverse_fft`. Figure 3.3 shows the perfect matching between the test signal and the inverse Fourier transform issue of its phase and spectrum.

The function `Inverse_fft` is used throughout this work to generate input signals of given spectrum. Later in this chapter for instance, an initial velocity of constant spectrum from $k = 1$ to $k = 10$ is imposed to the flow, whereas the phase is random.

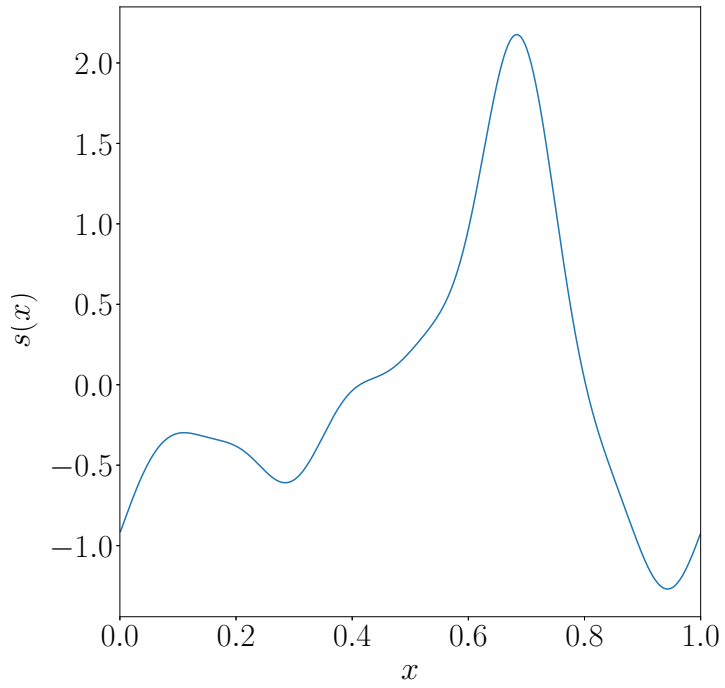

Figure 3.1: Test signal, sampling wave number $k_s = 512$

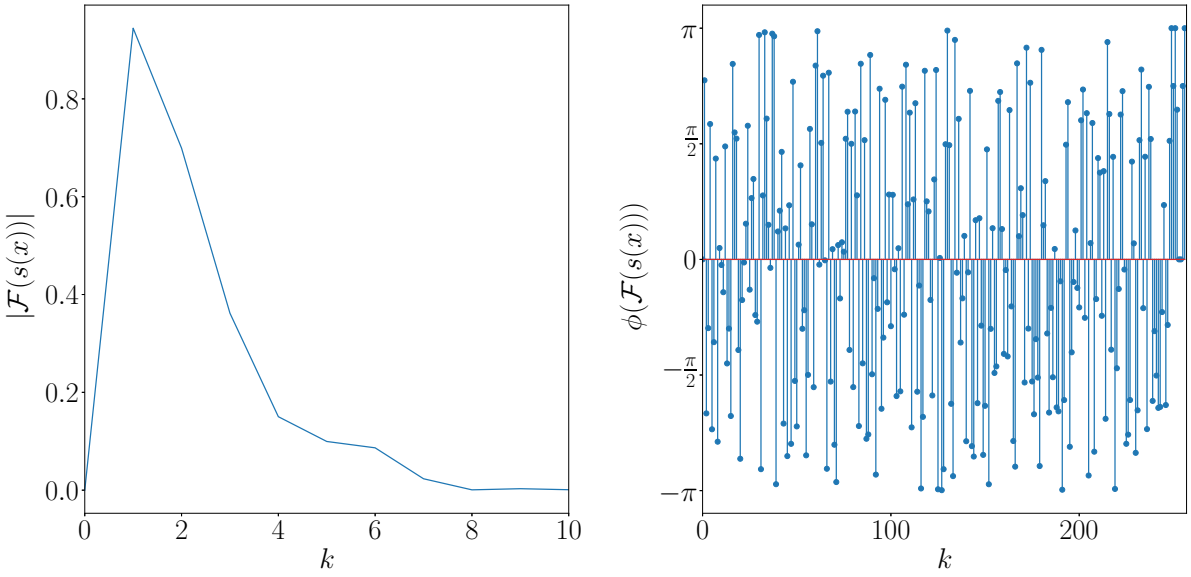

(a) Signal spectrum

(b) Phase spectrum

Figure 3.2: Fast Fourier transform of the test signal

3.3 From the one-dimensional Navier-Stokes equations to the Burgers equation: inviscid numerical simulations

In this section, dynamic and spectral behaviours observed from numerical simulations are discussed; the fluid is an ideal gas and different initial conditions are imposed. A non-viscous

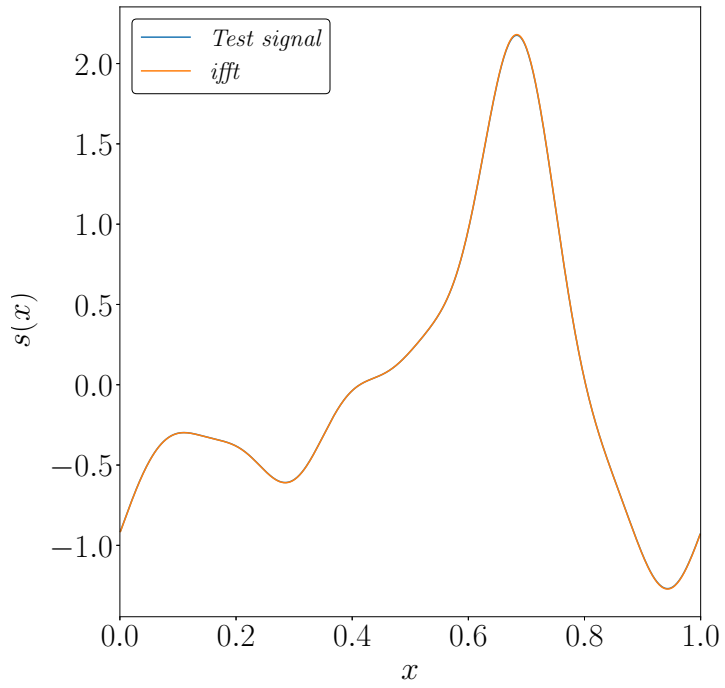

Figure 3.3: Inverse Fourier transform vs. original signal

version of `Compreal` has been used, thus, in the first instance, viscous terms will not be taken into account. In any manner, equation 3.13 holds true for $\mu \to 0$. Indeed, for the quasi-inviscid Burgers equation, the effect of viscosity is dominant at the discontinuity and negligible elsewhere (see section 2.2); this very same behaviour is assessed by the inviscid version of `Compreal` with a shock-capturing scheme which adds an artificial viscosity at the discontinuity.
In section 3.3.1, a velocity perturbation is imposed over the spatial domain; the temperature and the specific volume are set constant at $t = 0$.
In section 3.3.2, pure thermodynamic perturbations are imposed over the spatial domain at $t = 0$, while the initial velocity is set to zero.

Even though the same asymptotic behaviour is observed, it is interesting how velocity perturbations trigger thermodynamic perturbations and vice versa. Sections 3.3.1 and 3.3.2 therefore present two basic cases: in the former, kinetic energy oscillations are imposed to the flow at $t = 0$; in the latter, internal energy oscillations are imposed to the flow at $t = 0$.

3.3.1 Velocity perturbation

Firstly, the time evolution of a given initial-velocity perturbation is addressed. The initial temperature and specific volume are constant over the x domain at $t = 0$. Indeed, the initial condition $u_0(x)$ (the subscript $(\bullet)_0$ always refers to the initial condition) is a zero-mean signal from $x = 0$ to $x = 1$ with a given spectrum content: it is a window in Fourier space of constant amplitude 10^{-2} from wave number $k = 1$ to $k = 10$. In other words, modes from 1 to 10 are excited uniformly, though a random phase is set (see figure 3.4b). The specific volume is constant over the space domain and equal to $\vartheta = 0.9091$, the same for the temperature which is equal to $T = 1.001$. The perfect gas has a heat capacity ratio γ of 1.001.
The simulation ran on 4 cores. The spatial domain is discretised by 4096 points; the solution

was computed from $t = 0$ to $t = 1000$ with $\Delta t = 10^{-4}$ and 10^7 time steps. Table 3.1 collects all the parameters employed to run this first case referred to as *simulation 1*.

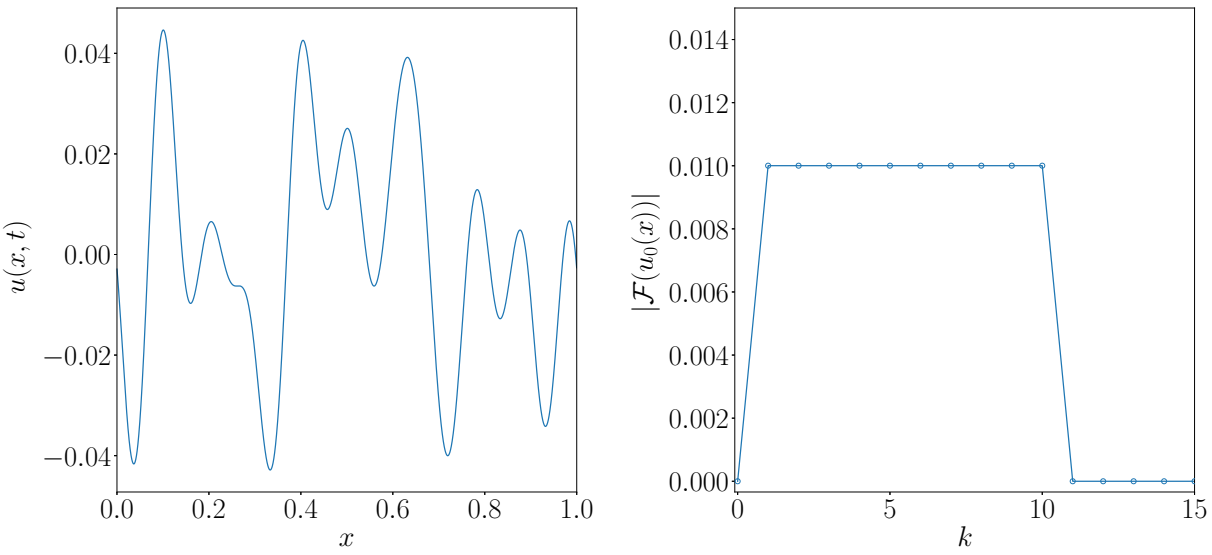

(a) Velocity as a function of space at $t = 0$

(b) $u_0(x)$ discrete spectrum

Figure 3.4: Initial condition

Table 3.1: *Simulation 1*: parameters employed

Parameter	Value
u_0	perturbation
$\overline{u}_0$	0
ϑ_0	0.9091
T_0	1.001
γ	1.001
N_x	4096
N_t	10^7
Δt	10^{-4}
t_{final}	1000

The time-space evolution of velocity is drawn on a $x - t$ diagram (figure 3.5). This graphic shows that discontinuities rapidly form: the colors are blurred at the beginning, whereas–from $t \simeq 2$ on–they change abruptly across the shocks. Since the gas is ideal, the velocity decreases across a shock front: the color darkens when a shock wave passes at a given location and time. In addition, diamond structures appear inside the domain due to the periodic shock waves interaction. Discontinuities merge as time passes, thus resulting in a more coherent diamond structure at larger t.

From section 3.1, the mapping between the one-dimensional Navier-Stokes equations and the Burgers equation is well-known. The quasi-simple waves theory implies small perturbations. Indeed, the initial conditions fully respect this assumption, thus a Burgers-like solution is expected. To this end, figure 3.6b depicts the velocity $u(x,t)$ at $t = 1000$. A sawtooth–Burgers-like–solution forms at large times from an initial random perturbation of given spectrum. In addition, fig-

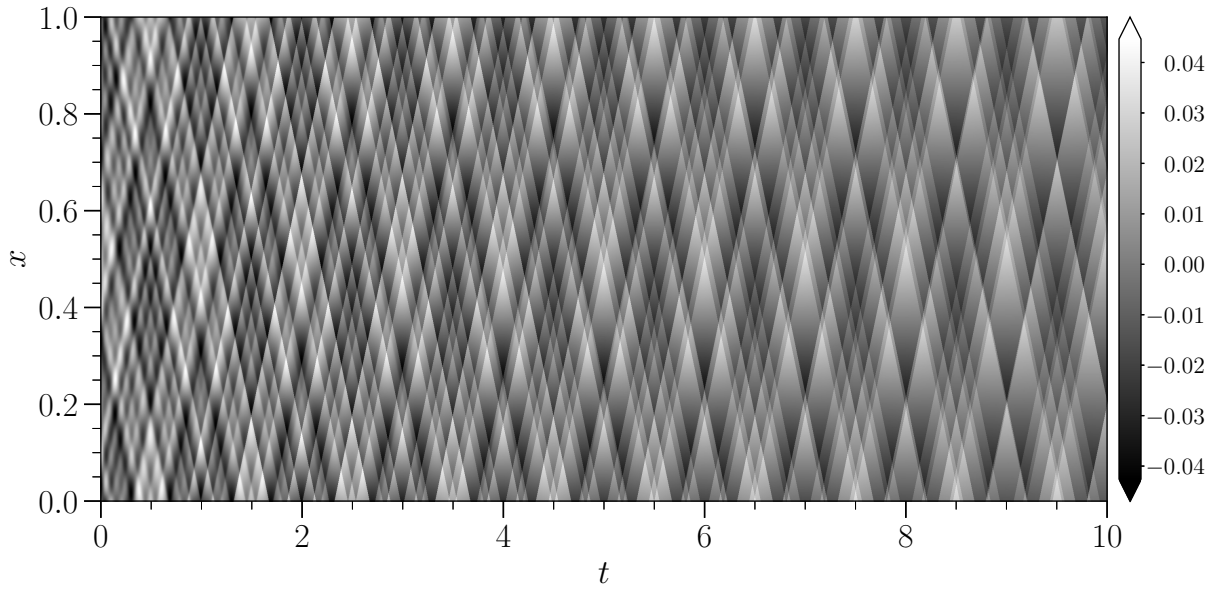

Figure 3.5: *Simulation 1*: velocity evolution in the $x-t$ diagram for $t \in [0; 10]$

ure 3.6a represents the velocity field at the time of formation of the first shock wave inside the domain.

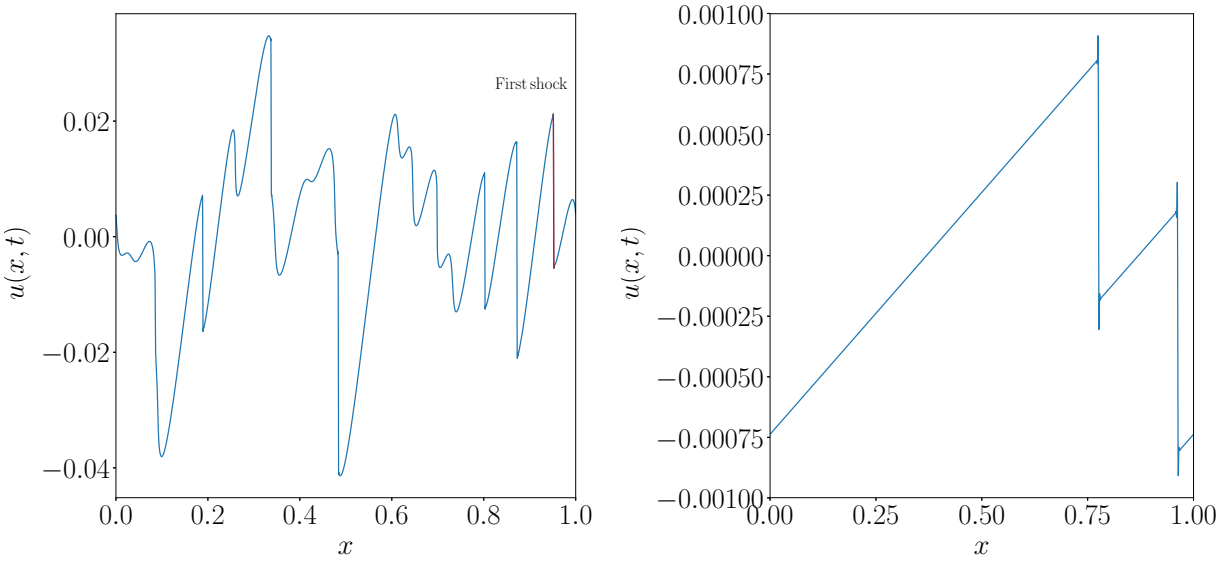

(a) Velocity as a function of x at $t = 1.8$

(b) Velocity as a function of x at $t = 1000$

Figure 3.6: *Simulation 1*: sectional views of the $x-t$ diagram

From the theoretical results of section 2.1.2, it can be inferred that the inertial spectrum is dominated by discontinuities and $E(k,t)$ is inversely proportional to the wave number squared. This statement can be verified by plotting the energy spectrum at $t = 1000$ (see figure 3.7), although $E(k,t)$ aligns with k^{-2} long before, at $t \simeq 2$.

The time evolution of the mean spectrum is a reliable indicator of the flow behaviour. It is

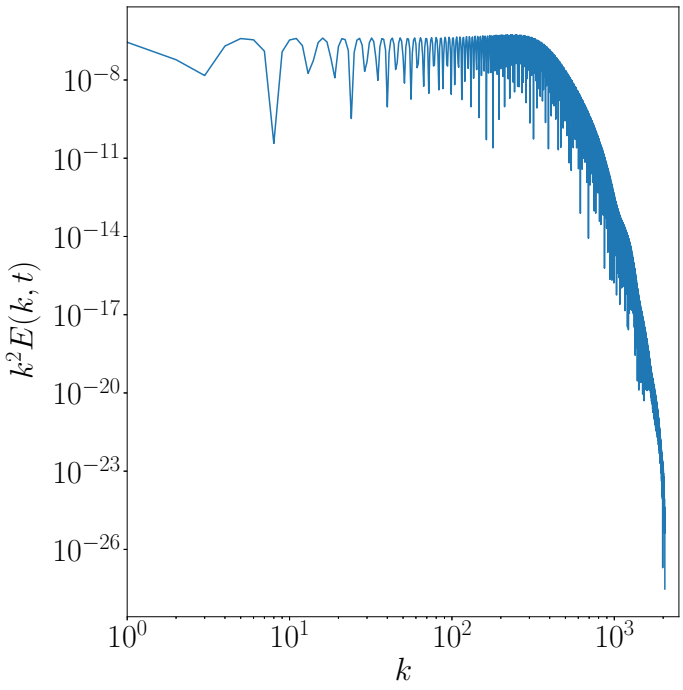

Figure 3.7: *Simulation 1*: energy spectrum times k^2 at $t = 1000$

defined as:

$$E_{mean}(t) = \frac{1}{N_{max} - N_{min}} \sum_{i=N_{min}}^{N_{max}} E(k_i, t) \tag{3.18}$$

where $N_{min} = 20$ and $N_{max} = 1000$ for 4096 grid points. In other words, the mean spectrum is computed from $k = 20$ to $k = 1000$. The lower boundary has been fixed–given the uniform initial-velocity spectrum from $k = 1$ to $k = 10$–for E_{mean} to indicate the formation of shock waves. The upper boundary corresponds to the cut-off wave number k_{cut}. After k_{cut}, the energy spectrum rapidly decreases because of numerical dissipation through the explicit filter at $4-5\Delta x$ (see section 3.2.1). Smaller structures, which have higher wave numbers, are filtered out.
From figure 3.8, three regimes appear to fully describe how the velocity perturbation develops inside the domain, namely:

1. **Shock-free regime**: the initial perturbation is injected inside the domain. Shock waves do not appear yet. When the velocity perturbation begins to steepen, E_{mean} ramps up. Through this simple tool, one can rapidly locate the instant of formation of the first shock wave, which occurs just before the time t_{max} for which E_{mean} is maximum.

2. **Transitional regime**: shock waves form inside the domain and, since discontinuities dominate the inertial range, $E(k,t)$ becomes proportional to k^{-2}. The velocity field tends to assume the typical sawtooth shape.

3. **Burgers regime**: the sawtooth solution is well established. Shock waves sweep the domain. The shocks strength diminishes in time as $1/t$, thus $E_{mean}(t)$ decreases as $1/t^2$; this result mirrors the behaviour observed in section 2.1.2. Figure 3.9 zooms in on the *Burgers*

regime and displays its main features: not only the characteristic slope, but also the small jumps when two shocks coalesce.

In this particular case, the time of formation of the first shock is $t_{shock} = 1.8$ and the *Burgers regime* is fully established at $t_{burg} = 26$ (see the vertical dashed lines in figure 3.8).

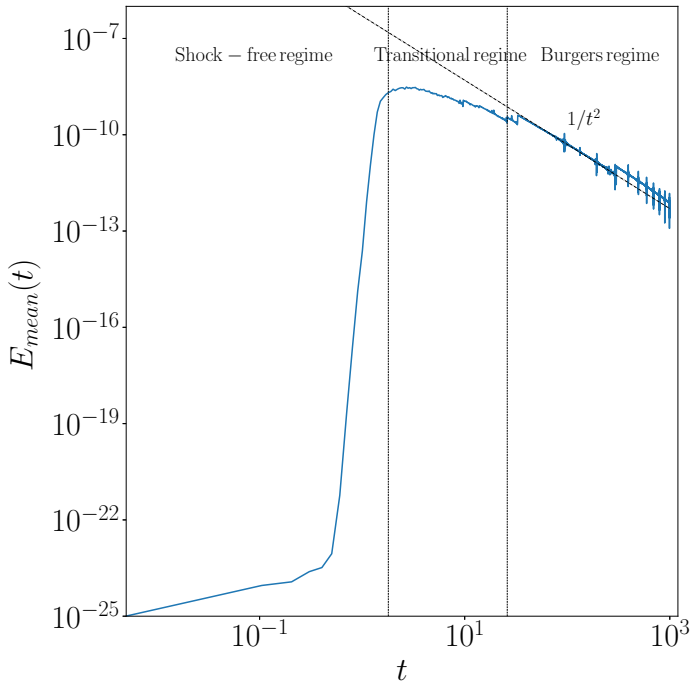

Figure 3.8: *Simulation 1*: mean spectrum as a function of time for $t \in [0; 1000]$

Phase alignment

The energy spectrum alone has been discussed thus far. However, the Fourier transform provides another valuable information, i.e. the phase spectrum. As discussed in section 2.2.3, the phase tends to align as time passes. In fact, the phase spectrum is constant and equal to $\pm\pi/2$ at large t (see figure 3.10).

Effect of changing the spatial discretisation on the energy spectrum

The effect of an increasing number of points along the x axis is now investigated. We recall that a non-viscous version of `Compreal` solving the Euler equations has been used so far. The very same input as *Simulation 1* is injected into the domain and the number of points N_x along the x dimension takes four values: 2048, 4096, 8192 and 16384.
Since dissipation does not play any role in the Euler equations, no dissipative scale exists. This means that the energy spectrum will be largely affected by the spatial discretisation of the domain. Indeed, when the full Navier-Stokes equations are taken into account, kinetic energy is dissipated through viscosity beyond a certain cut-off wave number. In the case of the Euler equations, the cut-off wave number depends on the number of grid points and is due to numerical

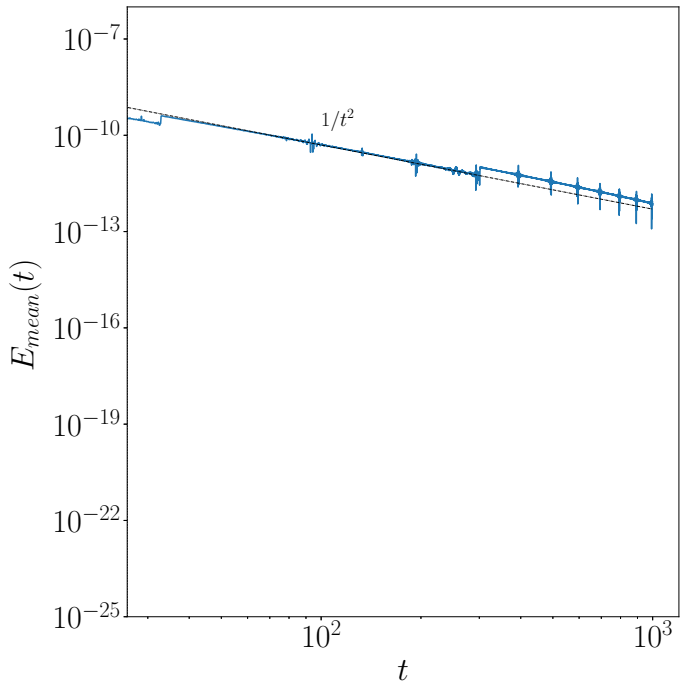

Figure 3.9: *Simulation 1*: zoom on the *Burgers range*

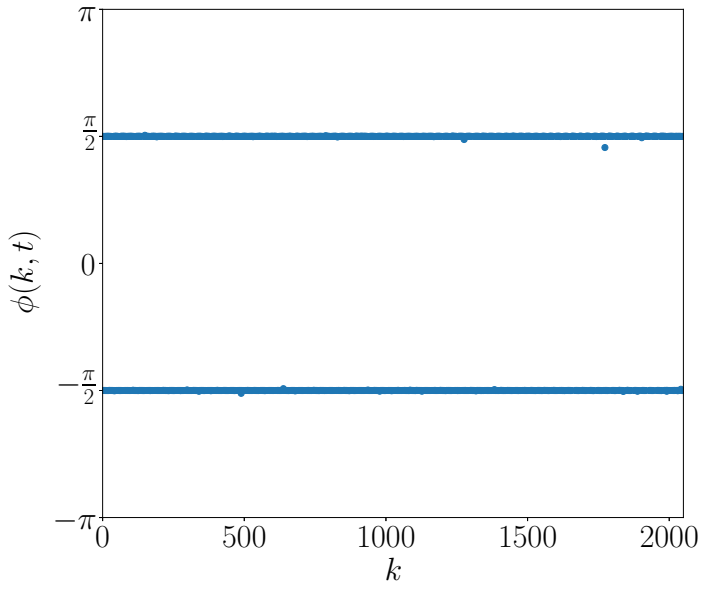

Figure 3.10: Phase as a function of k at $t = 1000$

dissipation through the explicit filter at $4 - 5\Delta x$ (see section 3.2.1). Smaller structures, which have higher wave numbers, are filtered out.

By increasing N_x, one puts kinetic energy over a broader spectrum of wave numbers. This can be easily verified on figure 3.11. The energy spectrum $E(k,t)$ is traced for increasing N_x at time 10.

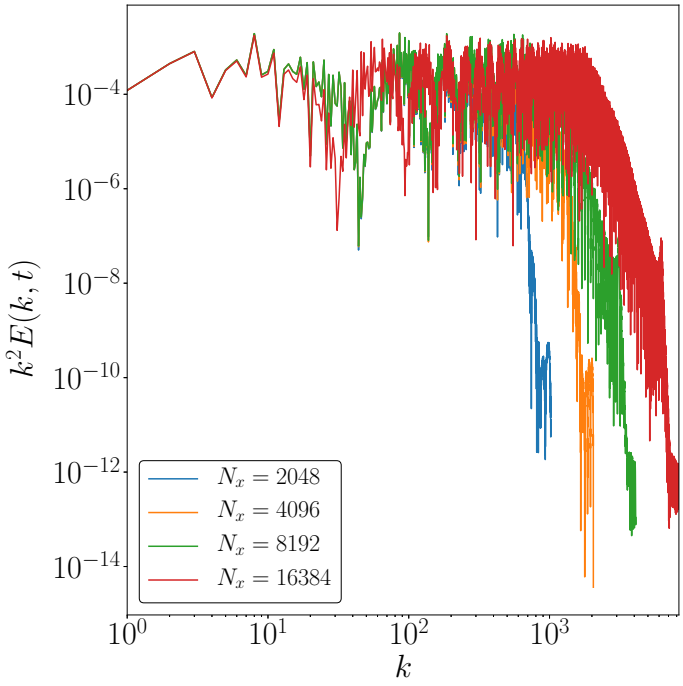

Figure 3.11: $E(k,t)$ at $t = 10$ for different N_x

As expected, the greater N_x, the larger the inertial spectrum becomes. Naturally, the formation time of the first shock wave is independent of the spatial discretisation and always equal to $t = 1.8$.

3.3.2 Thermodynamic perturbations

In this section, the initial kinetic energy is set to zero, meaning $u_0 = 0$ over the domain, while thermodynamic quantities, i.e. density and temperature are imposed as perturbations of the initial state.
When a thermodynamic perturbation of uniform entropy is imposed at $t = 0$, the flow behaves much like in the case presented in section 3.3.1.
In fact, it was shown in section 3.1 that a mapping between the Navier-Stokes equations and the Burgers equation exists whether certain hypotheses are respected. In particular, a solution was found as a perturbation of a simple wave for which all thermodynamic variables can be written as functions of one single variable. A simple wave has uniform entropy and it originates from a homoentropic initial condition.

In order for the initial state to be homoentropic over the one-dimensional domain, the temperature and the specific volume must vary according to the following:

$$T\vartheta^{\gamma-1} = const \tag{3.19}$$

If the initial specific volume ϑ_0 is a signal of given energy content, T_0 is retrieved from (3.19) to have uniform entropy s_0 (see figure 3.12).

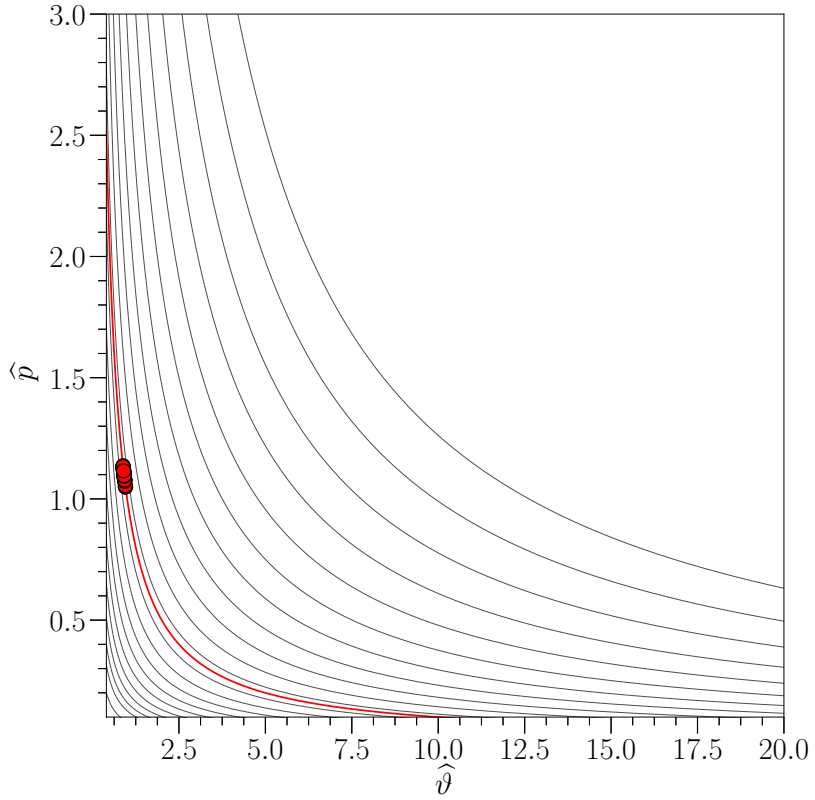

The light grey lines represent the isentropes, the red-filled points corresponding to the initial thermodynamic state of each point x lie on the red isentrope

Figure 3.12: *Simulation 2A*: initial state in the $p - \vartheta$ diagram

Simulation 2A has the following characteristics: ϑ_0 is a signal of given spectrum, i.e., a window in Fourier space of constant amplitude 10^{-2} from wave number $k = 1$ to $k = 10$, and mean value $\overline{\vartheta}_0 = 0.9091$. The temperature T_0 varies according to equation (3.19) and its mean value is $\overline{T}_0 = 1.001$; the specific heat capacity of the gas is $\gamma = 1.001$. *Simulation 2A* ran on 4 cores. The spatial domain is discretised by 4096 points; the solution was computed from $t = 0$ to $t = 1000$ with $\Delta t = 10^{-4}$ and 10^7 time steps. Table 3.2 summarises the parameters employed for *simulation 2A*.

The time-space evolution of velocity is drawn on a $x-t$ diagram (figure 3.13). As for the velocity perturbation case, shocks are formed inside the domain after a certain time; these shocks interact while the perturbation evolves in the sawtooth solution.

Sectional views of the $x - t$ diagram show the velocity at a given instant of time; they highlight how the perturbation evolves and how it finally converges to the Burgers solution (see figure 3.14b). In addition, by looking at those views, it is possible to spot the formation time of the first shock, i.e. $t_{shock} = 1.8$ (see figure 3.14a). t_{shock} does not change between *simulation 1* and *simulation 2A*.

The energy spectrum at time $t = 1000$ (see figure 3.15) is again proportional to k^{-2}, although it aligns to the k^{-2} line long before at $t \simeq 2$. The shock waves appearing in the velocity field–formed by a thermodynamic perturbation–dominate the inertial range. This means that the Burgers-like

Table 3.2: Homoentropic perturbation for a perfect gas: parameters employed

Parameter	Value
u_0	0
ϑ_0	perturbation
$\overline{\vartheta}_0$	0.9091
T_0	perturbation
$\overline{T}_0$	1.001
γ	1.001
N_x	4096
N_t	10^7
Δt	10^{-4}
t_{final}	1000

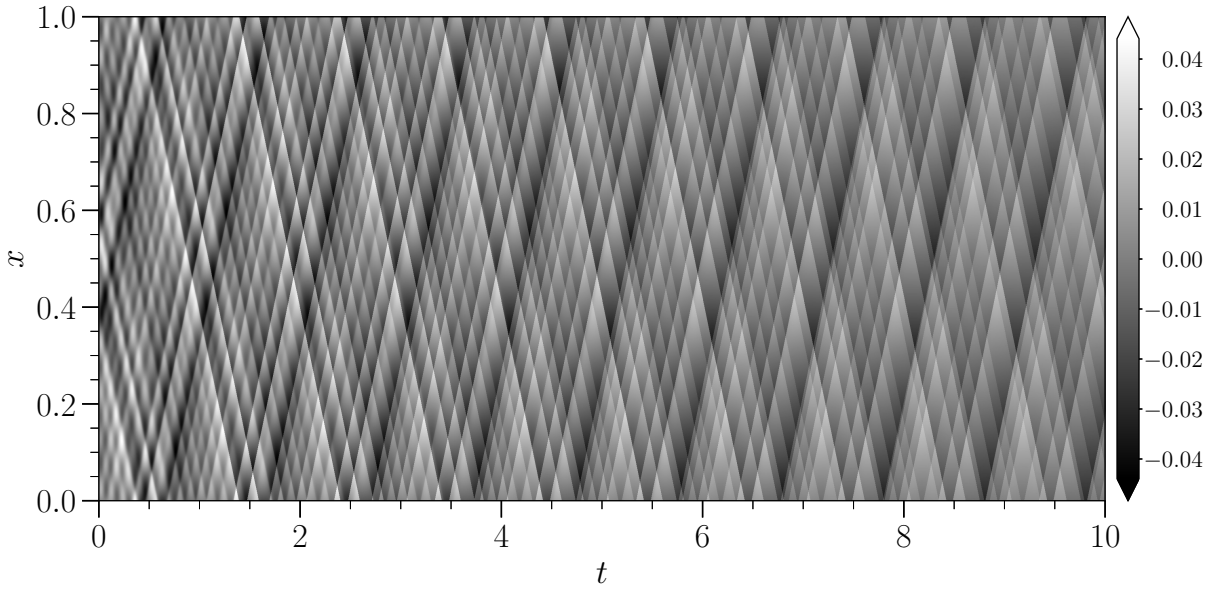

Figure 3.13: *Simulation 2A*: velocity evolution in the $x - t$ diagram for $t \in [0; 10]$

behaviour that leads to the well-known sawtooth shape dominates $E(k, t)$, whatever the initial perturbation is as long as homoentropic. This result will be later extended to non-ideal gases.

The mean spectrum evolves in time the same way it did in *simulation 1*. Figure 3.16 depicts its allure; two dashed lines indicate the formation time of the first shock, $t = 1.8$, and the convergence time to the Burgers solution, $t = 26$. In addition, once the flow is converged to the Burgers-like solution, $E_{mean}(t)$ decreases as $1/t^2$.

Let us consider another situation where only ϑ_0 varies along the space domain and T is kept constant: this initial state coincides with an isothermic perturbation. In the particular case of a dense gas for which $\gamma \to 1$ (see Thompson and Lambrakis [16]) the isotherm converges towards the isentrope, as depicted by figure 3.17.

The gas used for *Simulation 2B* has specific heat capacity γ equal to 1.001; ϑ_0 is a signal having the same spectral characteristics as the initial specific volume of *simulation 2A*. The initial temperature is set constant and equal to 1.001. *Simulation 2B* ran on 4 cores. The spatial

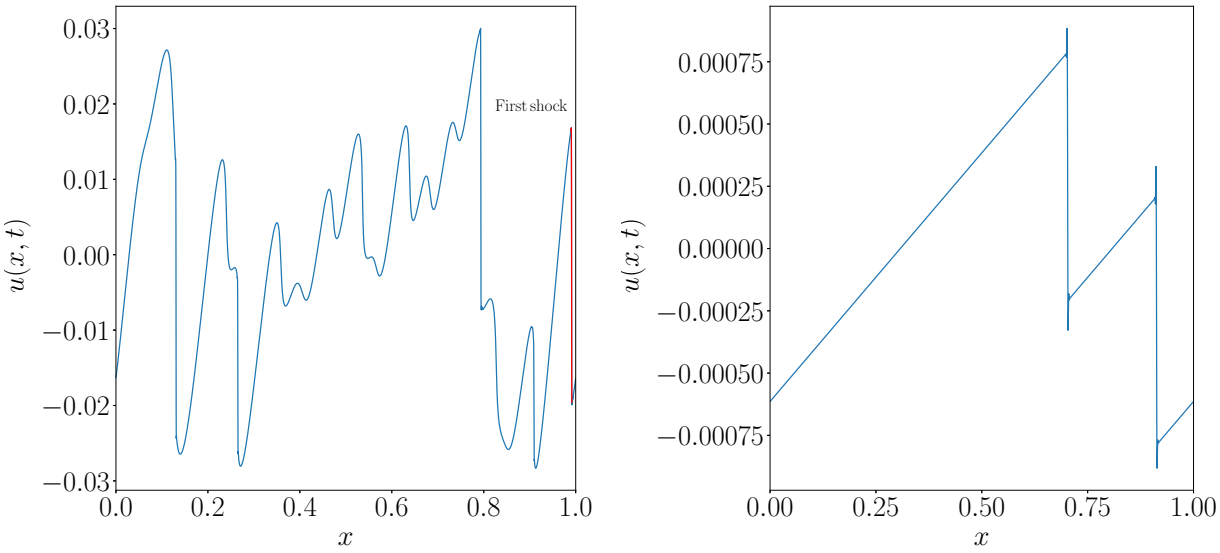

(a) Velocity as a function of x at $t = 1.8$

(b) Velocity as a function of x at $t = 1000$

Figure 3.14: *Simulation 2A*: sectional views of the $x - t$ diagram

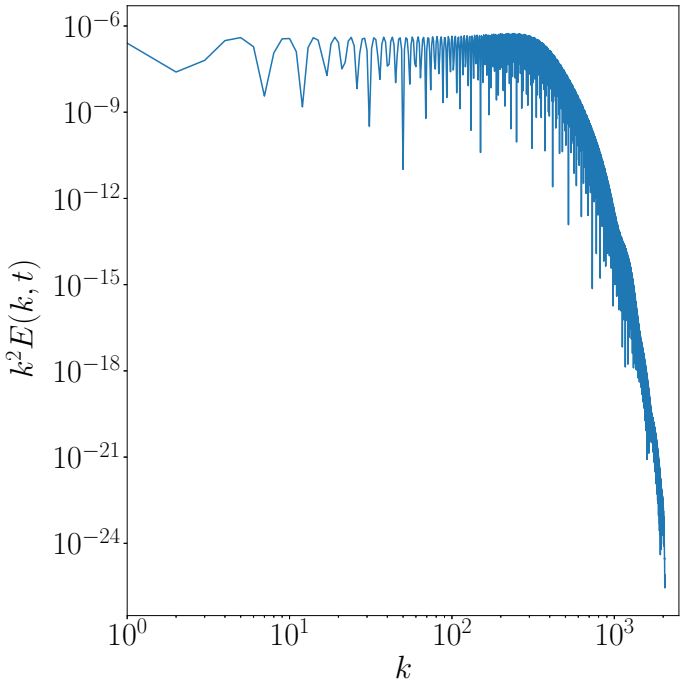

Figure 3.15: *Simulation 2A*: spectrum times k^2 at $t = 1000$

domain is discretised by 4096 points; the solution was computed from $t = 0$ to $t = 1000$ with $\Delta t = 10^{-4}$ and 10^7 time steps. Table 3.3 summarises the parameters employed for *simulation 2B*.

The time-space evolution of velocity is drawn on the $x-t$ diagram of velocity (figure 3.18). Since

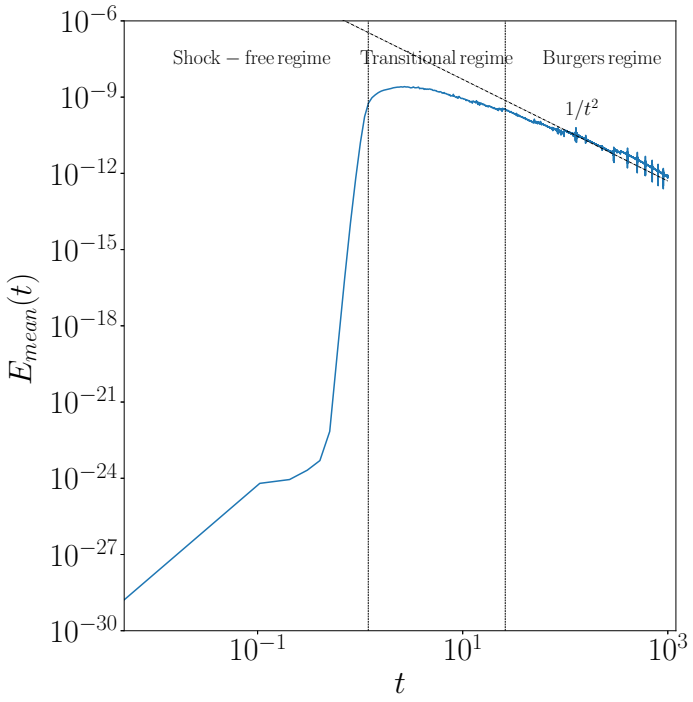

Figure 3.16: *Simulation 2A*: mean spectrum as a function of time for $t \in [0; 1000]$

Table 3.3: Specific volume perturbation for a perfect gas: parameters employed

Parameter	Value
u_0	0
ϑ_0	perturbation
$\overline{\vartheta}_0$	0.9091
T_0	1.0713
γ	1.001
N_x	4096
N_t	10^7
Δt	10^{-4}
t_{final}	1000

the initial condition is very similar to *simulation 2A*, the resulting velocity field will be alike.

The main difference between *simulation 2A* and *simulation 2B* is illustrated by figure 3.20. Indeed, the formation time of the first shock ($t_{shock} = 1.4$) is slightly smaller for the former (see figure 3.19), since shocks tend to develop before when the flow is initially non-homoentropic.

3.3.3 Is the non-linear acoustics approximation justified?

Section 3.1 develops the theoretical basis that justifies the mapping between the one-dimensional Navier-Stokes equations and the Burgers equation. The whole reasoning is built on a strong hypothesis, namely, small perturbation. In practice, non-linear acoustic waves propagate inside the domain.

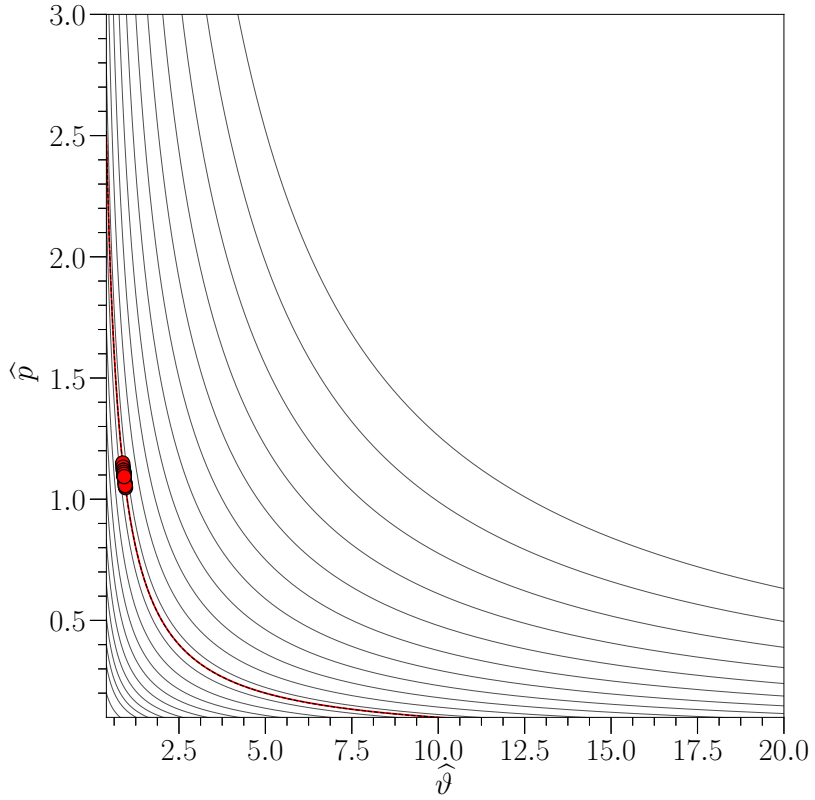

The light grey lines represent the isentropes, the red-filled points corresponding to the initial thermodynamic state of each point x lie on the red isotherm. Since $\gamma = 1.001$ it almost coincides with the black dashed isentrope.

Figure 3.17: *Simulation 2B*: initial state in the $p - \vartheta$ diagram

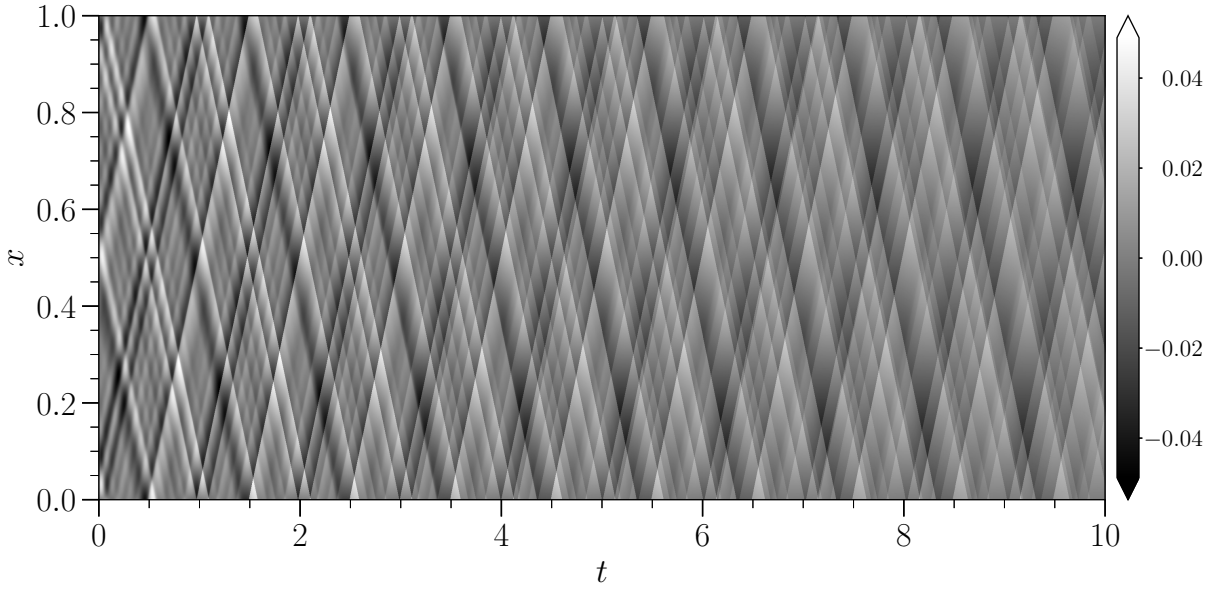

Figure 3.18: *Simulation 2B*: velocity evolution in the $x - t$ diagram for $t \in [0; 10]$

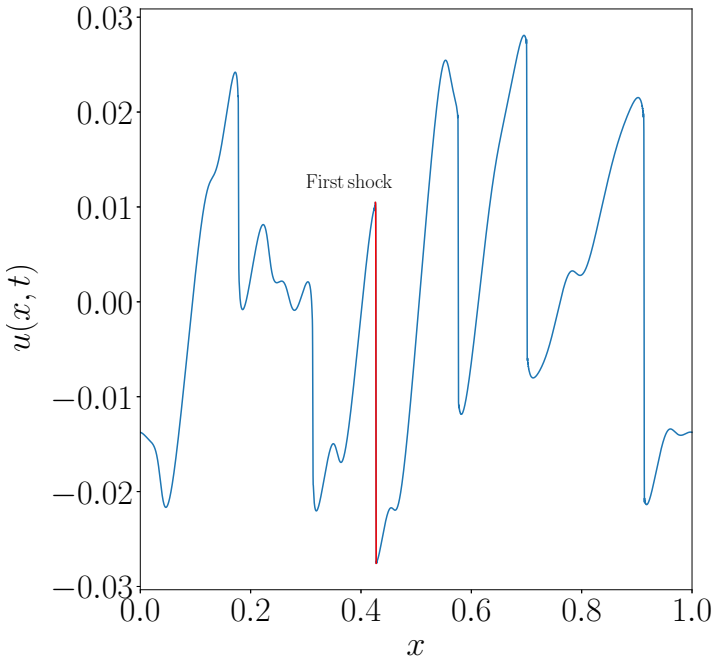

Figure 3.19: *Simulation 2B*: velocity as a function of x at $t = 1.4$

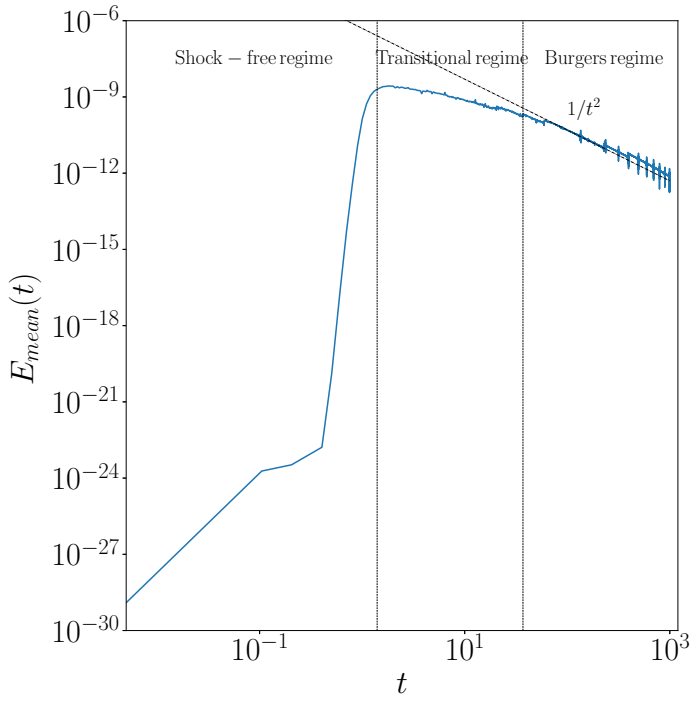

Figure 3.20: *Simulation 2B*: mean value of the inertial range as a function of time for $t \in [0; 1000]$

The solution can be written as the sum of left- and right-travelling sine waves, each of them corresponding to a mode of the linearised Euler system. The two-dimensional Fourier transform makes possible visualising these modes that distribute within a cone, whose edges are $k = \pm f/c_{min} f$ and $k = \pm f/c_{max}$[3] where:

$$\begin{aligned} c_{min} &= \min_{\forall t \text{ and } \forall x} c(x,t) \\ c_{max} &= \max_{\forall t \text{ and } \forall x} c(x,t) \end{aligned} \tag{3.20}$$

f indicates the frequency and k the wave number. Figure 3.21 shows the amplitude spectrum of the two-dimensional Fourier transform of *simulation 1*. The 2D spectrum does not lie entirely within the two cones since shock waves, though weak, sweep the domain. Nevertheless, we can state that the small perturbation hypothesis is respected.

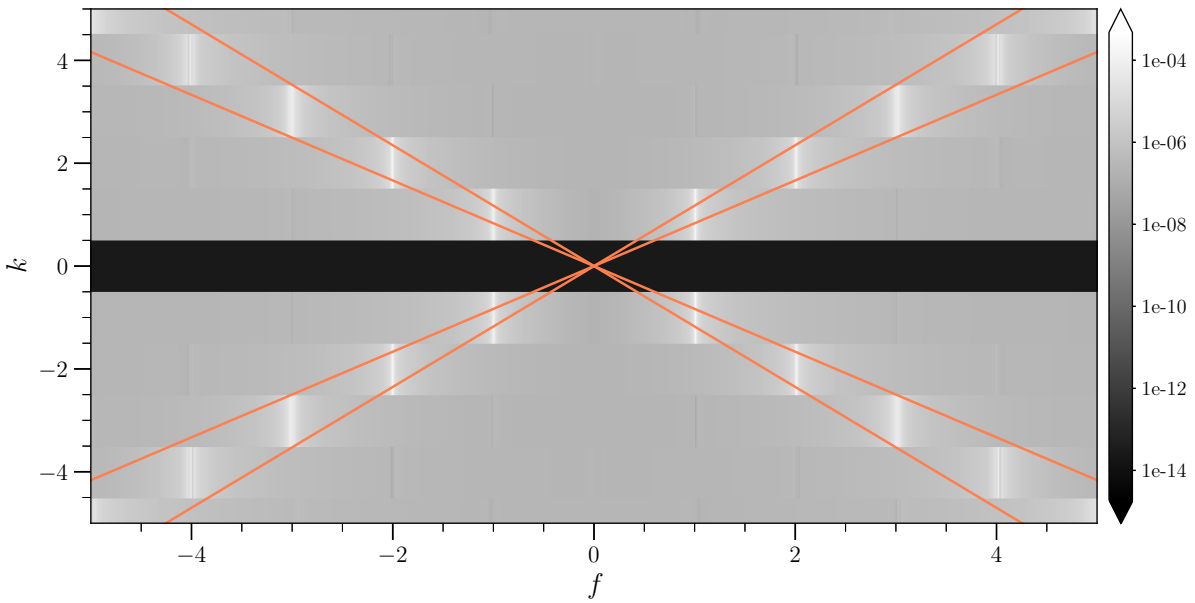

The values of the 2D Fourier transform are represented on a logarithmic scale. The orange lines correspond to the $k = \pm f/c_{min}$ and $k = \pm f/c_{max}$ curves. Pyhton `fft2d` function allocates the mean-value at $k = 0$–which is null for *simulation 1*. This justifies the horizontal black stripe. The k-axis is clipped from -5 to $+5$.

Figure 3.21: *Simulation 1*: two-dimensional Fourier transform

[3] This result was largely expected since the linearised-Euler-system eigenvalues are $u \pm c$ and u.

3.4 From the one-dimensional Navier-Stokes equations to the Burgers equation: viscous numerical simulations

This section focuses on the effect of bulk viscosity. A viscous version of `Compreal` has been used. In fact, a diffusive term is added to the Euler equations which, in one dimension, become:

$$\begin{cases} \dfrac{\partial \rho}{\partial t} + \dfrac{\partial \rho u}{\partial x} = 0 \\ \dfrac{\partial \rho u}{\partial t} + u\dfrac{\partial \rho u}{\partial x} + \rho u \dfrac{\partial u}{\partial x} = -\dfrac{\partial p}{\partial x} + \mu_b \dfrac{\partial^2 u}{\partial x^2} \\ \dfrac{\partial \rho e_t}{\partial t} + \dfrac{\partial}{\partial x}\left(\rho e_t u\right) = -\dfrac{\partial p u}{\partial x} + \mu_b \dfrac{\partial}{\partial x}\left(u\dfrac{\partial u}{\partial x}\right) \end{cases} \tag{3.21}$$

In this one-dimensional framework, the effect of bulk viscosity is indeed equivalent to that of shear viscosity. Nevertheless, μ is set to zero. In addition, no heat exchange appears inside the total-energy equation: the flow is adiabatic. The dimensionless expression of system (3.21) is (see section 3.2.1):

$$\begin{cases} \dfrac{\partial \widehat{\rho}}{\partial \widehat{t}} + \dfrac{\partial \widehat{\rho}\widehat{u}}{\partial \widehat{x}} = 0 \\ \dfrac{\partial \widehat{\rho}\widehat{u}}{\partial \widehat{t}} + \widehat{u}\dfrac{\partial \widehat{\rho}\widehat{u}}{\partial \widehat{x}} + \widehat{\rho}\widehat{u}\dfrac{\partial \widehat{u}}{\partial \widehat{x}} = -\dfrac{\partial \widehat{p}}{\partial \widehat{x}} + \dfrac{1}{Re_b}\dfrac{\partial^2 \widehat{u}}{\partial \widehat{x}^2} \\ \dfrac{\partial \widehat{\rho}\widehat{e_t}}{\partial \widehat{t}} + \dfrac{\partial}{\partial \widehat{x}}\left(\widehat{\rho}\widehat{e_t}\widehat{u}\right) = -\dfrac{\partial \widehat{p}\widehat{u}}{\partial \widehat{x}} + \dfrac{1}{Re_b}\dfrac{\partial}{\partial \widehat{x}}\left(\widehat{u}\dfrac{\partial \widehat{u}}{\partial \widehat{x}}\right) \end{cases} \tag{3.22}$$

where:

$$\mathrm{Re}_b = \frac{\rho_{ref} u_{ref} L_{ref}}{\mu_b}$$

is the bulk Reynolds number. `Compreal` allows to impose Re_b which in turn is inversely proportional to μ_b. Hence, an increasing Reynolds number means a decreasing viscosity.
Chapter 2 has already dealt with the viscosity effect on the asymptotic solution to the Burgers equation. It showed that shock waves are smoothed out as μ increases. In fact, the shock wave thickness–where diffusive phenomena are more intense–depends on μ: the greater it is, the more the shock wave is smoothed out.
Indeed, this affects the energy spectrum, since high-frequency contents are to be filtered out if one wants to obtain a smoother solution.

Hereunder, we show how μ_b affects *simulation 1* behaviour. From the very same initial conditions, simulations ran with different values of bulk Reynolds number, namely $Re_b = 6000, 8000, 10000, 20000, 50000, 100$
The convergence was verified in each case by looking at the energy spectrum. In fact, given a number of points N_x, Re_b should not be too large as the simulation may diverge. Therefore, simulations were carried out with increasing N_x for a given value of bulk viscosity; if converged, the solution would present the same energy spectrum at a given time.
Firstly, the space-time evolution of the velocity (see figure 3.22) shows how the flow forms once more the typical diamond structures. The sharp edges representing the travelling shock waves are smoother. The dissipative phenomena mostly happen in the shock layer whose thickness increases as μ_b increases.

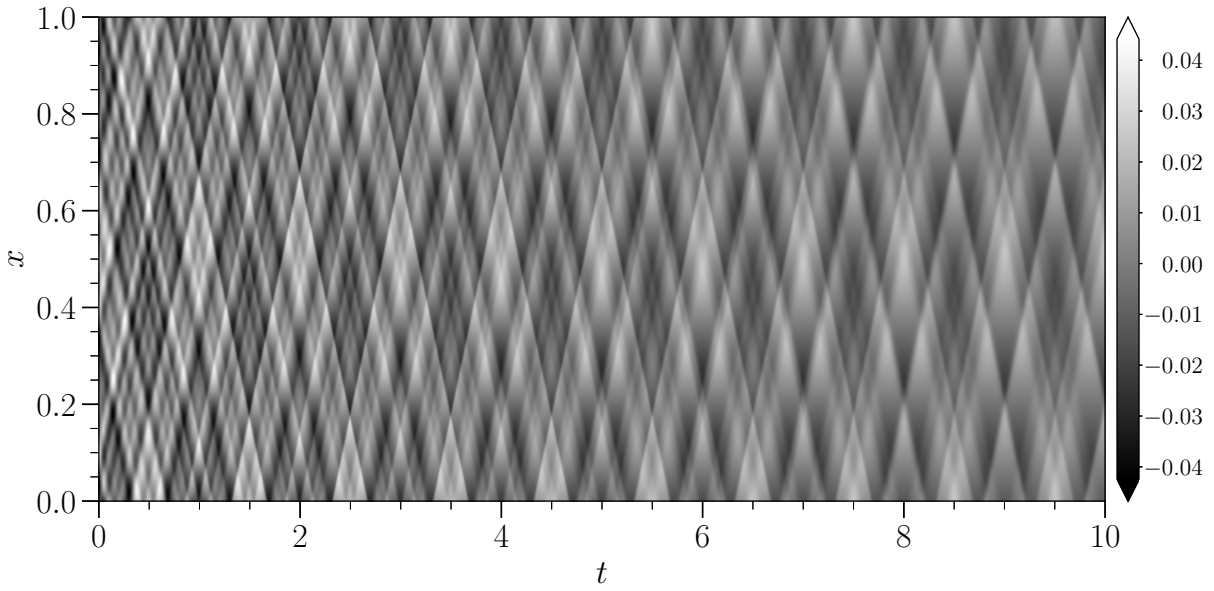

Figure 3.22: *Simulation 1*: velocity evolution in the $x-t$ diagram for $t \in [0;10]$ and $Re_b = 6000$

To better visualise this behaviour, figure 3.23 depicts a cross-view of the $x-t$ diagram at $t = 10$. The solution between two successive discontinuities is not affected by the increasing contribution of the diffusive term, while the shock waves spread out.

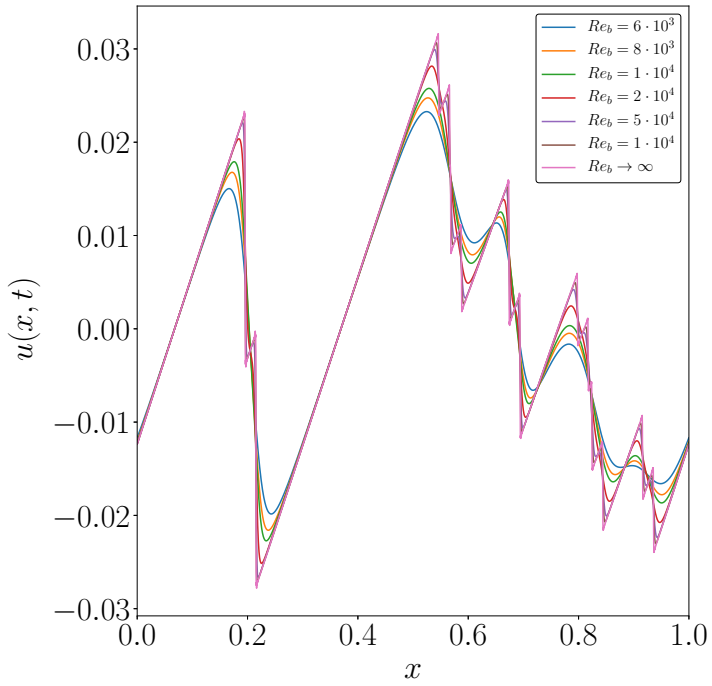

Figure 3.23: Velocity as a function of time at $t = 10$ for different values of Re_b

As far as the energy spectrum $E(k,t)$ is concerned, the effect of viscosity is manifest (see figure

3.24)[4]. Higher wave numbers are cut out and the higher the viscosity, the more this effect is intense. There exists a cut-off wave number k_{cut} whose value decreases at higher μ_b. The kinetic energy is dissipated below this critical wave number by the shock waves sweeping the domain, where diffusive effects are stronger. When the shock wave is more spread out, k_{cut} is smaller and its inverse, the dissipative scale, is greater. Eventually, we can claim that–in one dimension–the dissipative scale is strongly related to the shock waves thickness.

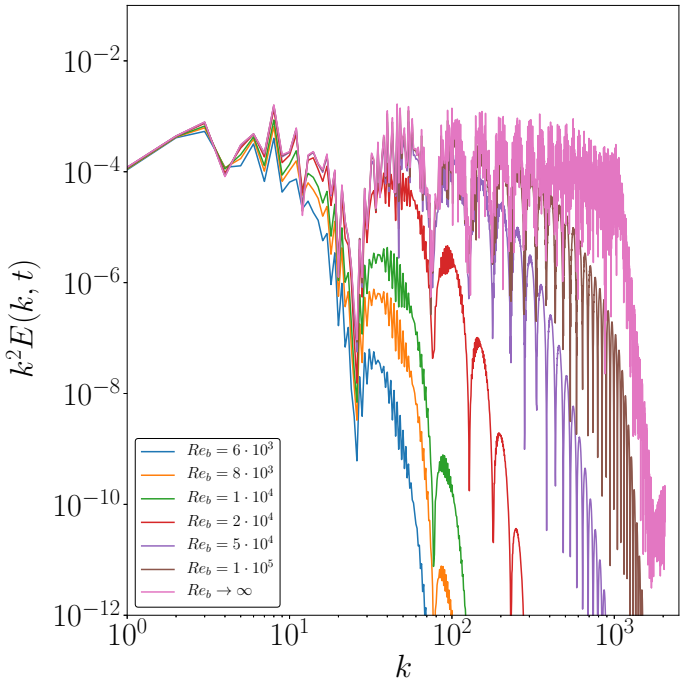

Figure 3.24: Energy spectrum times k^2 at $t = 10$ for different values of Re_b

Finally, we can point out that the k^{-2} slope of the inertial spectrum is not preserved in the viscous case. If $\mu_b = \delta$, where δ is a small enough value, the -2 exponent decreases. Chorin [6] proved that the viscosity affects indeed the energy spectrum which no longer is proportional to k^{-2}. Moreover, he provides a correction to the exponent. Nevertheless, it applies to a particular initial condition which has a hyperbolic-tangent shape. In fact, any correction strongly depends on the chosen initial condition and its energy spectrum: it is impossible to retrieve a universal law. This feature has been equally observed for two-dimensional flows by Professor Touber's research team.

As far as the phase is concerned, the bulk viscosity does not have any influence over its spectrum–similarly to the results obtained for the Burgers equation (see section 2.2.3).

[4]The energy spectrum has been clipped below 10^{-12}.

Part 4

Dynamic and spectral properties of one-dimensional non-ideal flows

In this chapter the results of chapter 3 are extended to non-ideal gases described by the van der Waals equation of state. Whilst this section is largely inspired by [10], it shows new interesting features of the non-ideal-gases energy spectrum. Once again, it exhibits an inverse proportionality to the square of the wave number even when the one-dimensional flow does not converge to the Burgers-like solution. In addition, by imposing the initial conditions in a certain region of the $p - \vartheta$ diagram, we demonstrate that the appearance of shock waves is retarded as much as possible. This might have practical applications for the design of self-driving-cars controllers and for experimental essays.

4.1 From the one-dimensional Navier-Stokes equations to the Burgers equation: theoretical background

The Navier-Stokes equations (1.1) can be rewritten for the one-dimensional case as:

$$\begin{cases} \dfrac{\partial \rho}{\partial t} + u\dfrac{\partial \rho}{\partial x} + \rho\dfrac{\partial u}{\partial x} = 0 \\ \rho\left(\dfrac{\partial u}{\partial t} + u\dfrac{\partial u}{\partial x}\right) + \dfrac{\partial p}{\partial x} = \left(\dfrac{4}{3}\mu + \lambda\right)\dfrac{\partial^2 u}{\partial x^2} \\ \rho T\left(\dfrac{\partial s}{\partial t} + u\dfrac{\partial s}{\partial x}\right) = \left(\dfrac{4}{3}\mu + \lambda\right)\left(\dfrac{\partial u}{\partial x}\right)^2 + k\dfrac{\partial^2 T}{\partial x^2} \end{cases} \tag{4.1}$$

where the entropy equation takes over the energy equation in accordance with section 1.1.4. Because our major concern is the lossless limit with μ, μ_b and k null, system (4.1) must be supplemented by the shock jump conditions:

$$\begin{cases} a[\rho] = [\rho u] \\ (u_s - u_a)(u_s - u_b) = \dfrac{[p]}{[\rho]} \\ [h] = \dfrac{1}{2}\left(\dfrac{1}{\rho_a} + \dfrac{1}{\rho_b}\right)[p] \\ [s] \geq 0 \end{cases} \tag{4.2}$$

where h and u_s are the specific enthalpy and the shock speed respectively. The brackets denote jumps, a and b refer to conditions after and before the shock.

The unperturbed state (subscript u) will be taken to be uniform and at rest $u = 0$, $\rho = \rho_u$ and $s = s_u$. It is convenient to introduce the dimensionless quantities:

$$\begin{aligned}
&\widehat{x} = \frac{x}{L},\ \widehat{t} = \frac{c_u}{L}t,\ \widehat{u} = \frac{u}{c_u},\ \widehat{a} = \frac{a}{c_u},\\
&\widehat{s} = \frac{s}{c_{v,u}},\ \widehat{p} = \frac{p - p_u}{\rho c_u^2},\ \widehat{\rho} = \frac{\rho}{\rho_u},\ \widehat{T} = \frac{T}{T_u},\ \widehat{h} = \frac{h}{c_u^2},\\
&\widehat{\mu_b} = \frac{\mu_b}{\mu_{b,u}},\ \widehat{\mu} = \frac{\mu}{\mu_u},\ \widehat{k} = \frac{k}{k_u}
\end{aligned} \tag{4.3}$$

where L is the characteristic wavelength. Substitution of (4.3) into (4.1) yields:

$$\begin{cases}
\dfrac{\partial \widehat{\rho}}{\partial \widehat{t}} + \widehat{u}\dfrac{\partial \widehat{\rho}}{\partial \widehat{x}} + \widehat{\rho}\dfrac{\partial \widehat{u}}{\partial \widehat{x}} = 0\\
\widehat{\rho}\left(\dfrac{\partial \widehat{u}}{\partial \widehat{t}} + \widehat{u}\dfrac{\partial \widehat{u}}{\partial \widehat{x}}\right) + \dfrac{\partial \widehat{p}}{\partial \widehat{x}} = \dfrac{1}{Re}\left(\dfrac{4}{3}\widehat{\mu} + \dfrac{\mu_{b,u}}{\mu_u}\mu_b\right)\dfrac{\partial^2 \widehat{u}}{\partial \widehat{x}^2}\\
\widehat{\rho}\widehat{T}\left(\dfrac{\partial \widehat{s}}{\partial \widehat{t}} + \widehat{u}\dfrac{\partial \widehat{s}}{\partial \widehat{x}}\right) = \dfrac{1}{Re}\left[E\left(\dfrac{4}{3}\widehat{\mu} + \dfrac{\mu_{b,u}}{\mu_u}\mu_b\right)\left(\dfrac{\partial \widehat{u}}{\partial \widehat{x}}\right)^2 + \dfrac{\gamma_u}{Pr}\widehat{k}\dfrac{\partial^2 \widehat{T}}{\partial \widehat{x}^2}\right]
\end{cases} \tag{4.4}$$

where:

$$\gamma_u = \frac{c_{p,u}}{c_{v,u}},\ Re = \frac{\rho c_u L}{\mu_u},\ Pr = \frac{\mu_u c_{pu}}{k_u},\ E = \frac{c_u^2}{T_u c_{v,u}} \tag{4.5}$$

are the ratio of the specific heats, the Reynolds, Prandtl and Eckert numbers. The jump conditions become:

$$\begin{cases}
\widehat{a}[\widehat{\rho}] = [\widehat{\rho}\widehat{u}]\\
\left(\widehat{u_s} - \widehat{u}_a\right)\left(\widehat{u_s} - \widehat{u}_b\right) = \dfrac{[\widehat{p}]}{[\widehat{\rho}]}\\
[\widehat{h}] = \dfrac{1}{2}\left(\dfrac{1}{\widehat{\rho}_a} + \dfrac{1}{\widehat{\rho}_b}\right)[\widehat{p}]\\
[\widehat{s}] \geq 0
\end{cases} \tag{4.6}$$

In the lossless limit for $Re \to \infty$, the right-hand sides of (4.4) are dropped. The Euler equations, which constitute a hyperbolic system of partial differential equations, are retrieved:

$$\begin{cases}
\dfrac{\partial \widehat{\rho}}{\partial \widehat{t}} + \widehat{u}\dfrac{\partial \widehat{\rho}}{\partial \widehat{x}} + \widehat{\rho}\dfrac{\partial \widehat{u}}{\partial \widehat{x}} = 0\\
\widehat{\rho}\left(\dfrac{\partial \widehat{u}}{\partial \widehat{t}} + \widehat{u}\dfrac{\partial \widehat{u}}{\partial \widehat{x}}\right) + \dfrac{\partial \widehat{p}}{\partial \widehat{x}} = 0\\
\widehat{\rho}\widehat{T}\left(\dfrac{\partial \widehat{s}}{\partial \widehat{t}} + \widehat{u}\dfrac{\partial \widehat{s}}{\partial \widehat{x}}\right) = 0
\end{cases} \tag{4.7}$$

In the following, approximate solutions of the governing equations describing weakly nonlinear waves are investigated. The method of characteristics applied to the previous system leads to

the following set of equations:

$$\begin{cases} \widehat{\rho}\dfrac{\mathrm{d}\widehat{u}}{\mathrm{d}\widehat{t}} \pm \widehat{c}\dfrac{\mathrm{d}\widehat{\rho}}{\mathrm{d}\widehat{t}} = -\alpha\dfrac{\partial\widehat{s}}{\partial\widehat{x}} & \text{on } \dfrac{\mathrm{d}\widehat{x}}{\mathrm{d}\widehat{t}} = \widehat{u} \pm \widehat{c} \\ \dfrac{\mathrm{d}\widehat{s}}{\mathrm{d}\widehat{t}} = 0 & \text{on } \frac{\mathrm{d}\widehat{x}}{\mathrm{d}\widehat{t}} = \widehat{u} \end{cases} \tag{4.8}$$

where:

$$\alpha = \frac{c_{v,u}}{\rho_u c_u^2}\frac{\beta T \rho c^2}{c_p},\ \beta = -\frac{1}{\rho}\left(\frac{\partial\rho}{\partial T}\right)_p. \tag{4.9}$$

Since thermoviscous effects are neglected, the entropy is constant on particle lines. However, it increases across a shock front. As shown by Kluwick [10], [11], [12] and Bethe [13], if the unperturbed state is assumed to be characterised by a point in the transition zone, i.e.:

$$\widehat{\rho} = 1,\ \widehat{s} = \widehat{s}_u,\ \Gamma_u = \varepsilon\widehat{\Gamma},\ \widehat{\Gamma} = \mathcal{O}(1),\ \Lambda_u = \frac{\widehat{c}_u}{\widehat{\rho}_u}\left(\frac{\partial\widehat{\Gamma}}{\partial\widehat{\rho}}\right)_{\widehat{s}} = \mathcal{O}(1) \tag{4.10}$$

then it can be shown that the lowest order expression for the entropy jumps across weak shocks is given by:

$$[s] = \frac{c_u^2[\rho]^3}{6T_u\rho_u^3}\left[\Gamma_u + \frac{\Lambda_u}{2}\left(\frac{\rho_b - \rho_u}{\rho_u} + \frac{\rho_a - \rho_u}{\rho_u}\right)\right] + o\left(\left(\frac{\rho - \rho_u}{\rho_u}\right)^4\right). \tag{4.11}$$

Thus, in the transition zone, the entropy jump is fourth order in the density jump. Equation (4.11) is used to show that the entropy term of the first equation of system (4.8) is negligibly small when it comes to computing the leading order terms of the expansion:

$$\begin{cases} u = \varepsilon u_1 + \varepsilon^2 u_2 + \varepsilon^3 u_3 + o(\varepsilon^3) \\ \rho = 1 + \varepsilon\rho_1 + \varepsilon^2\rho_2 + \varepsilon^3\rho_3 + o(\varepsilon^3) \\ c = 1 + \varepsilon\rho_1 + \varepsilon^2\rho_2 + \varepsilon^3\rho_3 + o(\varepsilon^3) \\ \widehat{s} = \dfrac{s_u}{c_{v,u}} + \varepsilon^4 s_4 + o\left(\varepsilon^4\right) \end{cases} \tag{4.12}$$

The speed of sound $\widehat{c}$–recalling that entropy is constant–can be rewritten in terms of $\widehat{\rho}$, Γ and Λ:

$$\widehat{c}(\overline{\widehat{s}}, \widehat{\rho}) = 1 + \left(\frac{\partial\widehat{c}}{\partial\widehat{\rho}}\right)_{\overline{\widehat{s}}}\Delta\widehat{\rho} + \frac{1}{2}\left(\frac{\partial^2\widehat{c}}{\partial\widehat{\rho}^2}\right)_{\overline{\widehat{s}}}\Delta\widehat{\rho}^2 \tag{4.13}$$

that can be recast as:

$$\widehat{c}(\overline{\widehat{s}}, \widehat{\rho}) = 1 + \left(\varepsilon\widehat{\Gamma} - 1\right)\left(\varepsilon\rho_1 + \varepsilon^2\rho_2 + ...\right) + \left(1 + \frac{1}{2}\Lambda_0\right)\left(\varepsilon\rho_1 + \varepsilon^2\rho_2 + ...\right)^2 \tag{4.14}$$

By substitution of (4.12), where $\widehat{c}$ is written as (4.14), into (4.8) and by elimination of the secular terms, one obtains for a positive simple wave[1] (see Kluwick [12]):

$$\frac{\partial u_1}{\partial\tau} + \left(\widehat{\Gamma} + \frac{\Lambda_u}{2}u_1\right)u_1\frac{\partial u_1}{\partial x} = 0 \tag{4.15}$$

[1] The minus sign was discarded.

where $\tau = \varepsilon^2 t$ is the slow time. Thus, thanks to the expansion of the speed of sound, one can retrieve an equation where the fundamental derivative of gasdynamics and its derivative appear and play an important role. In practice, this method fully matches the one used at section 3.1, although, in this case, it is generalised to non-ideal gases.

Based on the value of Γ_u (or $\widehat{\Gamma}$), it is possible to distinguish two main cases:

1. $\boldsymbol{|\Gamma_u| > 1}$ (or $\boldsymbol{|\widehat{\Gamma}| \gg |\Lambda_u u_1/2|}$): equation (4.15) can be reduced to the Burgers equation, thus the perturbation will evolve in the sawtooth solution: the result predicted by the classical theory of nonlinear Acoustics (see Karpman [21] and Crigthon [7]). However, when Γ_u is negative, a phenomenon distinctive of negative nonlinearity is observed: the sawtooth is characterised by expansion shock waves. On the contrary, when $\Gamma_u > 0$ the initial condition converges to the more classical Burgers-like solution with compression shock waves.

2. $\boldsymbol{\Gamma_u \simeq 0}$: since some points of the initial perturbation evolve towards positive Γ_u whereas others towards negative Γ_u, the domain will be swept by both compression and expansion shock waves.
   Moreover, we will show that van der Waals gases develop shock waves with a maximum delay when both Γ_u and Λ_u are zero-valued.

4.2 From the one-dimensional Navier-Stokes equations to the Burgers equation: inviscid numerical simulations

In the first part of this section, viscosity is set to zero, the flow being inviscid. Two basic cases are presented: an initial velocity perturbation is imposed to the flow while the thermodynamic properties are kept constant; an initial homoentropic perturbation is imposed to the flow while the initial velocity is set to zero thus having no initial kinetic energy.

In the second part of this section, the contribution of viscosity is added thus resulting in different dynamic and spectral properties of the flow.

4.2.1 Inviscid flow: dynamic and energetic features

Section 4.1 discusses the time evolution of a small perturbation, the gas being non-ideal. Different behaviours should be observed according to the value of the fundamental derivative Γ_0 (which plays the role of Γ_u of equation (4.15)). Different asymptotic solutions are attained by the flow; this section will show that theory and numerical simulations are in accordance.

Velocity perturbation

Three simulations provide the numerical data needed for this section. Despite the same initial-velocity perturbation (see figures 4.1a and 4.1b), the convergence of the velocity field to the classical sawtooth solution strongly depends on the thermodynamic features of the flow.

Indeed, it is straightforward to distinguish three cases by looking at the $p - \vartheta$ diagram. Figure 4.2 shows the initial thermodynamic characteristics of the three simulations. These three points were accurately chosen to show how Γ_0 is the key parameter to predict the solution asymptotic shape; the specific volume $\widehat{\vartheta}$ is fixed and equal to 1.1, whereas the temperature is computed

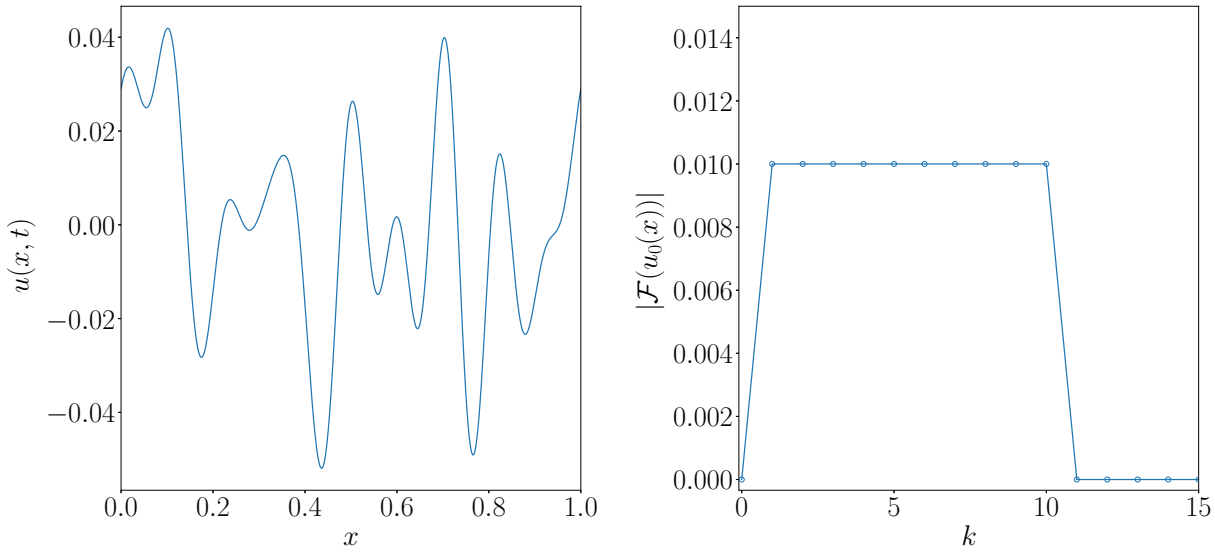

(a) Initial velocity as a function of space

(b) $u_0(x)$ discrete spectrum

Figure 4.1

by inverting equation (1.19) where Γ_0 is set to 1, 0 and -1 respectively. Table 4.1 collects the parameters employed for these simulations.

Table 4.1: Velocity perturbation for a non-ideal gas: parameters employed

	Simulation 1A	*Simulation 1B*	*Simulation 1C*
u_0	perturbation	perturbation	perturbation
$\overline{u}_0$	0	0	0
ϑ_0	1.1	1.1	1.1
T_0	1.1396	1.0189	1.0372
γ	1.001	1.001	1.001
Γ_0	1	-1	0
N_x	4096	4096	4096
N_t	10^7	10^7	10^7
Δt	10^{-5}	10^{-5}	10^{-5}
t_{final}	1000	1000	1000

In chapter 3, it is shown how the first shock is formed after a certain amount of time and how–at large t–the solution evolves in the sawtooth. When it comes to non-ideal gases, the mapping between the Burgers equation and the one-dimensional Navier-Stokes equations is not so trivial, for the fundamental derivative plays a major role. Section 4.1 has already presented the impact of Γ_0 on the asymptotic solution; simulations carried out with `Compreal` match the theoretical framework. When $\Gamma_0 = 1$, compression shock waves form and sweep the domain. The asymptotic solution looks identical to the Burgers solution. In other words, in this particular case, non-ideal gases behave like ideal gases at large t.
On the contrary, when $\Gamma_0 = -1$, expansion shock waves form. It is a typical feature of non-ideal gases and the solution at large t exhibits this unusual behaviour. Indeed, chapter 2 provides a geometrical method to draw $u(x,t)$ when $\mu \to 0$ and $t \gg 1$. It happens that between one shock

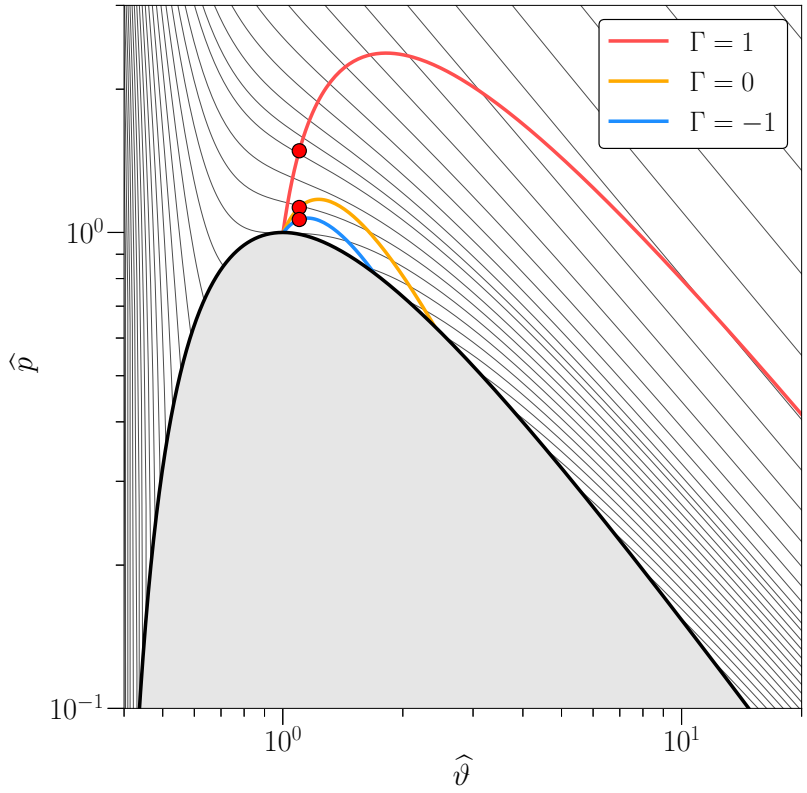

The light grey lines represent the isentropes, the simulation points are plotted on top of the iso-Γ lines

Figure 4.2: Initial thermodynamic conditions of the three simulations

and another $u(x,t) \propto 1/t$. However, when $\Gamma_0 < 0$, a negative sign appears before the non-linear term, thus leading to $u(x,t) \propto -1/t$.
For $\Gamma_0 = 0$, both compression and expansion shock waves appear thus leading to mixed non-linearity. In fact, some points of the x-domain drift, in time, towards negative values of Γ while others evolve towards positive Γ. As a result, the solution is very different from the previous ones.
Hereunder, three $x - t$ diagrams for $t \in [0; 10]$ and $\Gamma_0 = 1, -1, 0$ (see figures 4.4, 4.5 and 4.6 respectively) illustrate the evolution of velocity. If $\Gamma_0 = 1$, the discontinuities are compression shock waves thus implying a decrease in velocity (the color darkens across a shock front). In contrast, when $\Gamma_0 = -1$, expansion shock waves are visible in figure 4.5, for the velocity increases past a discontinuity. Figure 4.6 shows that both expansion and compression shock waves develop for mixed non-linearity. Furthermore, these three pictures reveal how the classical periodic diamond structure depends on the initial condition. Indeed, shock waves interact more frequently for $\Gamma_0 = 1$ than for $\Gamma_0 = -1$. This largely depends on the position of the initial condition in the $\widehat{p} - \widehat{\vartheta}$ diagram. The speed of sound $\widehat{c}_0(\widehat{T}, \widehat{\vartheta})$ at the initial thermodynamic state happens to be greater for the $\Gamma_0 = 1$ case than for the $\Gamma_0 = -1$ case. Therefore, discontinuities move faster when $\widehat{c}_0(\widehat{T}, \widehat{\vartheta})$ is greater and interact more frequently. We recall that, in the framework non-linear acoustics, shocks are weak and comparable to acoustic waves, that move at the speed of sound.

The cross-sectional views of velocity at $t = 1000$ reveal good accordance between theory and

numerical simulations (see figures 4.3a, 4.3b and 4.3c respectively). For the specific case Γ_0, the value of the fundamental derivative as a function of time is shown at $t = 1000$, the purpose being to visualise its constant change of sign.

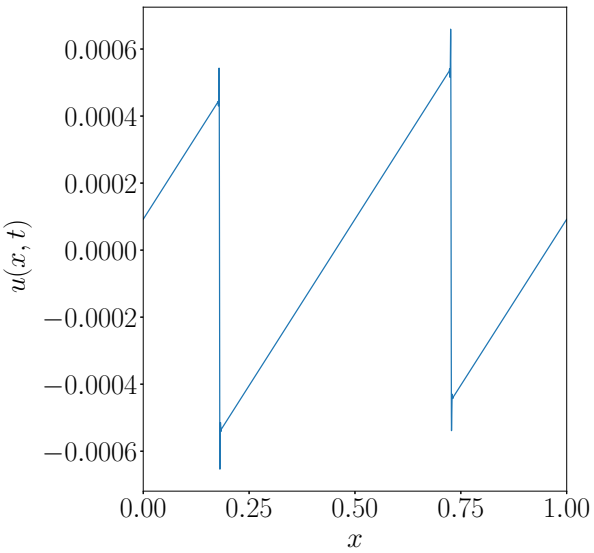

(a) Cross-sectional view of the velocity at $t = 1000$, $\Gamma_0 = 1$

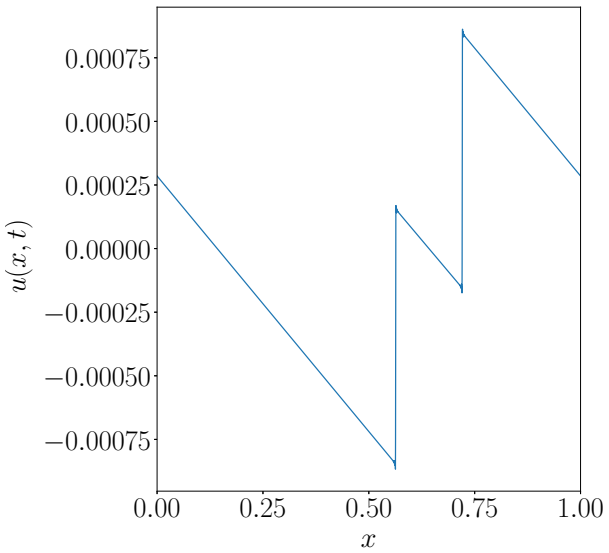

(b) Cross-sectional view of the velocity at $t = 1000$, $\Gamma_0 = -1$

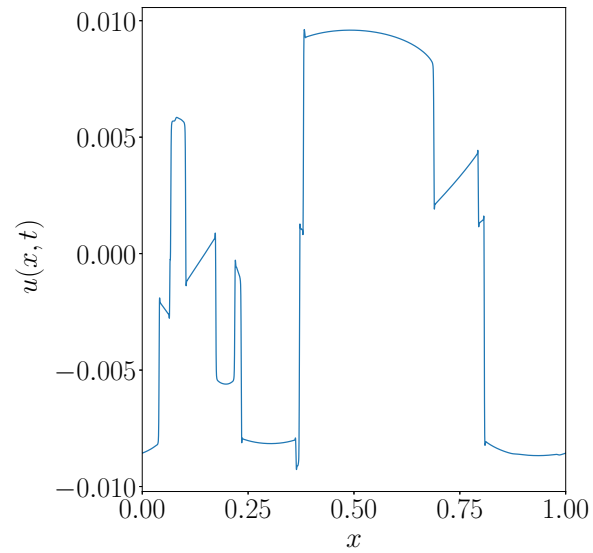

(c) Cross-sectional view of the velocity at $t = 1000$, $\Gamma_0 = 0$

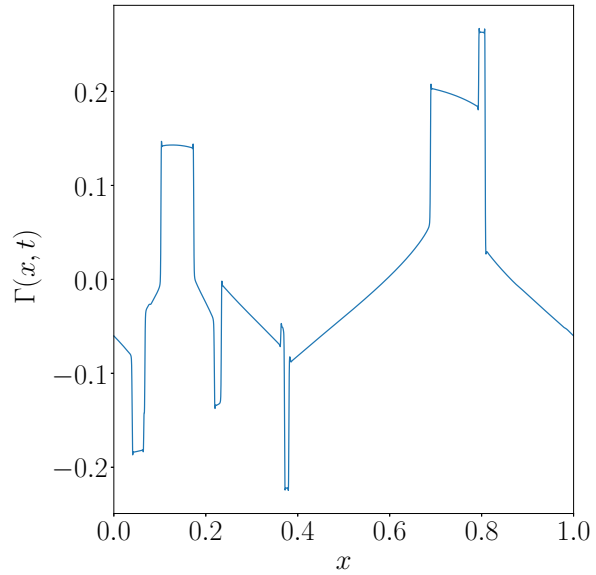

(d) Fundamental derivative at $t = 1000$ for $\Gamma_0 = 0$ as a function of space

Figure 4.3

Despite three different asymptotic solutions, the energy spectrum remains proportional to k^{-2} (see figure 4.7). Indeed, the -2 exponent is caused by discontinuities (see Gotoh [5]), whereas the shape of the velocity profile in between two shocks does not affect it. However, one can observe that the amplitude of the energy spectrum at $t = 1000$ is larger when $\Gamma_0 = 0$ thus indicating that discontinuities are stronger. This relates to the time decay of E_{mean}.

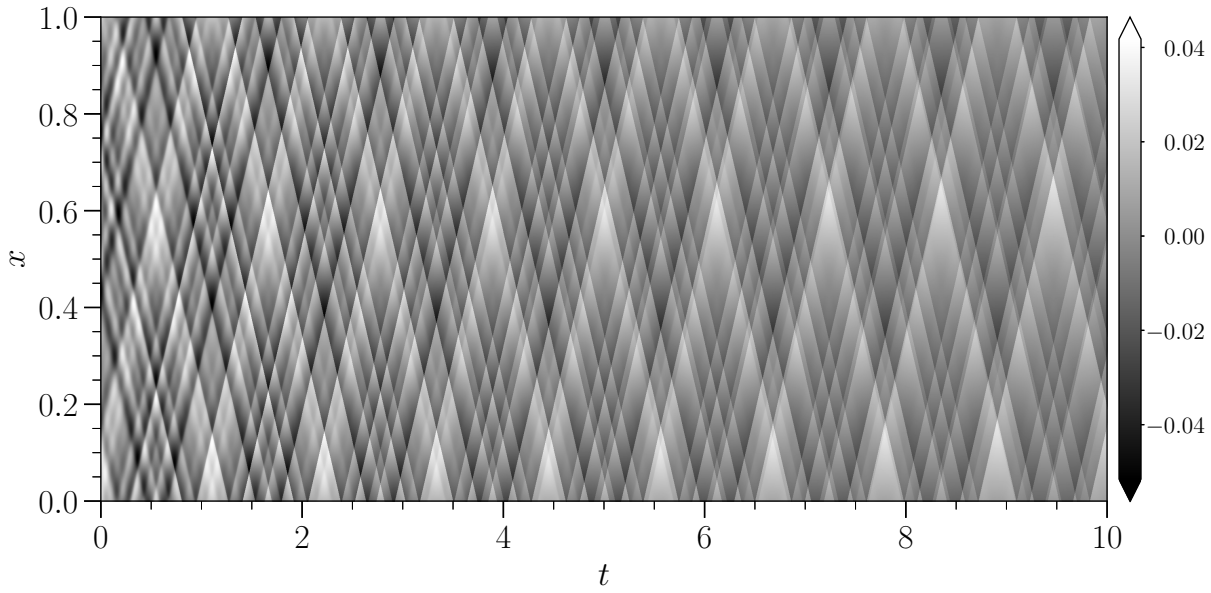

Figure 4.4: *Simulation 1A*: $x - t$ diagram for $\Gamma_0 = 1$, the colour scale represents the velocity

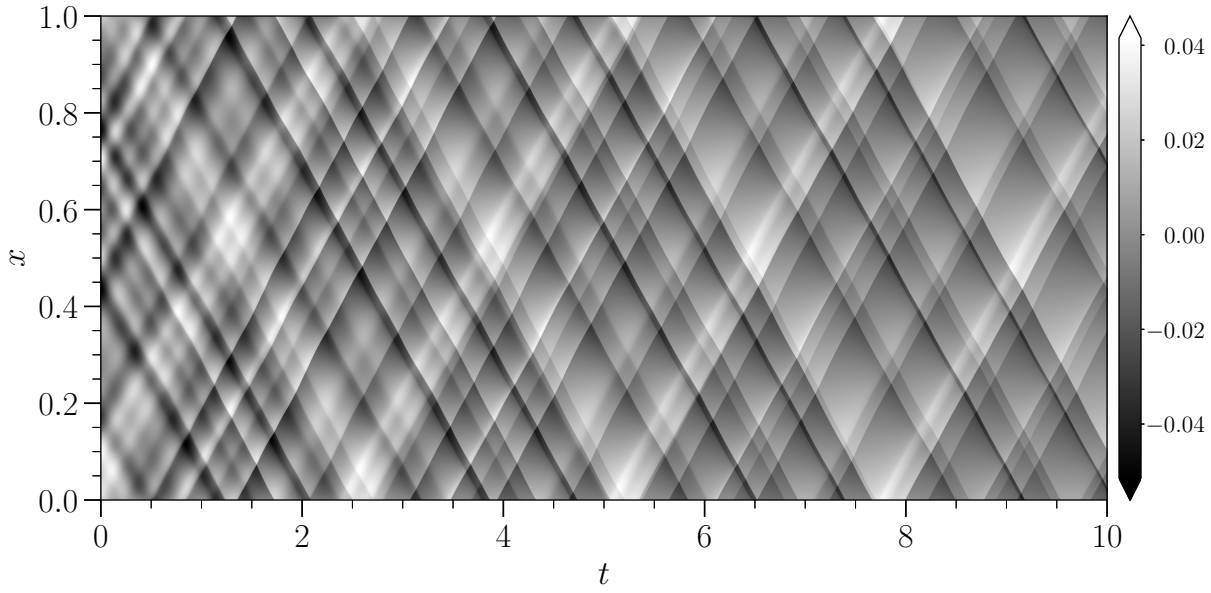

Figure 4.5: *Simulation 1B*: $x - t$ diagram for $\Gamma_0 = -1$, the colour scale represents the velocity

Figure 4.8 shows how the mean spectrum decays in time and how its asymptotic behaviour changes for $\Gamma_0 = 0$. In fact, when the asymptotic solution is expected to have a sawtooth shape, i.e. for $\Gamma_0 = 1$ and $\Gamma_0 = -1$, $E_{mean}(t)$ is proportional to $1/t^2$ for t that goes to infinity (see figures 4.8a and 4.8b). On the contrary, when both expansion and compression shockwaves appear inside the domain, E_{mean} features a proportionality to $1/t$ (see figure 4.8c). The shock strength does not decay as $1/t$ but rather as $1/t^{1/2}$, this leads to a different $E_{mean}(t)$ decay and justifies the larger amplitude of $E(k,t)$ at $t = 1000$. In effect, Kluwick [10] found that the shocks occurring at $\Gamma_0 = 0$ decay as $1/t^{1/3}$. His result is slightly different to the one reported here, but it was found for a square pulse propagating in a gas at rest.

In addition, one can infer the first-shock formation times from figure 4.8. They are collected in

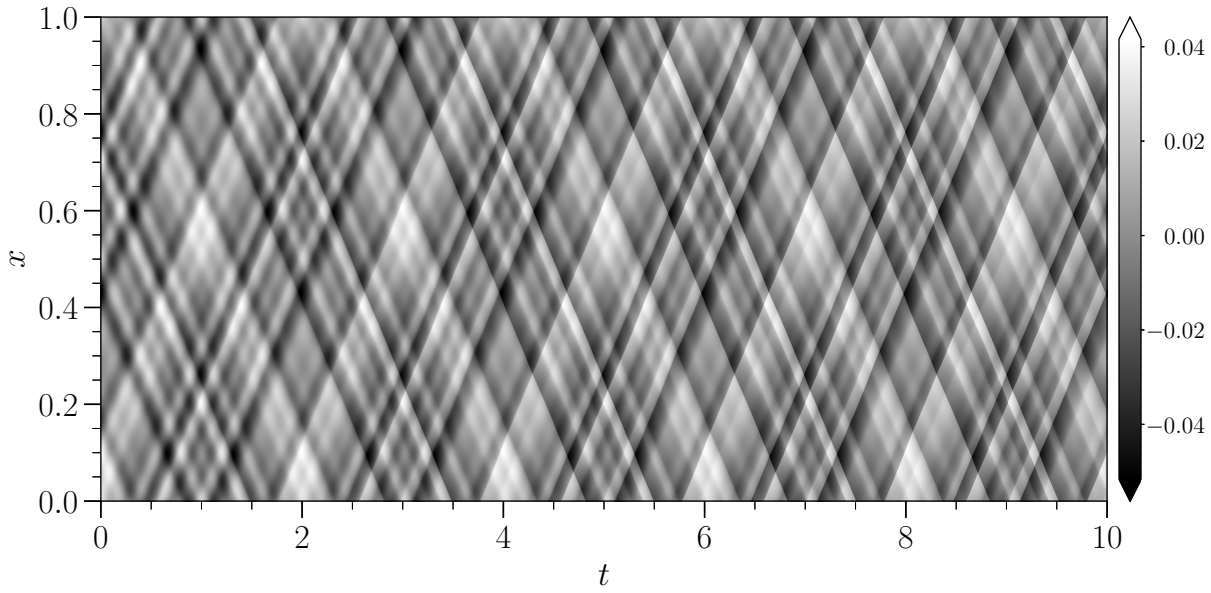

Figure 4.6: *Simulation 1C*: $x - t$ diagram for $\Gamma_0 = 0$, the colour scale represents the velocity

table 4.2.

Table 4.2: *Simulation 1*: formation times of the first shock wave

	Simulation 1A	*Simulation 1B*	*Simulation 1C*
Γ_0	1	-1	0
t_s	1.6	1.7	4.2

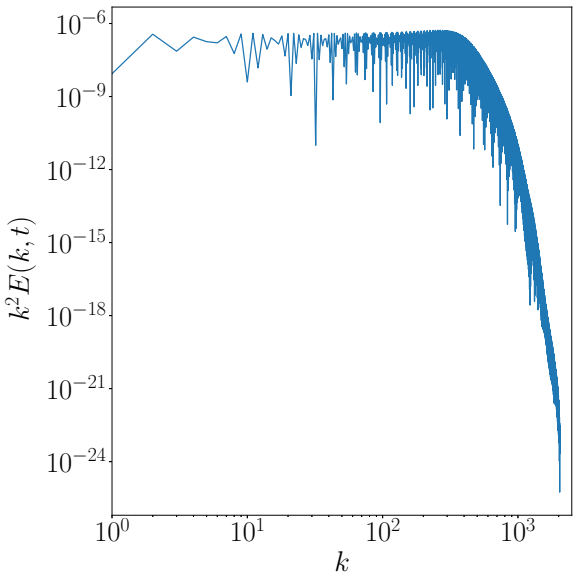

(a) *Simulation 1A*, $\Gamma_0 = 1$

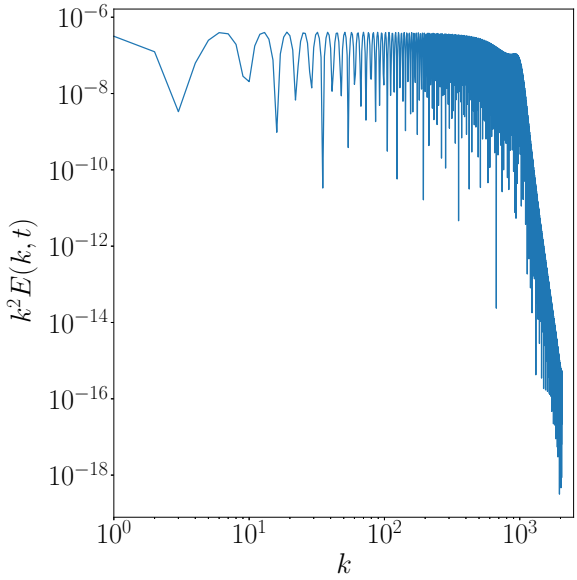

(b) *Simulation 1B*, $\Gamma_0 = -1$

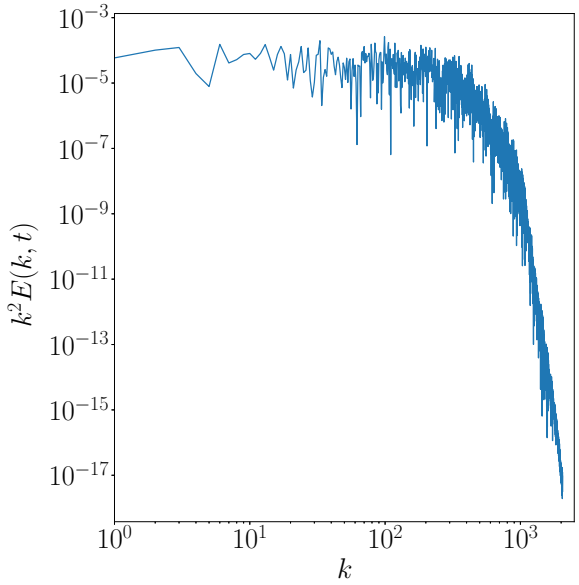

(c) *Simulation 1C*, $\Gamma_0 = 0$

Figure 4.7: *Simulation 1*: energy spectrum times k^2 as a function of k at $t = 1000$

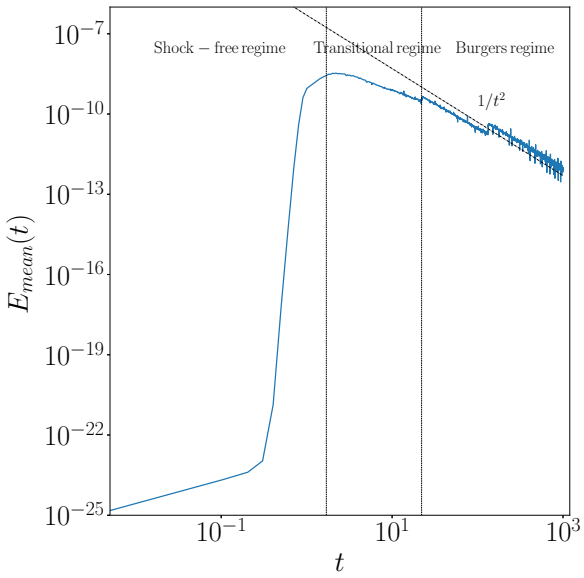

(a) *Simulation 1A*, $\Gamma_0 = 1$

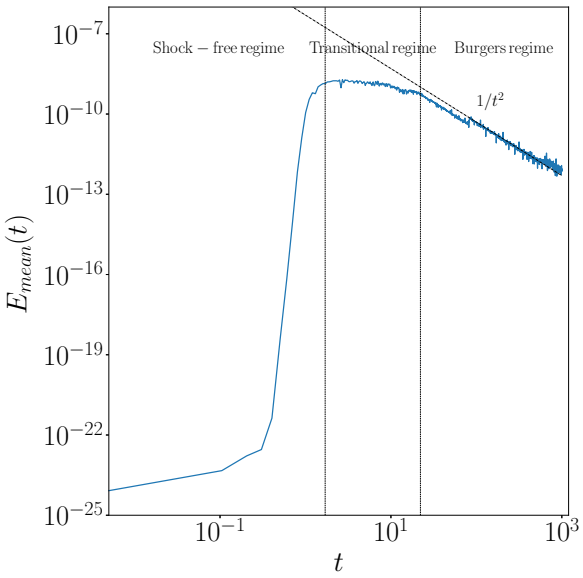

(b) *Simulation 1B*, $\Gamma_0 = -1$

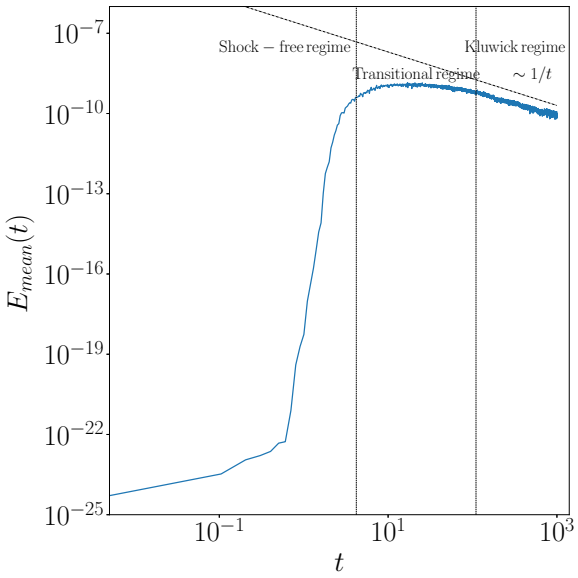

(c) *Simulation 1C*, $\Gamma_0 = 0$

Figure 4.8: *Simulation 1*: time evolution of the mean spectrum $E_{mean}(t)$

Phase alignment

The energy spectrum alone has been discussed thus far. However, the Fourier transform provides another valuable information, i.e. the phase spectrum. As discussed in sections 2.2.3 and 3.3.1, the phase tends to align as time passes. Nonetheless, since non-ideal gases are dealt with, the initial value of the fundamental derivative affects also the phase spectrum, namely:

- $\mathbf{\Gamma_0 \simeq 1}$: the solution converges to the classical sawtooth. The phase spectrum is either equal to $\pi/2$ or $-\pi/2$ (see figure 4.9). This result fully matches those obtained in sections 2.2.3 and 3.3.1.

- $\mathbf{\Gamma_0 \simeq -1}$: the solution converges to the reversed sawtooth. The Fourier series of this function resembles that of a classical sawtooth, but it is a sum of cosine waves. Therefore, at large t the phase spectrum is constant and equal to 0 or π (see figure 4.10).

- $\mathbf{\Gamma_0 \simeq 0}$: the phase does not align since the velocity does not converge to a sawtooth (see figure 4.11).

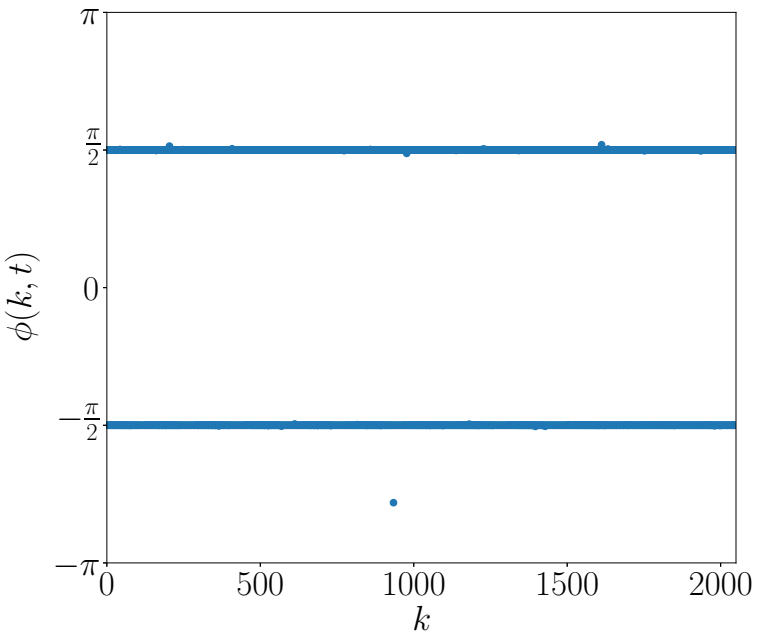

Figure 4.9: Phase as a function of k for $\Gamma_0 = 1$, $t = 1000$

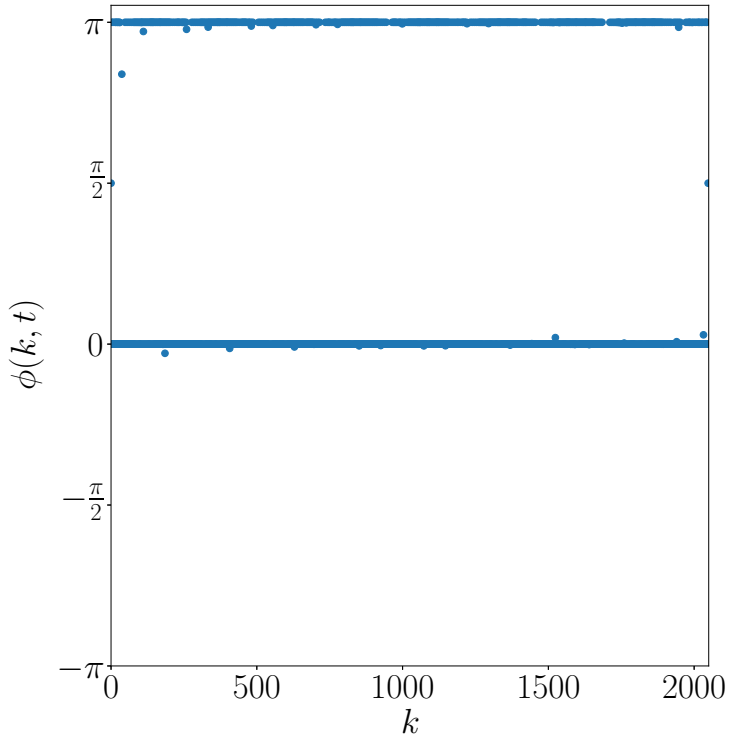

Figure 4.10: Phase as a function of k for $\Gamma_0 = -1$, $t = 1000$

How to delay the shocks formation?

Section 4.1 presented the mapping between the Navier-Stokes equations and the Burgers equation for non-ideal gases, leading to equation:

$$\frac{\partial u_1}{\partial \tau} + \left(\widehat{\Gamma} + \frac{\Lambda_u}{2} u_1\right) u_1 \frac{\partial u_1}{\partial x} = 0. \tag{4.16}$$

It is well known from Thompson [28] that, if $\Gamma = 0$ at every location x and every time t, shock waves do not appear. Indeed, the slope of the characteristics is $\mathrm{d}(u \pm c)$ and–whenever $\Gamma = 0$–this quantity is null. The local variation of velocity is compensated by the local variation of speed of sound meaning that the characteristics never intersect. In practice, it is impossible to obtain such a flow where Γ is zero-valued everywhere and at every time. Even though a zero-valued Γ_0 is imposed at $t = 0$, this parameter will evolve in time leading to the formation of shockwaves. Nonetheless, equation (4.16) suggests that–whenever both Γ_0 and its derivative Λ_0 are null–a shock wave is less likely to appear inside the domain. Analytically, the non-linear term is dropped and equation (4.16) becomes a simple heat equation.[2]
Physically, it is possible to impose a velocity perturbation at a specific thermodynamic point for which $\Gamma = 0$ and $\Lambda_0 = 0$. Indeed, Λ measures the sensitivity of Γ to change along an isentrope. Besides having $\Gamma = 0$–which means no shock waves can form–the flow is less likely to drift away from this condition when Λ_0 is null. The van der Waals gases happen to have a specific point in

[2]We recall that the right-hand side should not be considered zero in practice, for the shock-capturing scheme adds artificial viscosity.

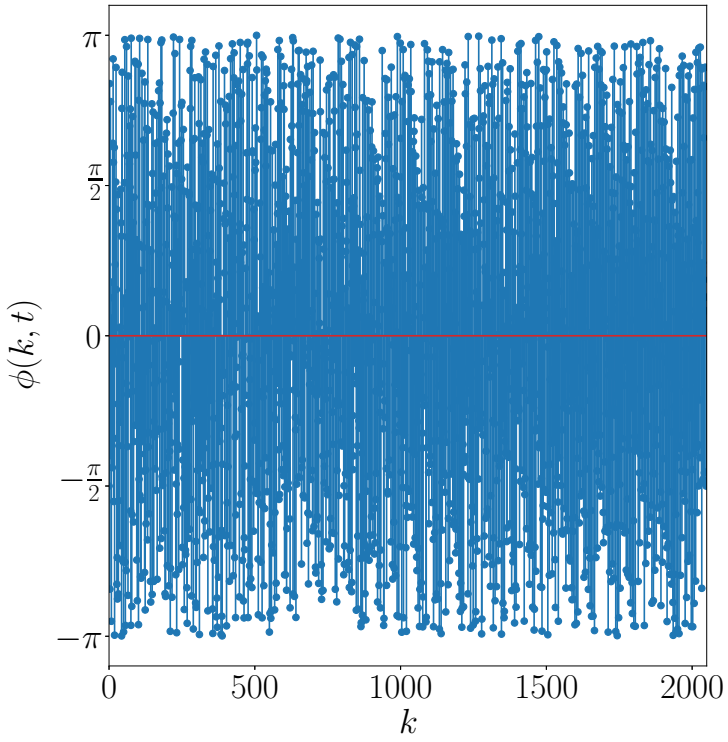

Figure 4.11: Phase as a function of k for $\Gamma_0 = 0$, $t = 1000$

the $p - \vartheta$ diagram for which both Γ and Λ are zero-valued. Indeed, Λ was defined by Kluwick [10], [12], [11] as:

$$\Lambda_0(\widehat{T}, \widehat{\vartheta}) = -\widehat{c}_0(\widehat{T}, \widehat{\vartheta})\widehat{\vartheta}_0 \left(\frac{\partial \Gamma(\widehat{T}, \widehat{\vartheta})}{\partial \widehat{\vartheta}} \right)_{\widehat{s}}. \tag{4.17}$$

In order to compute the derivative of Γ with respect to $\widehat{\vartheta}$ at constant entropy, the temperature can be rewritten as a function of $\widehat{\vartheta}$ and the dimensionless entropy $\widehat{s}$:

$$\widehat{T}(\widehat{s}, \widehat{\vartheta}) = \frac{e^{\delta(\widehat{s}-\widehat{s}_0)}}{(\widehat{\vartheta} - b)^{\delta}}. \tag{4.18}$$

One obtains $\Gamma(\widehat{s}, \widehat{\vartheta})$ by substitution of the expression above into equation (1.32). This allows to derive Γ at constant entropy. Once the expression of $\Lambda(\widehat{s}, \widehat{\vartheta})$ computed, the temperature is

substituted back thus giving $\Lambda(\widehat{T},\widehat{\vartheta})$, whose analytic form is:

$$\Lambda(\widehat{T},\widehat{\vartheta}) = -\widehat{c}(\widehat{T},\widehat{\vartheta})\widehat{\vartheta}^3 \left[\frac{\frac{1}{18}(\delta+1)(\delta+2)\left(\widehat{\vartheta}-\frac{1}{3}\right)^{-3}\left(1-(\delta+3)\frac{\widehat{\vartheta}}{\widehat{\vartheta}-1/3}\right)\widehat{T}+\frac{9}{8\widehat{\vartheta}^4}}{\frac{1}{9}(\delta+1)\left(\widehat{\vartheta}-\frac{1}{3}\right)^{-2}\widehat{T}-\frac{1}{4\widehat{\vartheta}^3}} + \right.$$
$$\left. + \frac{\left(\frac{1}{9}(1+\delta)(2+\delta)\left(\widehat{\vartheta}-\frac{1}{3}\right)^{-3}\widehat{T}-\frac{3}{4\widehat{\vartheta}^4}\right)\left(\frac{1}{18}(1+\delta)(2+\delta)\left(\widehat{\vartheta}-\frac{1}{3}\right)^{-3}\widehat{T}\widehat{\vartheta}-\frac{3}{8\widehat{\vartheta}^3}\right)}{\left(\frac{1}{9}(\delta+1)\left(\widehat{\vartheta}-\frac{1}{3}\right)^{-2}\widehat{T}-\frac{1}{4\widehat{\vartheta}^3}\right)^2} \right] \tag{4.19}$$

where $\widehat{c}(\widehat{T},\widehat{\vartheta})$ is the square root of equation (1.20). Therefore, Λ is null whenever either $\widehat{\vartheta}$, $\widehat{c}(\widehat{T},\widehat{\vartheta})$ or the expression within brackets (from here on referred to as $\sigma(\widehat{T},\widehat{\vartheta})$) are zero-valued. This said, it is impossible to attain $\widehat{\vartheta}=0$; besides, $\widehat{c}(\widehat{T},\widehat{\vartheta})$ is never null except at the critical point if $\delta \to 0$. Nonetheless, the curve $\sigma(\widehat{T},\widehat{\vartheta})=0$ happens to be of great interest, for it reduces Λ to zero.
As mentioned before, we are interested in a point for which both Γ and Λ are null. To this end, it is convenient to consider the restriction of $\sigma(\widehat{T},\widehat{\vartheta})$ along the $\Gamma=0$ line. The root of the resulting function $\sigma(\widehat{\vartheta},\delta)|_{\Gamma=0}$ coincides with the point of interest referred to as point LM. The coordinates of point LM in the $\widehat{p}-\widehat{\vartheta}$ diagram depend on the gas molecular complexity through δ (or N). We recall that, for $\delta = 1/16.66$, there exists a unique point V where $\Gamma = 0$ in the vapour region. When $\delta \to 1/16.66$, point LM converges to point V:

$$\lim_{\delta \to 1/16.66} \left(\widehat{\vartheta},\widehat{p}\right)_{LM} = \left(\widehat{\vartheta},\widehat{p}\right)_{V} \tag{4.20}$$

Furthermore, Kluwick [12] proved that the time of formation of the first shock is:

$$t \propto \frac{1}{\Gamma_0/\varepsilon + \Lambda_0/\widehat{\vartheta}_0(x)} \tag{4.21}$$

where ε is linked to the amplitude of the initial velocity perturbation. Thus, the time of formation of the first shock is maximised for both Λ_0 and Γ_0 zero-valued regardless of the initial perturbation. This result is confirmed by numerical simulations. The LM point shows interesting features and might be exploited for experimental essays aimed at preventing the formation of shock waves inside a non-ideal gas flow.

As far as the numerical simulation is concerned, the very same initial velocity as the previous cases is imposed. The temperature and the specific volume are chosen for Λ_0 and Γ_0 to be zero. For $\delta = 0.001$ (or $\gamma = 1.001$), the LM point is located at[3]:

$$\widehat{\vartheta} = 1.334668,\ \widehat{p} = 1.15547124 \tag{4.22}$$

Figure 4.13 depicts the $x-t$ diagram of velocity for $t \in [0;10]$ and shows a different pattern with respect to the previous simulations: no shock is formed yet.

[3]This values were found numerically as the root of $\sigma(\widehat{\vartheta},\delta)|_{\Gamma=0}$

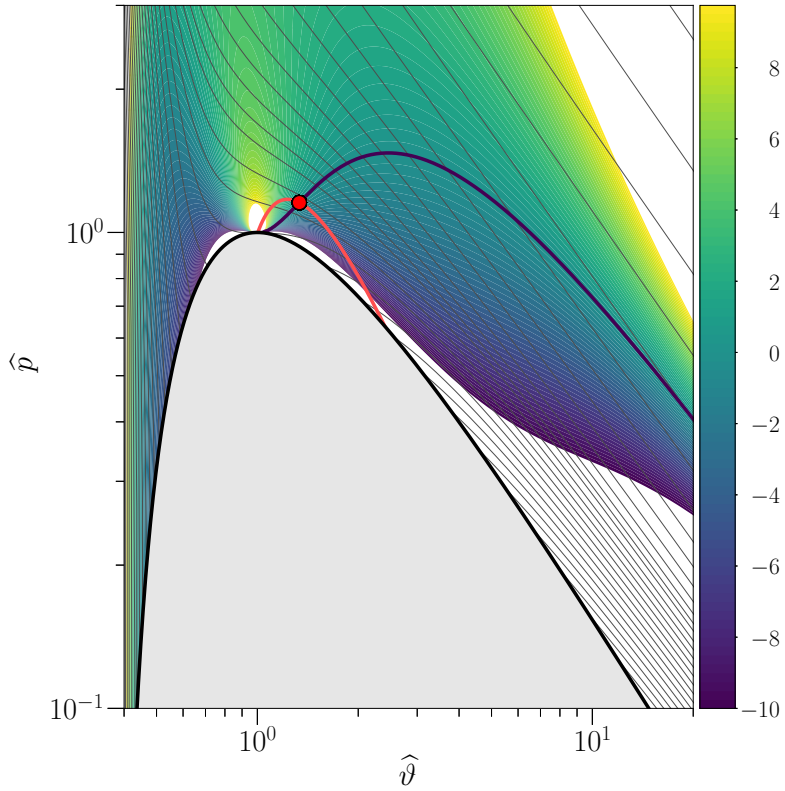

The thick red line is the iso-$\Gamma = 0$, the thick blue line represents the iso-$\Lambda = 0$ curve. At their intersection lies the LM point. The grey lines are the isentropes

Figure 4.12: Λ contour from -10 to $+10$ for $\delta = 0.001$

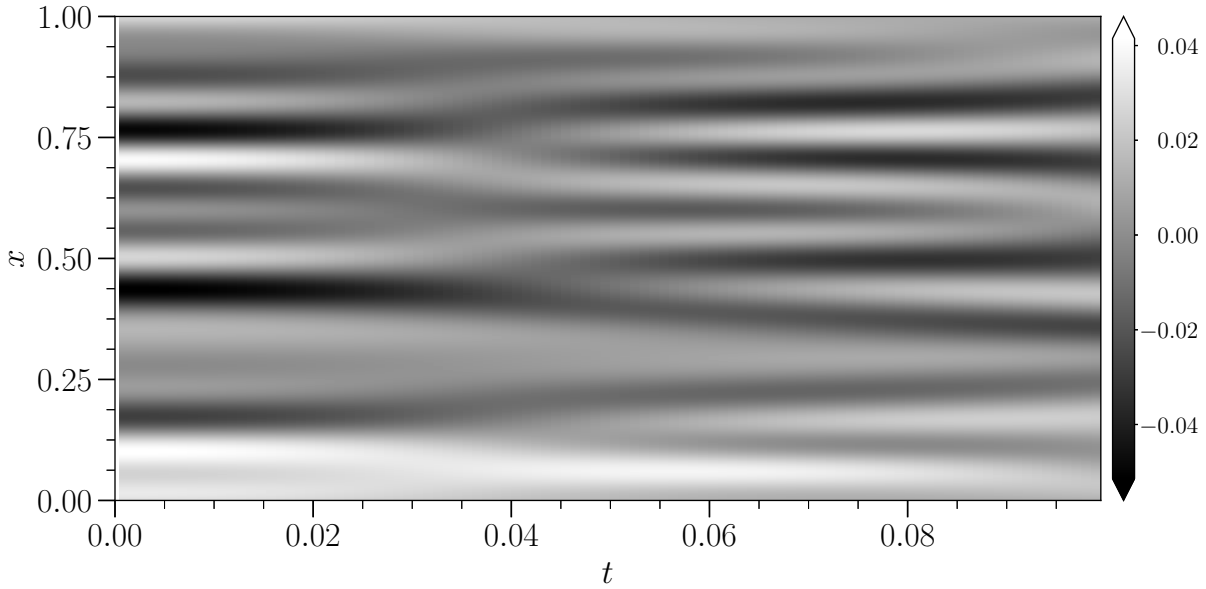

Figure 4.13: $x - t$ diagram for $\Gamma_0 = 0$ and $\Lambda_0 = 0$, the colour scale represents the velocity

The first shock forms at $t_s = 370$ (figure 4.14); the order of magnitude of t_s is twice greater than t_s of the previous simulations. The sudden increase of E_{mean} (figure 4.15) is delayed as

much as possible since a suitable initial thermodynamic state has been chosen. Nevertheless, a shock eventually forms; the reason lies in the higher-order terms that have been discarded when deriving equation (4.16). Indeed, when both Γ_0 and Λ_0 are zero-valued, they lead to the formation of the first shock wave.

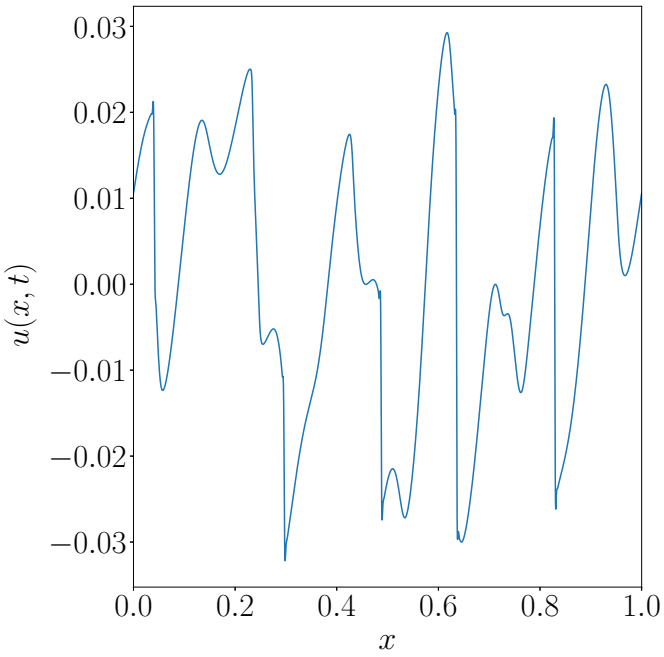

Figure 4.14: Velocity as a function of time at $t = 370$

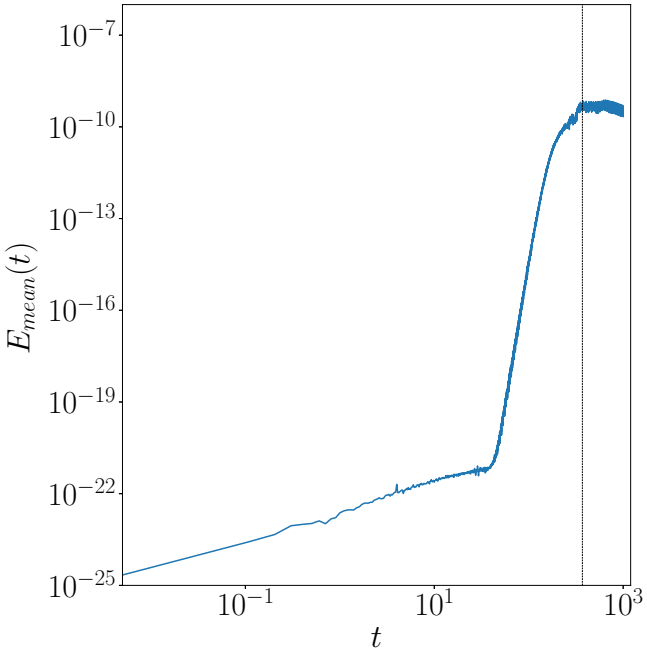

Figure 4.15: Mean spectrum as a function of time

Thermodynamic perturbation

This section–similarly to section 3.3.2–shows how velocity oscillations could be triggered by an initial homoentropic perturbation, despite the initial kinetic energy being set to zero. However–unlike perfect gases–the asymptotic solution will differ in accordance with the initial thermodynamic state, that is to say, depending on the mean value of Γ.
The initial specific volume is a signal of given energy content, namely, a window in Fourier space of constant amplitude 10^{-2} from wave number $k = 1$ to $k = 10$, whose mean value is $\overline{\vartheta}_0 = 1.1$. For the entropy to be constant over the spatial domain, the initial temperature T_0 must vary according to:

$$\widehat{s}(\widehat{T}, \widehat{\vartheta}) = \widehat{s}_0 + \frac{1}{\delta} \ln \widehat{T} + \ln \left(\widehat{\vartheta} - \frac{1}{3} \right) \tag{4.23}$$

and its mean value $\overline{T}_0$ differs between the three cases presented. Consequently, the flow will develop dissimilar non-linear phenomena. Table 4.3 collects all the parameters employed.

Table 4.3: Homoentropic perturbation for a non-ideal gas: parameters employed

	Simulation 2A	*Simulation 2B*	*Simulation 2C*
u_0	0	0	0
$\overline{\vartheta}_0$	1.1	1.1	1.1
$\overline{T}_0$	1.1396	1.0372	1.0189
γ	1.001	1.001	1.001
$\overline{\Gamma}_0$	1	-1	0
N_x	4096	4096	4096
N_t	10^7	10^7	10^7
Δt	10^{-5}	10^{-5}	10^{-5}
t_{final}	1000	1000	1000

Indeed, one can distinguish these three cases by looking at the $p - \vartheta$ diagram (see figure 4.16).

Strong similarities are observed between these three simulations and the simulations of section 4.2.1. In fact, depending on the mean initial value of Γ, the flow will exhibit either positive, negative or mixed non-linearity; notably, the shocks nature changes according to Γ_0. The $x - t$ diagrams depict the time-space evolution of velocity: no substantial differences are observed between the phenomena appearing in figures 4.17, 4.18, 4.19 and those in figures 4.4, 4.5, 4.6 respectively. Thus meaning that, regardless whether a thermodynamic or a velocity perturbation is imposed to the flow, it converges to the same asymptotic solution provided that Γ_0 is the same. Figure 4.20 depicts the three asymptotic solutions at time $t = 1000$.
Once again, the energy spectrum is proportional to k^{-2}, but even more interesting is the time evolution of the mean spectrum as illustrated by figure 4.21. Despite showing the same asymptotic decay, the formation times of the first shock wave (summarised in table 4.4) are quite different with respect to *simulation 1*.

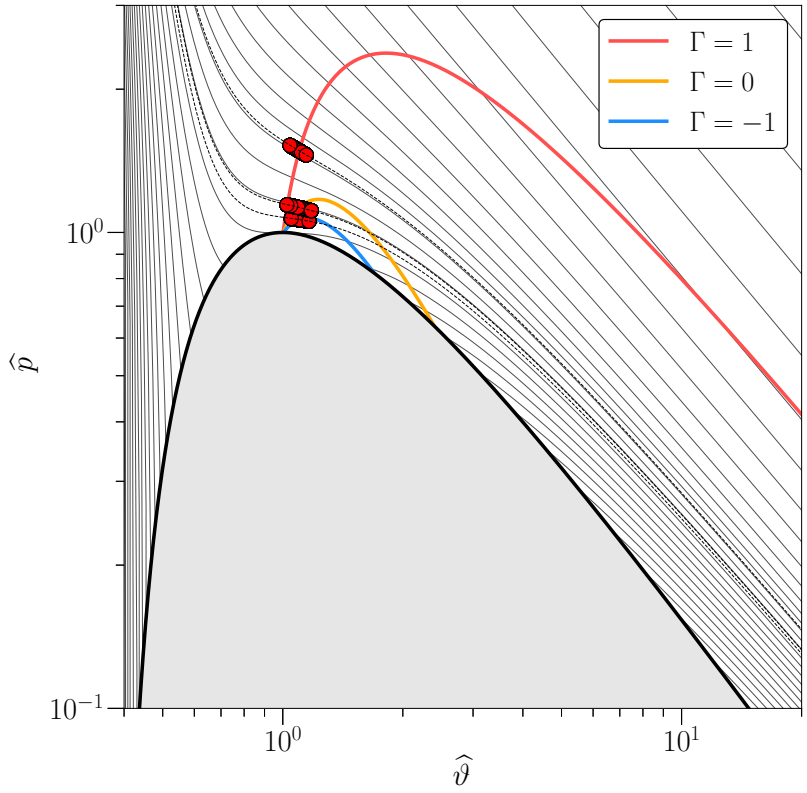

The light grey lines represent the isentropes. The points corresponding to the initial thermodynamic state at each spatial location are plotted on top of grey dashed lines which indicate the three entropy levels.

Figure 4.16: Initial thermodynamic conditions of the three simulations

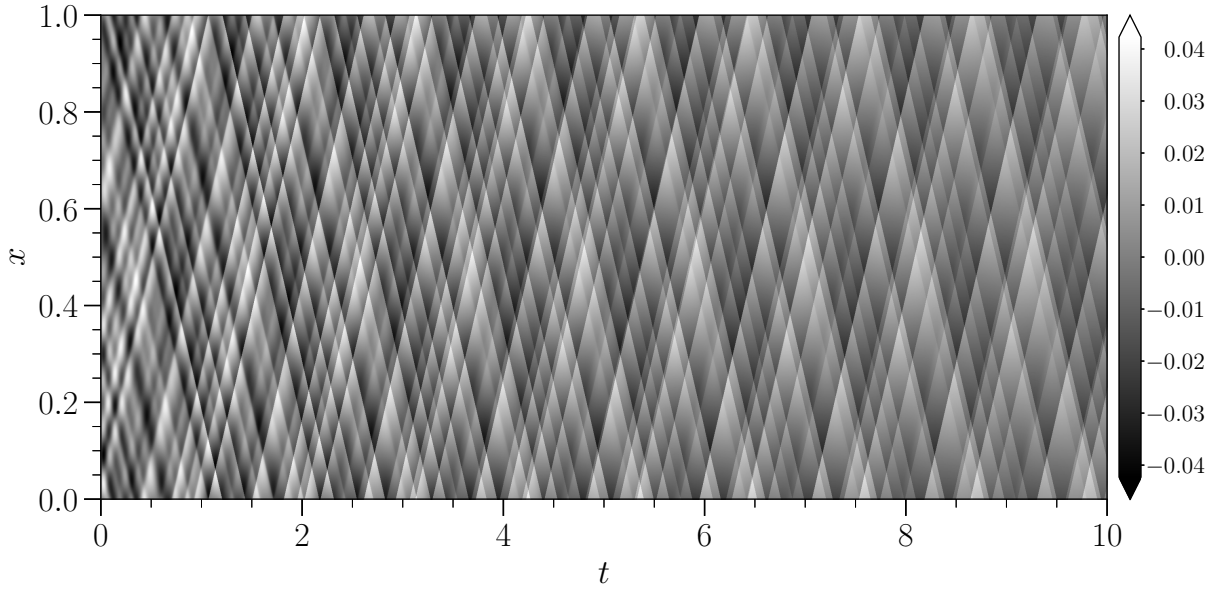

Figure 4.17: *Simulation 2A*: $x - t$ diagram for $\Gamma_0 = 1$, the colour scale represents the velocity

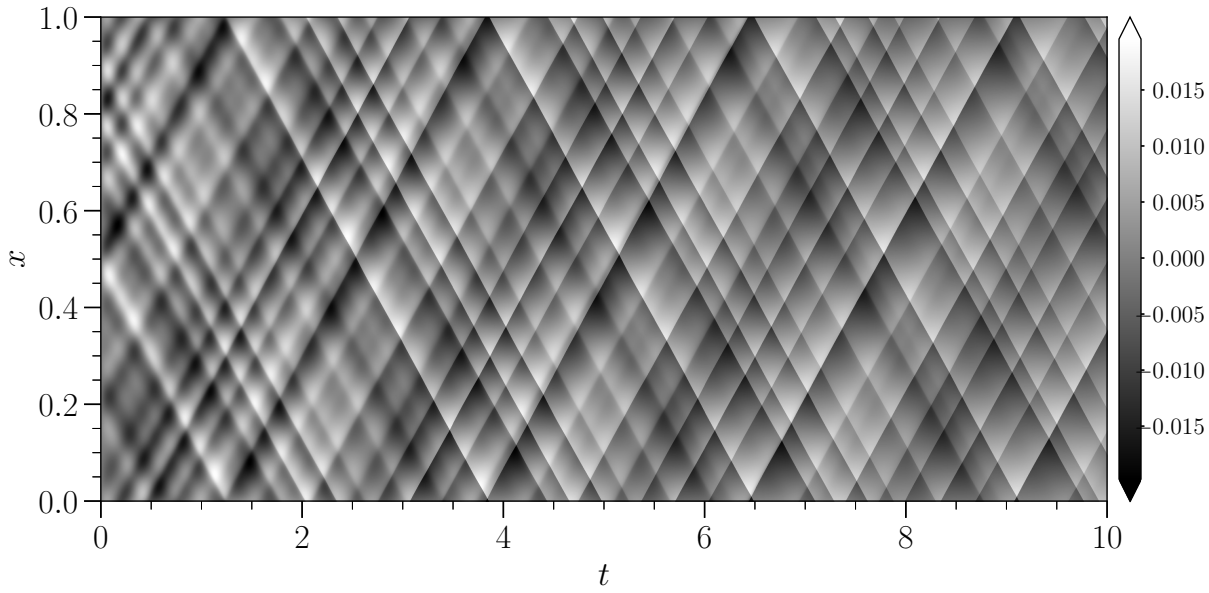

Figure 4.18: *Simulation 2B*: $x - t$ diagram for $\Gamma_0 = -1$, the colour scale represents the velocity

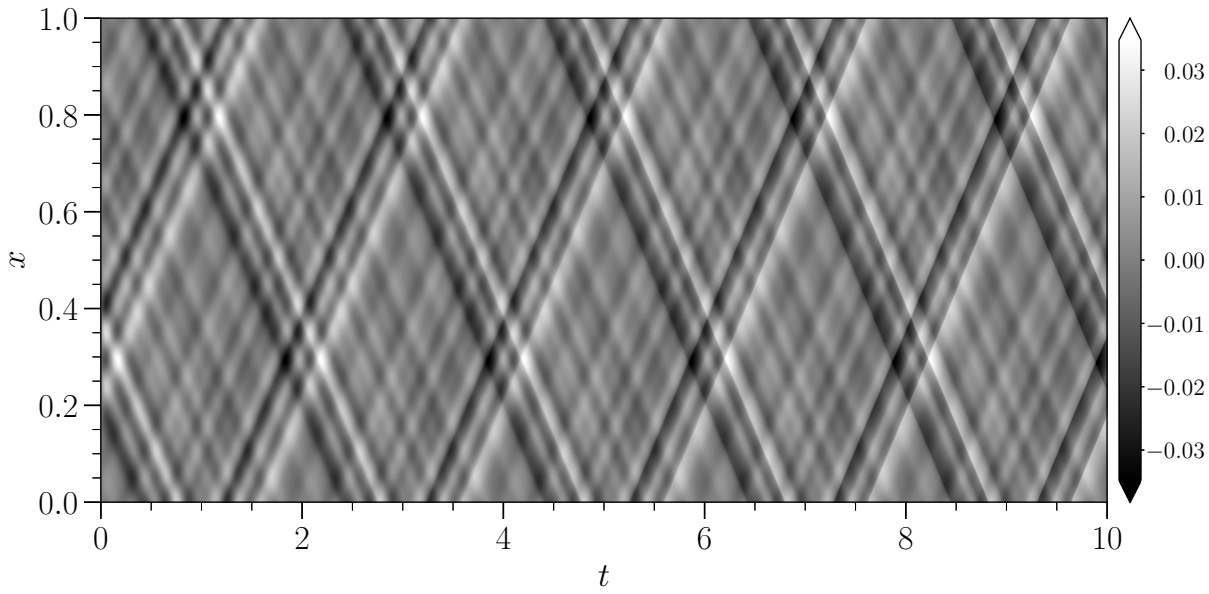

Figure 4.19: *Simulation 2C*: $x - t$ diagram for $\Gamma_0 = 0$, the colour scale represents the velocity

Table 4.4: *Simulation 2*: formation times of the first shock wave

	Simulation 2A	*Simulation 2B*	*Simulation 2C*
Γ_0	1	-1	0
t_s	1.3	3.0	23.5

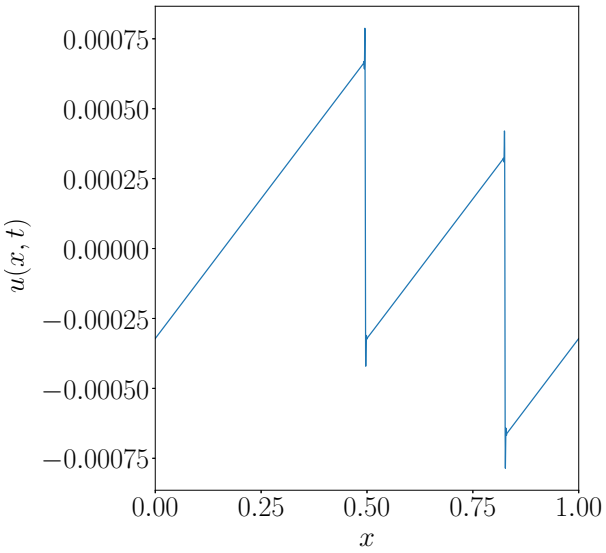

(a) Cross-sectional view of the velocity at $t = 1000$, $\Gamma_0 = 1$

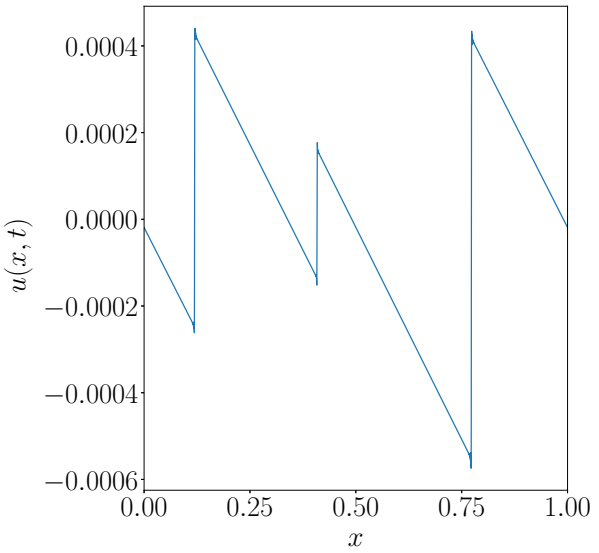

(b) Cross-sectional view of the velocity at $t = 1000$, $\Gamma_0 = -1$

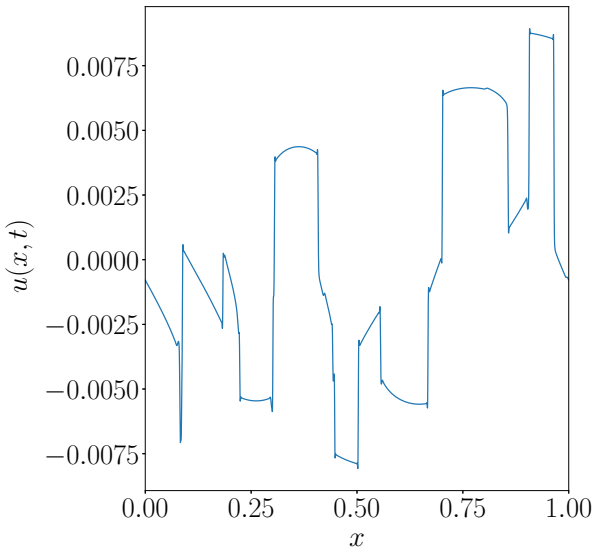

(c) Cross-sectional view of the velocity at $t = 1000$, $\Gamma_0 = 0$

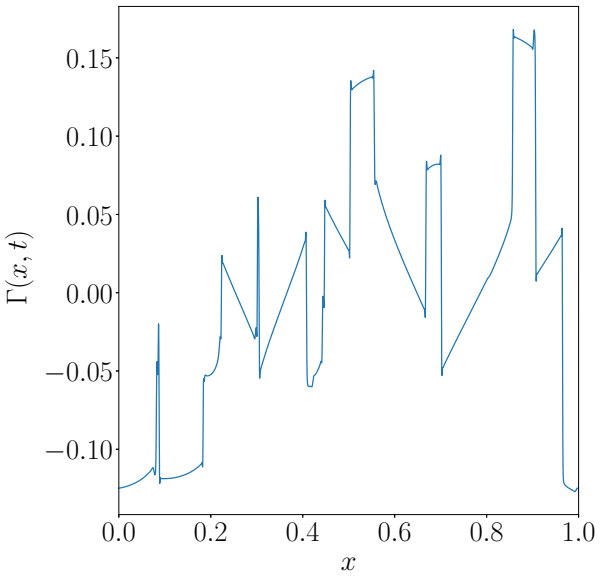

(d) Fundamental derivative at $t = 1000$ for $\Gamma_0 = 0$ as a function of space

Figure 4.20

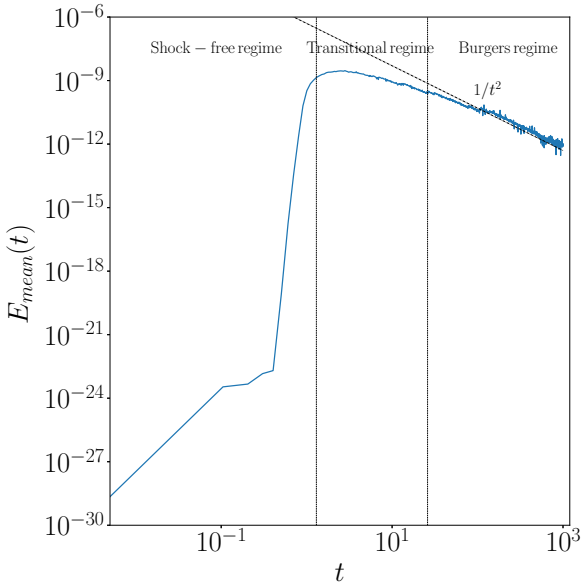

(a) *Simulation 2A*, $\Gamma_0 = 1$

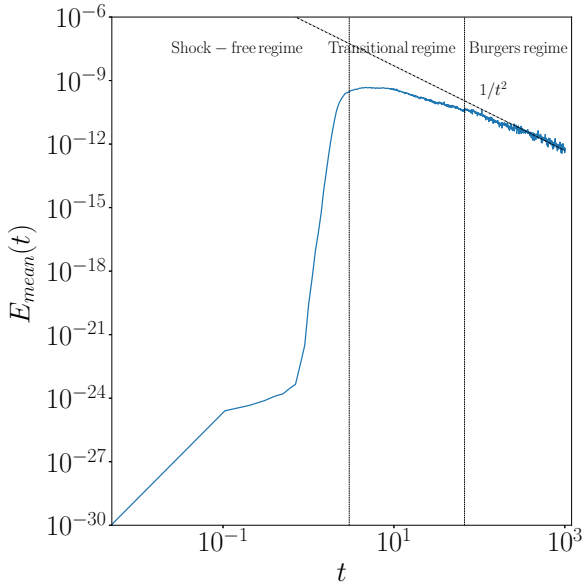

(b) *Simulation 2B*, $\Gamma_0 = -1$

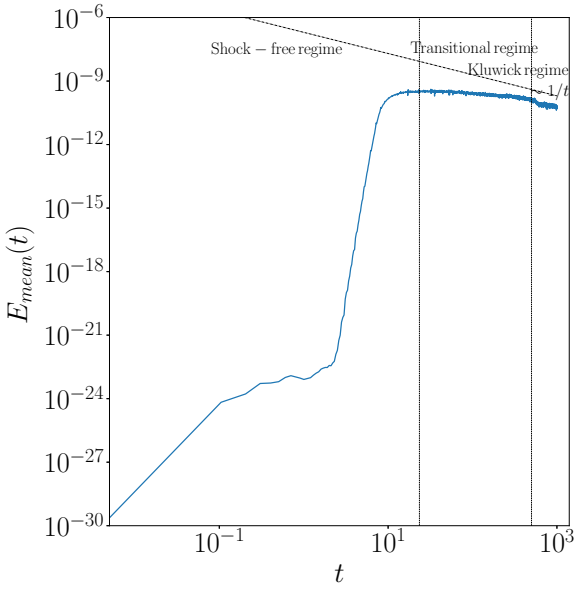

(c) *Simulation 2C*, $\Gamma_0 = 0$

Figure 4.21: *Simulation 2*: time evolution of the mean spectrum $E_{mean}(t)$

4.2.2 Formation time of the first shock wave

Kluwick [12] stated that the formation time of the first shock wave is:

$$t_s = -\frac{1}{\varepsilon^2 \dfrac{\partial \rho_1(x,0)}{\partial x} \left(\Gamma_0/\varepsilon + \Lambda_0 \rho_1(x,0)\right)}. \tag{4.24}$$

It does not uniquely depend on the initial thermodynamic state, but also on the amplitude of the initial perturbation. Table 4.5 collects the first-shock formation times for the six simulations.

Table 4.5: Formation times of the first shock wave

	Simulation 1A	*Simulation 1B*	*Simulation 1C*
Γ_0	1	-1	0
Λ_0	4.79	5.52	6.11
t_s	1.6	1.7	4.2
	Simulation 2A	*Simulation 2B*	*Simulation 2C*
$\overline{\Gamma}_0$	1	-1	0
$\overline{\Lambda}_0$	4.79	5.52	6.11
t_s	1.3	3.0	23.5

Despite equation (4.24) gives an expression of t_s, it is hard to assess its numerical value since ε and $\rho_1(x,t)$ are not explicitly set. Nonetheless, we can comment on its general behaviour. In fact, the Γ_0/ε term is dominant if Γ_0 is different from zero. Consequently, t_s is much lower for *simulations 1A, 1B, 2A* and *2B*. On the contrary, for $\Gamma_0 = 0$, it is the second order term that leads to the formation of the first shock wave. Indeed, t_s is greater if the first-order term is zero-valued.

Moreover, t_s strongly changes whether a velocity or a thermodynamic perturbation is imposed to the flow. Even though for $\Gamma_0 = 1$ the first-shock formation time barely changes, major differences are observed otherwise. The reason lies behind the momentum equation. Let us take *simulations 2A, 2B* and *2C*: figures 4.17, 4.18 and 4.19 clearly show that the initial homoentropic perturbation triggers velocity oscillations of different amplitude. Equation (4.24) states that t_s is greater whether ε is lower, i.e. when the velocity oscillations are more limited. For an inviscid flow, one might rewrite the momentum equation as follows:

$$\frac{D\boldsymbol{u}}{Dt} = -\frac{1}{\rho}\mathbf{grad}(p) \tag{4.25}$$

The variation of $\boldsymbol{u}$ is driven by the pressure gradient, which in turn is related to the speed of sound. The greater the speed of sound, the greater the slope of the isentrope and, consequently, the right-hand-side term of equation (4.25). For instance, let us consider *simulation 2A* and *simulation 2B*. In spite of the same initial density perturbation, the resulting velocity oscillations are lower for *simulation 2B*. This explains why t_s decreases considerably between *simulation 2B* and *simulation 1B*, whose velocity oscillations are in the same range as *simulation 1A* and *simulation 2A*.

4.2.3 Is the non-linear acoustics approximation justified?

Similarly to section 3.3.3, the small perturbation hypothesis is now addressed. Once again, the two-dimensional Fourier transform makes possible verifying whether the aforementioned hypothesis is respected. Let us take *simulation 1A, 1B, 1C* as examples. Figures 4.22, 4.23 and 4.24 respectively show their two-dimensional spectrum. The spectrum component outside the cones differ depending on the initial conditions. Indeed, for $\Gamma_0 = -1$, the shock waves that originate from the initial condition have stronger intensity than for $\Gamma_0 = 1$, the reason being the lower speed of sound. Therefore, the spectrum component outside the cones is greater for *simulation 1B*.

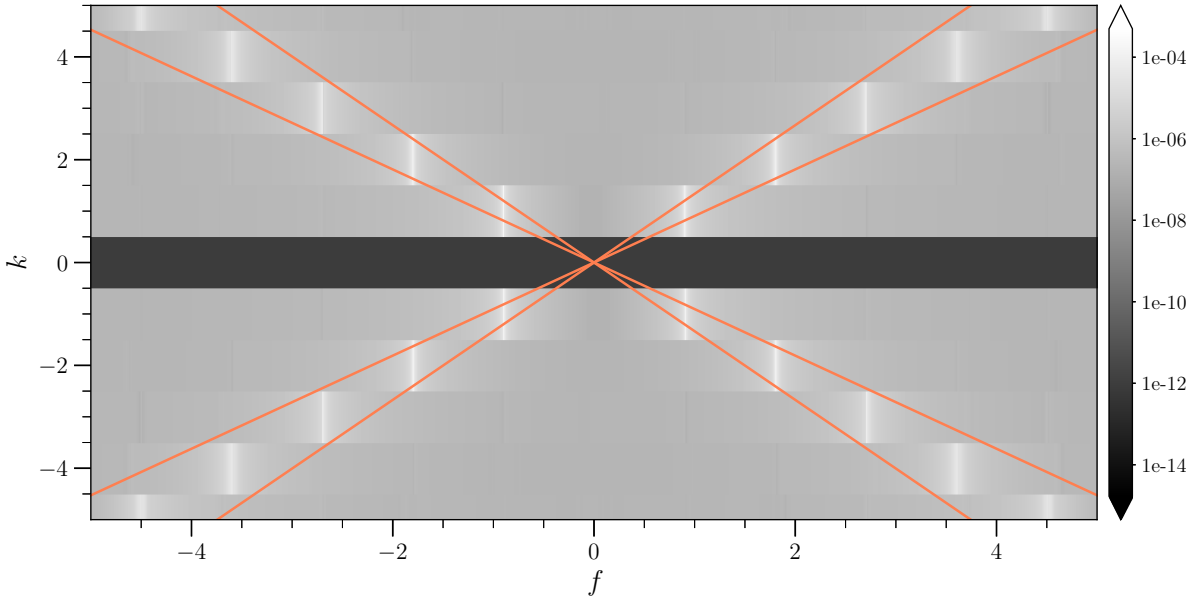

The values of the 2D Fourier transform are represented on a logarithmic scale. The orange lines correspond to the $k = \pm f/c_{min}$ and $k = \pm f/c_{max}$ curves. Pyhton `fft2d` function allocates the mean-value at $k = 0$–which is null for *simulation 1*. This justifies the horizontal black stripe. The k-axis is clipped from -5 to $+5$.

Figure 4.22: *Simulation 1A*: two-dimensional Fourier transform

4.3 From the one-dimensional Navier-Stokes equations to the Burgers equation: viscous numerical simulations

The effect of bulk viscosity is now investigated by using a viscous version of `Compreal`. The same initial condition as *simulation 1B* is imposed. Simulations ran with different values of bulk Reynolds number, namely $Re_b = 6000, 8000, 10000, 20000, 50000, 100000$. The convergence was verified in each case by looking at the energy spectrum as explained in section 3.4.
Firstly, the space-time evolution of the velocity (see figure 4.25) shows how the flow forms once more the typical diamond structures. The sharp edges representing the travelling shock waves are smoother. The dissipative phenomena mostly happen in the shock layer whose thickness increases as μ_b increases.

To better visualise this behaviour, figure 4.26 depicts a cross-view of the $x-t$ diagram at $t = 10$. The solution between two successive discontinuities is not affected by the increasing contribution of the diffusive term, while the shock waves spread out.

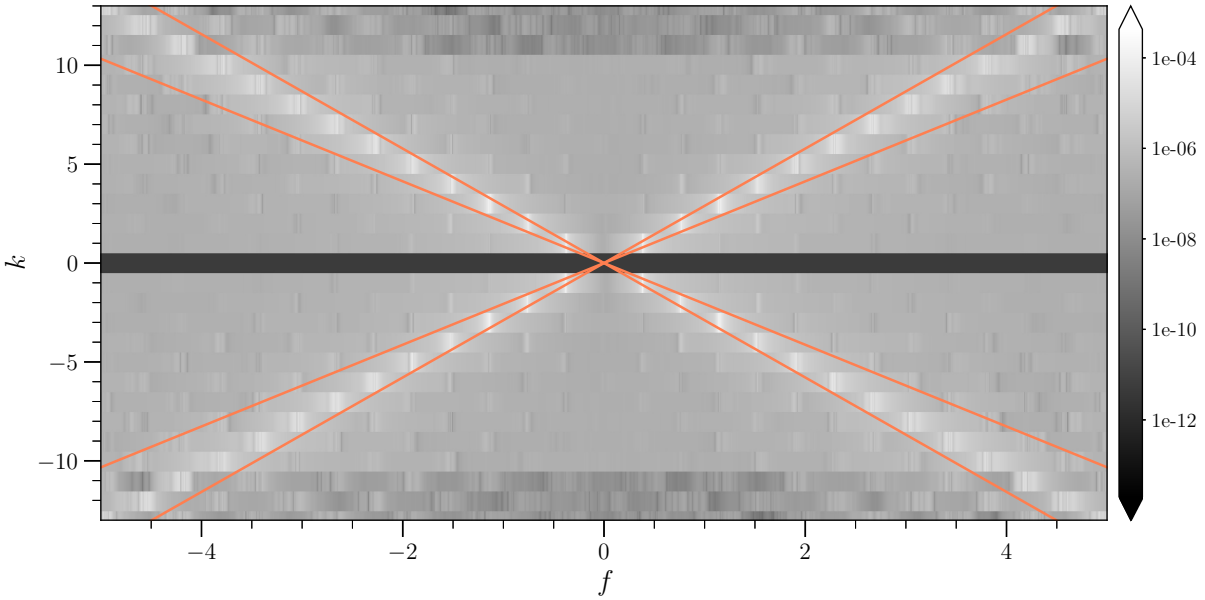

The values of the 2D Fourier transform are represented on a logarithmic scale. The orange lines correspond to the $k = \pm f/c_{min}$ and $k = \pm f/c_{max}$ curves. Pyhton `fft2d` function allocates the mean-value at $k = 0$–which is null for *simulation 1*. This justifies the horizontal black stripe. The k-axis is clipped from -13 to $+13$.

Figure 4.23: *Simulation 1B*: two-dimensional Fourier transform

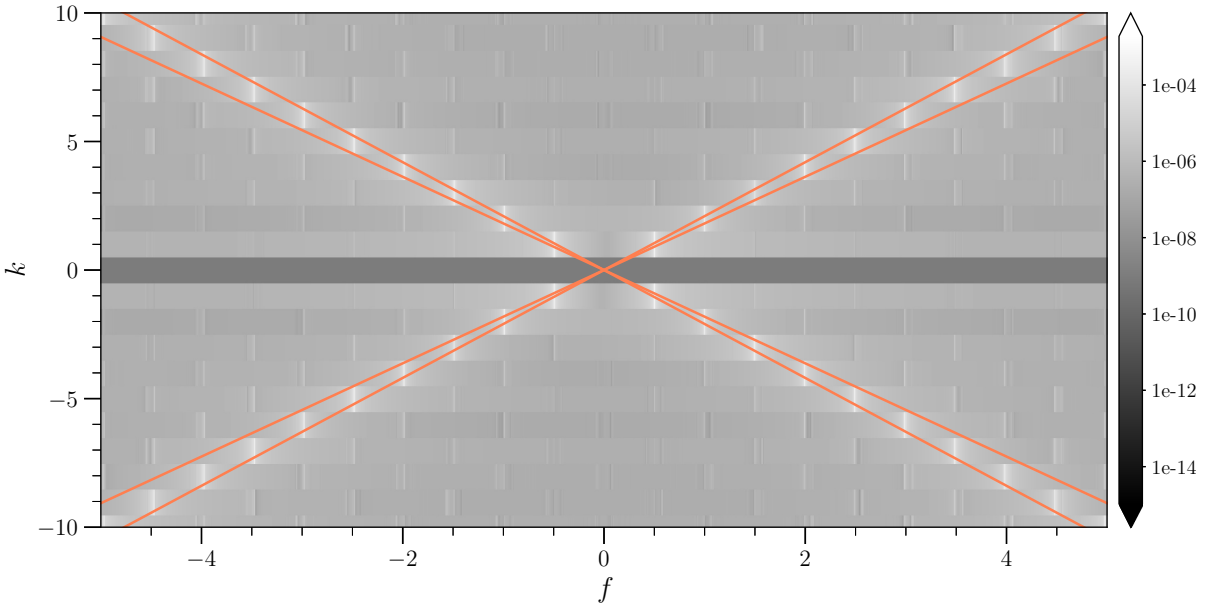

The values of the 2D Fourier transform are represented on a logarithmic scale. The orange lines correspond to the $k = \pm f/c_{min}$ and $k = \pm f/c_{max}$ curves. Pyhton `fft2d` function allocates the mean-value at $k = 0$–which is null for *simulation 1*. This justifies the horizontal black stripe. The k-axis is clipped from -10 to $+10$.

Figure 4.24: *Simulation 1C*: two-dimensional Fourier transform

As far as the energy spectrum $E(k,t)$ is concerned, the effect of viscosity is manifest (see figure 4.27).[4] Higher wave numbers are cut out and the higher the viscosity, the more this effect is intense. There exists a cut-off wave number k_{cut} whose value decreases at higher μ_b. The kinetic energy is dissipated below this critical wave number by the shock waves sweeping the domain,

[4]The energy spectrum has been clipped below 10^{-12}.

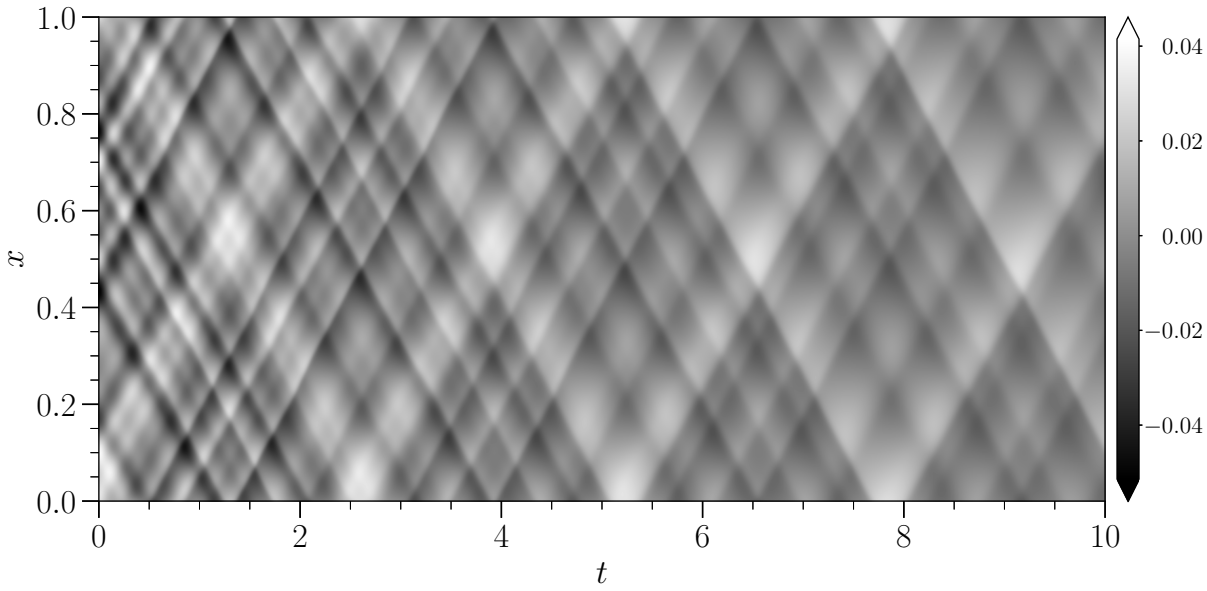

Figure 4.25: *Simulation 1B*: velocity evolution in the $x - t$ diagram for $t \in [0; 10]$ and $Re_b = 6000$

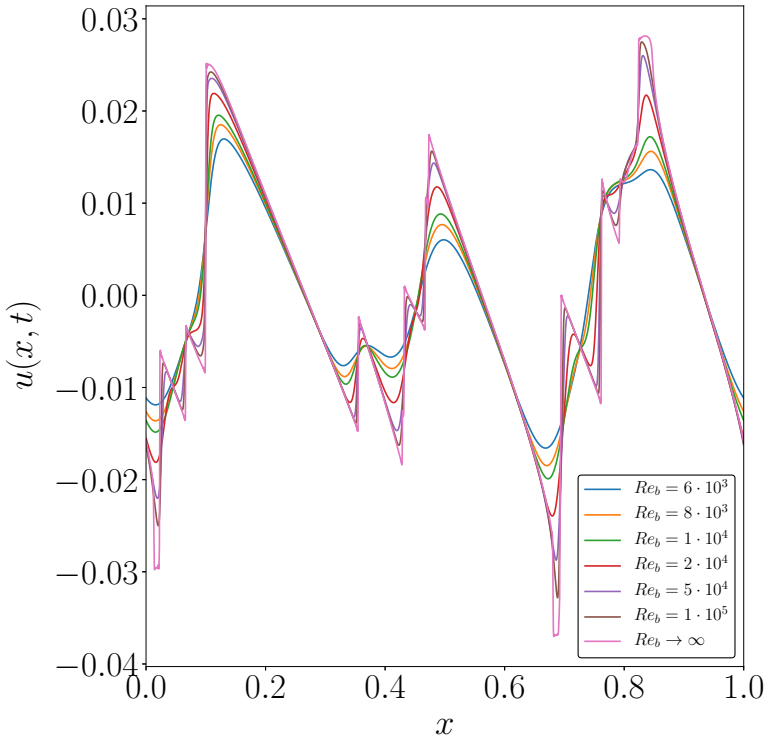

Figure 4.26: *Simulation 1B*: velocity as a function of time at $t = 10$ for different values of Re_b

where diffusive effects are stronger. When the shock wave is more spread out, k_{cut} is smaller and its inverse, the dissipative scale, is greater. Eventually, we can claim that–in one dimension–the dissipative scale is strongly related to the shock waves thickness.

Finally, we can point out that the k^{-2} slope of the inertial spectrum is not preserved in the

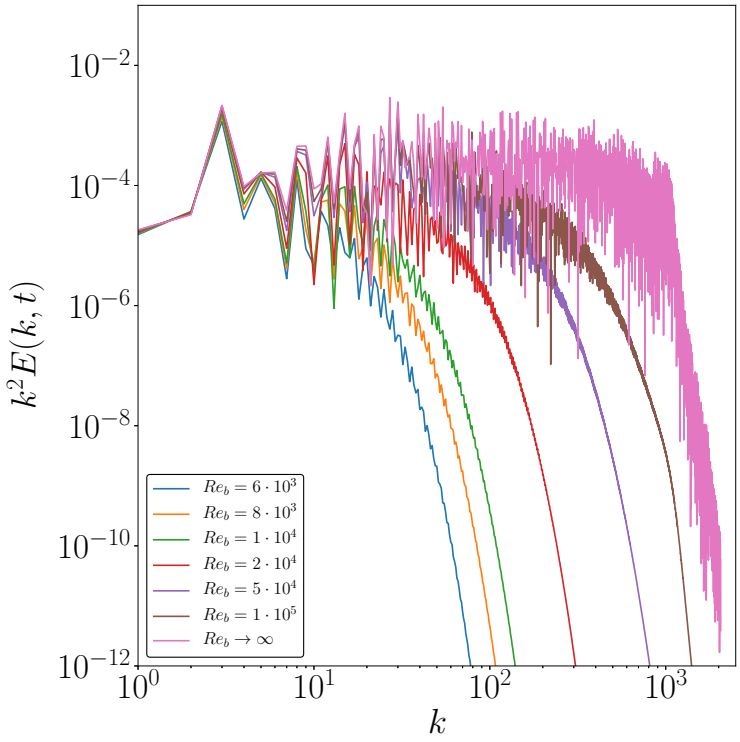

Figure 4.27: *Simulation 1B*: energy spectrum times k^2 at $t = 10$ for different values of Re_b

viscous case. If $\mu_b = \delta$, where δ is a small enough value, the -2 exponent decreases. Chorin [6] proved that the viscosity affects indeed the energy spectrum which no longer is proportional to k^{-2}. Moreover, he provides a correction to the exponent. Nevertheless, it applies to a particular initial condition which has a hyperbolic-tangent shape. In fact, any correction strongly depends on the chosen initial condition and its energy spectrum: it is impossible to retrieve a universal law. This feature has been equally observed for two-dimensional flows by Professor Touber's research team.

As far as the phase is concerned, the bulk viscosity does not have any influence over its spectrum– similarly to the results obtained for the Burgers equation (as shown in section 2.2.3).

Part 5

Energy exchanges in ideal and real gases

This chapter pivots on energy exchanges between internal and kinetic energy. Firstly, the analysis focuses on inviscid flows and a comparison between ideal and non-ideal gases is carried out: it highlights the role that the speed of sound plays on the internal-energy oscillations–typically as their amplitude and frequency are concerned.
Secondly, viscous flows are considered and the role of bulk viscosity is investigated.

5.1 Inviscid flows

To start with, the transport equations of total, kinetic and internal energy for an inviscid flow are recalled (from this point forward all the quantities are dimensionless; for convenience, we let the $\widehat{\bullet}$ notation drop):

$$\frac{\partial(\rho e_t)}{\partial t} + \operatorname{div}\left(\rho e_t \boldsymbol{u}\right) = -\operatorname{div}\left(p\boldsymbol{u}\right), \tag{5.1a}$$

$$\frac{\partial(\rho e_k)}{\partial t} + \operatorname{div}\left(\rho e_k \boldsymbol{u}\right) = -\boldsymbol{u}\cdot\operatorname{div}\left(p\boldsymbol{I}\right), \tag{5.1b}$$

$$\frac{\partial\left(\rho e\right)}{\partial t} + \operatorname{div}\left(\rho e \boldsymbol{u}\right) = -p\operatorname{div}(\boldsymbol{u}) \tag{5.1c}$$

which in one dimension become:

$$\frac{\partial(\rho e_t)}{\partial t} + \frac{\partial}{\partial x}\left(\rho e_t u\right) = -\frac{\partial pu}{\partial x}, \tag{5.2a}$$

$$\frac{\partial(\rho e_k)}{\partial t} + \frac{\partial}{\partial x}\left(\rho e_k u\right) = -u\frac{\partial p}{\partial x}, \tag{5.2b}$$

$$\frac{\partial\left(\rho e\right)}{\partial t} + \frac{\partial}{\partial x}\left(\rho e u\right) = -p\frac{\partial u}{\partial x} \tag{5.2c}$$

the equations above are space-averaged thereafter in order to assess the mean exchanges between kinetic and internal energy. The space average is defined as follows:

$$\langle\bullet\rangle_x = \frac{1}{L}\int_0^L \bullet\,\mathrm{d}x. \tag{5.3}$$

If the operator $\langle \bullet \rangle_x$ is applied to the set of equations (5.2), then one gets:

$$\langle \frac{\partial \left(\rho e_t\right)}{\partial t} \rangle_x + \langle \frac{\partial}{\partial x} \left(\rho e_t u\right) \rangle_x = -\langle \frac{\partial pu}{\partial x} \rangle_x, \tag{5.4a}$$

$$\langle \frac{\partial \left(\rho e_k\right)}{\partial t} \rangle_x + \langle \frac{\partial}{\partial x} \left(\rho e_k u\right) \rangle_x = -\langle u \frac{\partial p}{\partial x} \rangle_x, \tag{5.4b}$$

$$\langle \frac{\partial \left(\rho e\right)}{\partial t} \rangle_x + \langle \frac{\partial}{\partial x} \left(\rho e u\right) \rangle_x = -\langle p \frac{\partial u}{\partial x} \rangle_x. \tag{5.4c}$$

As mentioned in section 3.2.1, periodic boundary conditions were imposed, hence the divergence terms can be discarded. In fact, let us take the total energy as a matter of example:

$$\langle \frac{\partial}{\partial x} \left(\rho e_t u\right) \rangle_x = \frac{1}{L} \int_0^L \frac{\partial}{\partial x} \left(\rho e_t u\right) \mathrm{d}x = \rho(L,t) e_t(L,t) u(L,t) - \rho(0,t) e_t(0,t) u(0,t). \tag{5.5}$$

Because of the periodic boundary conditions, $\rho e_t u$ at $x = 0$ and $x = L$ cancel out at every t, thus:

$$\langle \frac{\partial}{\partial x} \left(\rho e_t u\right) \rangle_x = 0. \tag{5.6}$$

The same applies to the right-hand-side term of equation (5.4a). Eventually, one obtains:

$$\frac{\partial \langle \rho e_t \rangle_x}{\partial t} = 0, \tag{5.7a}$$

$$\frac{\partial \langle \rho e_k \rangle}{\partial t} = -\langle u \frac{\partial p}{\partial x} \rangle_x, \tag{5.7b}$$

$$\frac{\partial \langle \rho e \rangle_x}{\partial t} = -\langle p \frac{\partial u}{\partial x} \rangle_x \tag{5.7c}$$

where:

$$\langle \frac{\partial \bullet}{\partial t} \rangle_x = \frac{\partial \langle \bullet \rangle_x}{\partial x} \tag{5.8}$$

since L is time independent. One can easily infer that the mean total energy $\langle \rho e_t \rangle_x$ is constant in time. Indeed, the sum of internal and kinetic energy has to be conserved.

Let us consider *simulation 1* of chapter 3–the gas being ideal. The energy balances described by the set of equations (5.7) can be easily verified. From the output provided by `Compreal`, the time derivatives are computed with a first-order-accuracy forward-finite-difference scheme:

$$\frac{\partial f(x,t_i)}{\partial t} \simeq \frac{f(x,t_{i+1}) - f(x,t_i)}{\Delta t} \tag{5.9}$$

whereas the space derivatives are computed with a first-order-accuracy centered-finite-difference scheme:

$$\frac{\partial f(x_i,t)}{\partial x} \simeq \frac{f(x_{i+1},t) - 2f(x,t_i) + f(x_{i-1},t)}{\Delta x^2}. \tag{5.10}$$

Figure 5.1 depicts the mean-internal-energy balance and figure 5.2 the mean-kinetic-energy balance. The error between the energy time evolution and the forcing term at the right-hand side is minor: it is due to the artificial viscous term that should be added to the forcing term to balance out the left-hand side. Nonetheless, the shocks appearing in this specific case are weak, hence, the contribution of the artificial viscous term is negligible.

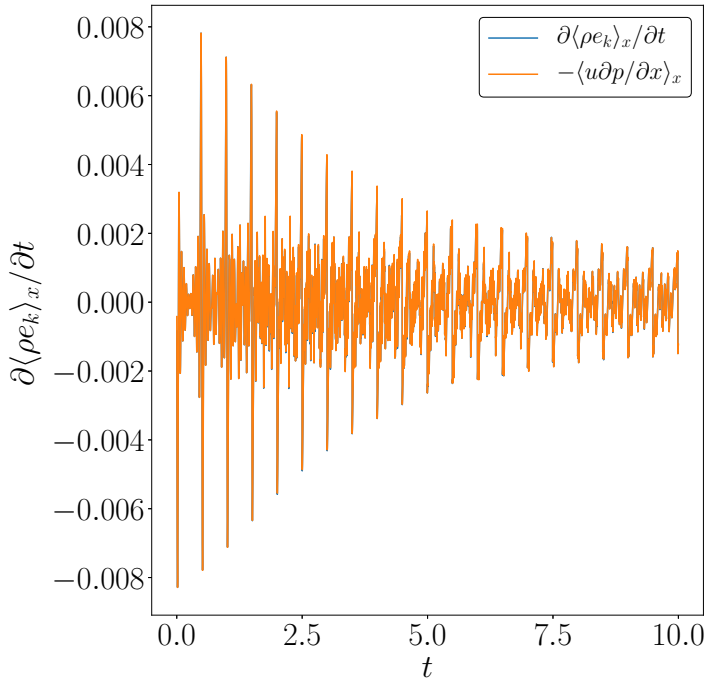

Figure 5.1: Mean-kinetic-energy balance for an ideal gas, $t \in [0; 10]$

Once the energy balances verified, the exchanges between internal and kinetic energy can be finally assessed. To this end, we define $\overline{E}_t(t)$, $\overline{E}_k(t)$ and $\overline{E}(t)$ as follows:

$$\overline{E}_t(t) = \langle \rho e_t \rangle_x, \tag{5.11a}$$

$$\overline{E}_k(t) = \langle \rho e_k \rangle_x, \tag{5.11b}$$

$$\overline{E}(t) = \langle \rho e \rangle_x \tag{5.11c}$$

and plot $\overline{E}(t)$ as a function of $\overline{E}_k(t)$. Every point of coordinates $(\overline{E}_k(t); \overline{E}(t))$ corresponds to a given time. In chapters 3 and 4, two classes of initial conditions were addressed: a velocity perturbation and a thermodynamic perturbation. The former is equivalent to a kinetic energy perturbation (see *simulation 1* of chapter 3), the latter to an internal energy perturbation (see *simulation 2* of chapter 3).

Figure 5.3 shows the aforementioned evolution of $\overline{E}(t)$ as a function of $\overline{E}_k(t)$ for *simulation 1*.

The slope of the curve depicted in figure 5.3 is easily found to be -1 since the mean total energy is conserved and:

$$\overline{E}_t(t) = \overline{E}_k(t) + \overline{E}(t) \rightarrow \overline{E}(t) = \overline{E}_t(t) - \overline{E}_k(t) \tag{5.12}$$

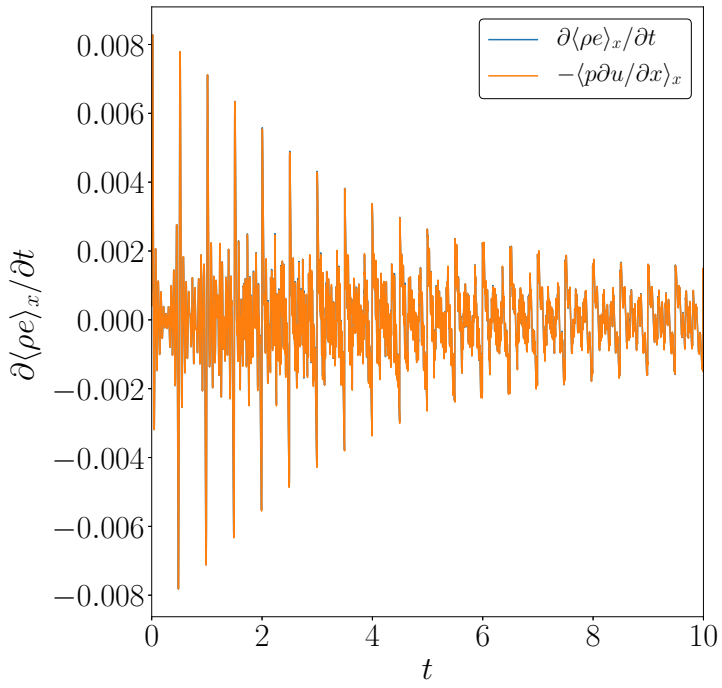

Figure 5.2: Mean-internal-energy balance for an ideal gas, $t \in [0; 10]$

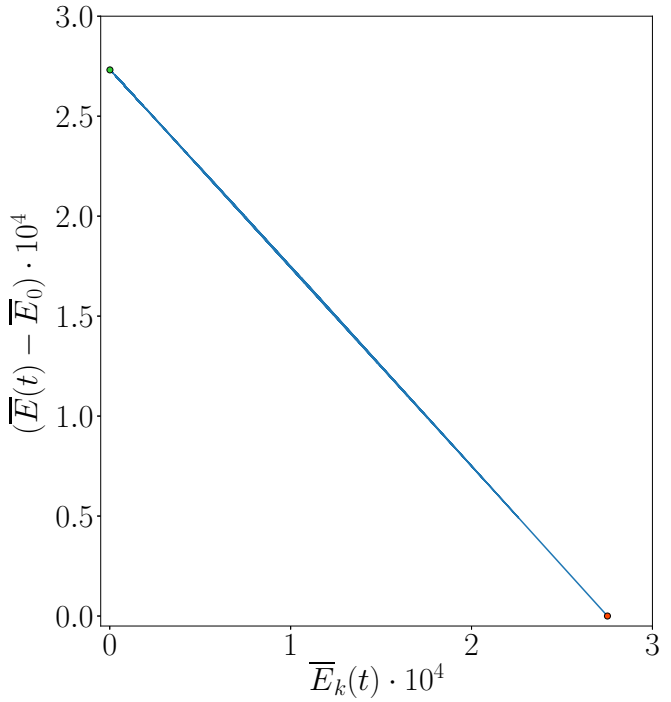

The starting point is pictured in red, the ending point in green. For the sake of better understanding, both the x and y-axes have been magnified by a 10^4 factor.

Figure 5.3: Velocity perturbation for an ideal gas: mean internal energy vs. mean kinetic energy, $t \in [0; 1000]$

In addition, from a theoretical stand point, the mean total energy is not function of time as its time derivative is zero (see equation (5.7a)).
Nonetheless–as explained in chapter 3.2.1–a filter is applied. Its aim being to drain energy at small scale, it hence introduces dissipation. This reflects on the total energy which slightly decreases in time. Even though it is hardly visible from figure 5.3, the curve slightly drifts to lower levels of $\overline{E}_t$ as time passes. To better visualise the effect of applying a numerical filter, figure 5.4 shows the time evolution of $\overline{E}_t(t)$.

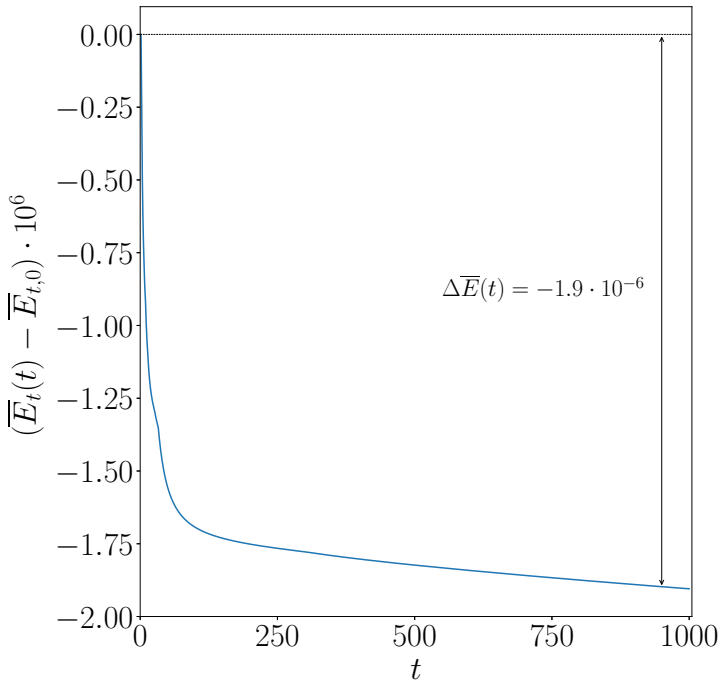

Figure 5.4: Velocity perturbation for an ideal gas: mean total energy as a function of time

This said, let us shift focus back to the mean-kinetic-energy and mean-internal-energy oscillations. Figures 5.5 and 5.6 reproduce their allure in time: the mean kinetic energy decreases in time, while the mean internal energy increases. This behaviour was largely expected, however, one might investigate more thoroughly these oscillations and associate their behaviour to the velocity space-time evolution.

Indeed, both the mean kinetic and mean internal energy oscillate much. By zooming in on a shorter time interval, this characteristic is manifest: the mean kinetic energy has local minima and maxima due to shock waves interaction. Notably, whenever the two biggest shock waves interact, $\overline{E}_k(t)$ ramps up showing a local maximum (see figures 5.7 and 5.8). Furthermore, the shock waves velocity strongly relates to the speed of sound. Because the strong assumption of small perturbations has been considered throughout this work, the non-linear-acoustic framework fits perfectly (see Crigthon [7] and Kluwick [10], [11], [12]): weak shock waves sweep the domain and can be modelled as acoustic waves. That is why the distance between two successive local maxima in figure 5.7 is almost constant and equal to:

$$\Delta t = \frac{L/2}{c_0} \tag{5.13}$$

where the $1/2$ coefficient that multiplies L is due to the fact that acoustic waves can travel

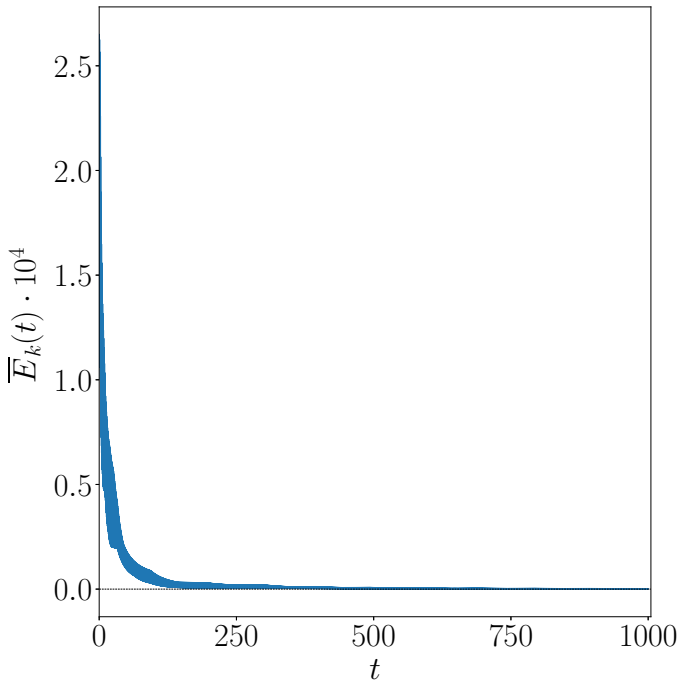

Figure 5.5: Velocity perturbation for an ideal gas: mean kinetic energy as a function of time

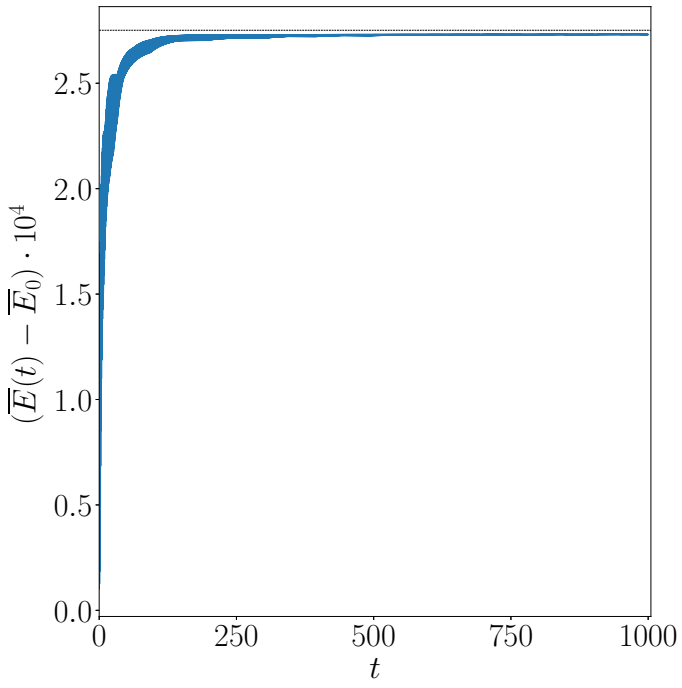

Figure 5.6: Velocity perturbation for an ideal gas: mean internal energy as a function of time

rightwards or leftwards. Consequently, as c_0 decreases, shock waves interact at lower frequency: the resulting diamond structures in the $x-t$ diagram will spread out. Eventually, the amplitude of the $\overline{E}_k(t)$ oscillations lessens over time as the shock waves intensity lowers (see section 3.3.1).

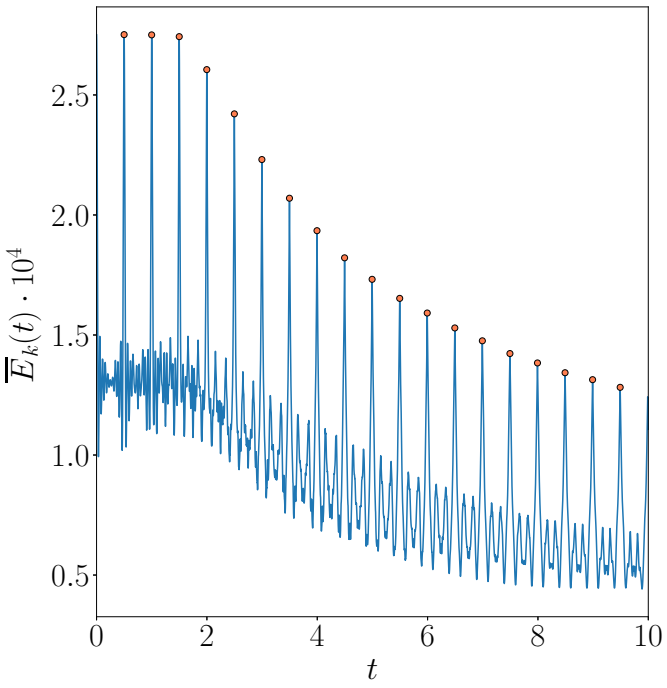

The orange points highlight local mean-kinetic-energy maxima.

Figure 5.7: Velocity perturbation for an ideal gas: mean kinetic energy as a function of time, $t \in [0; 10]$

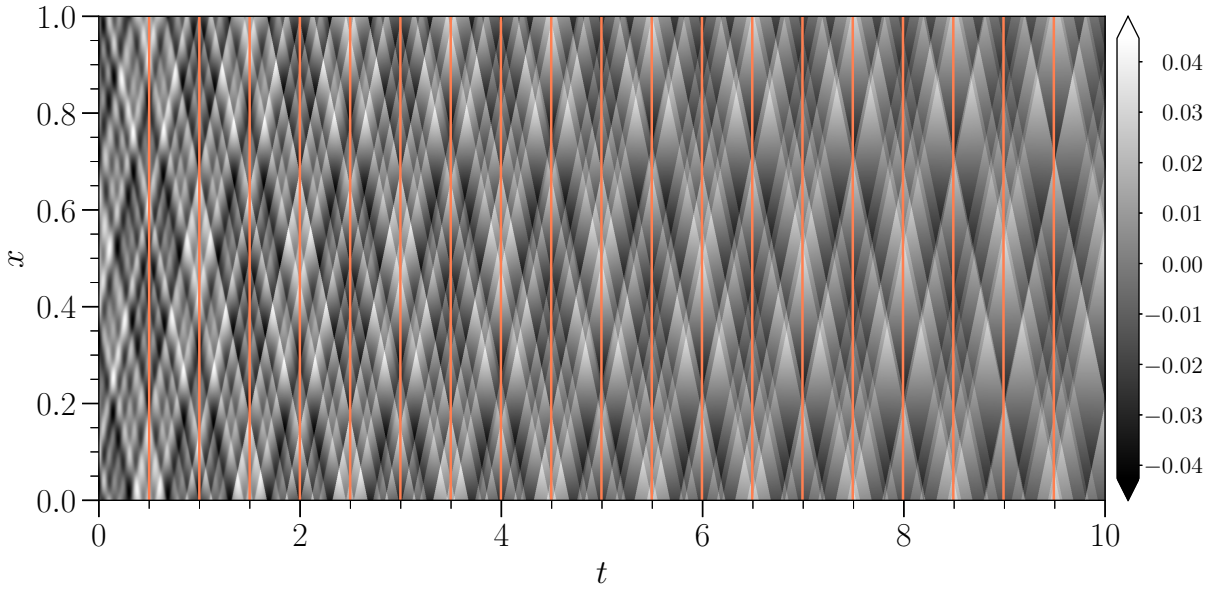

The orange vertical lines correspond to local mean-kinetic-energy maxima.

Figure 5.8: Velocity perturbation for an ideal gas: $x - t$ diagram of velocity, $t \in [0; 10]$

Let us consider *simulation 2* of chapter 3 where a thermodynamic perturbation was injected at $t = 0$. The most valuable information concerns the energy path: in spite of a zero $\overline{E}_{k,0}$, the internal energy perturbation rapidly triggers kinetic energy oscillations. Theoretically, the

reason is rather straightforward and lies behind the momentum equation. In fact, it states:

$$\frac{D\boldsymbol{u}}{Dt} = -\frac{1}{\rho}\mathbf{grad}(p) \tag{5.14}$$

therefore, the right-hand side drives the velocity oscillations and explains the creation of kinetic energy. $\overline{E}_k(t)$ attains a maximum shortly thereafter before decreasing in time. The energy path depicted in figure 5.9 summarises this process. Once more, the filter dissipates a small amount of total energy (as shown in figure 5.10) thus the curve drifts downwards to lower-energy levels. Nonetheless, let us assume that no total energy dissipation happens, we do not expect the point at $t = \infty$ to coincide with the initial point. In fact, shock waves appear inside the domain and these irreversible phenomena lead to an asymptotic condition that does not match the initial.

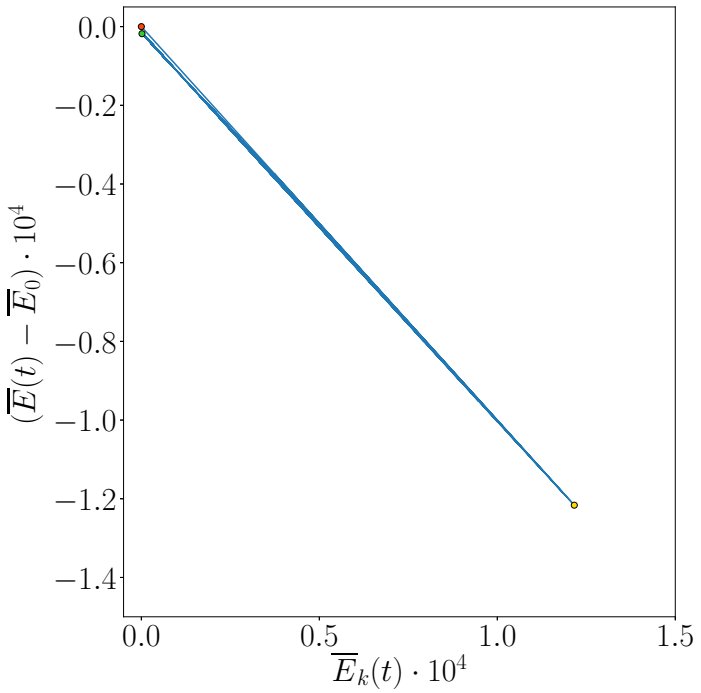

The starting point is pictured in red, the ending point in green. $\overline{E}_k(t)$ attains a maximum whose value is marked by a yellow point. For the sake of better understanding, both the x and y-axes have been magnified by a 10^4 factor.

Figure 5.9: Thermodynamic perturbation for an ideal gas: mean internal energy vs. mean kinetic energy, $t \in [0; 1000]$

Similar behaviours are observed for non-ideal gases–namely for *simulations 1A, 1B, 1C* and *simulations 2A, 2B, 2C* of chapter 4.

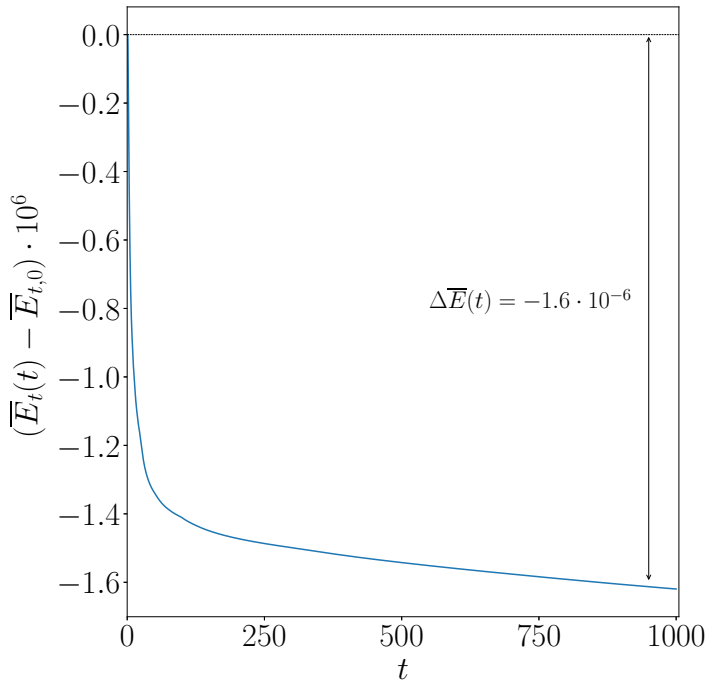

Figure 5.10: Thermodynamic perturbation for an ideal gas: mean total energy as a function of time

5.2 Comparison of ideal and non-ideal gases behaviours

Firstly, let us take the system of equations (1.15):

$$\begin{cases} \dfrac{\partial \rho}{\partial t} + \operatorname{div}(\rho \boldsymbol{u}) = 0 \\ \dfrac{\partial \rho \boldsymbol{u}}{\partial t} + \operatorname{div}(\rho \boldsymbol{u} \otimes \boldsymbol{u} + p\boldsymbol{I}) = 0 \\ \dfrac{\partial \rho e}{\partial t} + \operatorname{div}(\rho e \boldsymbol{u}) = -p \operatorname{div}(\boldsymbol{u}) \end{cases} \tag{5.15}$$

System (5.15) can be recast more conveniently as follows:

$$\begin{cases} \dfrac{Dv}{Dt} = \vartheta \operatorname{div}(\boldsymbol{u}) \\ \dfrac{D\boldsymbol{u}}{Dt} = -\vartheta \, \mathbf{grad}(p) \\ \dfrac{De}{Dt} = -p \dfrac{D\vartheta}{Dt} \end{cases} \tag{5.16}$$

or, in one dimension:

$$\begin{cases} \dfrac{D\vartheta}{Dt} = \vartheta \dfrac{\partial u}{\partial x} \\ \dfrac{Du}{Dt} = -\vartheta \dfrac{\partial p}{\partial x} \\ \dfrac{De}{Dt} = -p\dfrac{D\vartheta}{Dt} \end{cases} \tag{5.17}$$

where the third equation is nothing but the first principle of thermodynamics in the absence of heat exchange.

To effectively compare ideal and non-ideal gases, a specific input has been designed. Given the same initial state in the $\widehat{p} - \widehat{\vartheta}$ diagram, we impose the same $\partial u/\partial x$ and, consequently, the same $\Delta\vartheta$, for the first equation of system (5.17) prescribes the equivalence between $D\vartheta/Dt$ and the derivative of velocity with respect to space. The slope of the isentrope being different, the internal-energy oscillations triggered by the input will depend on the gas nature.
Moreover, not only the same velocity signal is imposed–be the gas ideal or non-ideal–, but also the frequency content of $\partial u/\partial x$ is constant from $k = 1$ to $k = 1000$. To do so, the amplitude spectrum of $u_0(t)$ is:

$$|\mathcal{F}(u_0(t))| = k^{-1} \quad \text{for } k \in [1; 1000] \tag{5.18}$$

Figure 5.11 shows $u_0(x)$ as a function of x, whereas figures 5.12a and 5.12b give the spectra of $u_0(x)$ and $\partial u_0(x)/\partial x$ spectrum. The amplitude of $u_0(x)$ is greater with respect to the simulations of the previous chapters; we expect the resulting shock waves not to propagate at the speed of sound. For the initial condition to be fully described, figure 5.13 shows the initial state on the $\widehat{p} - \widehat{\vartheta}$ diagram.
At $t = \Delta t$, the thermodynamic states align with one of the two isentropes that cross point $(\widehat{\vartheta}_0, \widehat{p}_0)$, depending on the equation of state of the gas. As expected, $\Delta\vartheta$ is equal for the two cases (see figure 5.14). On the other hand, Δp is greater for the perfect-gas case since the initial speed of sound is greater and thus the isentrope slope. Table 5.1 summarises the parameters of the two simulations.

Table 5.1: Comparison of ideal and real gas

	Ideal gas	Non-ideal gas
u_0	perturbation	perturbation
ϑ_0	1.1	1.1
p_0	1.4846	1.4846
γ	1.001	1.001
c_0	0.899	1.279
Γ_0	/	1
N_x	4096	4096
N_t	10^6	10^6
Δt	10^{-5}	10^{-5}
t_{final}	10	10

The results from `Compreal` allow us to compare an ideal gas to a non-ideal gas. First of all,

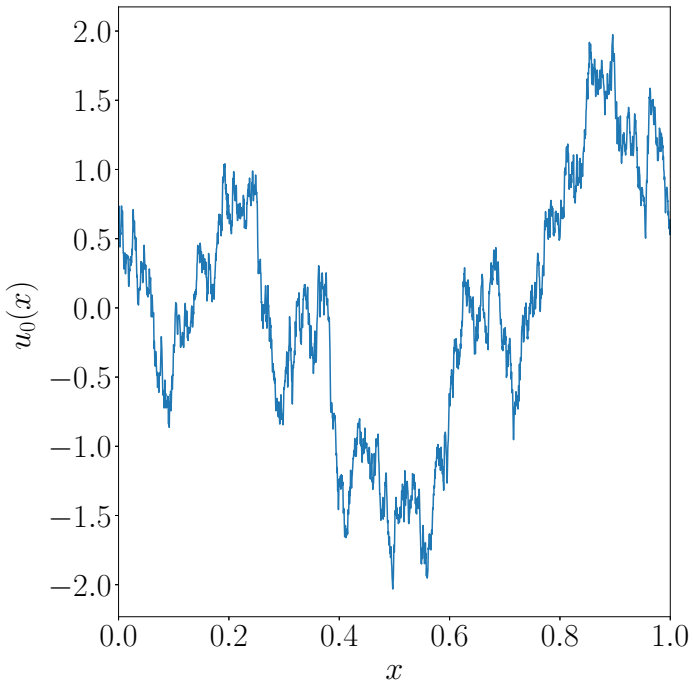

Figure 5.11: Initial velocity signal

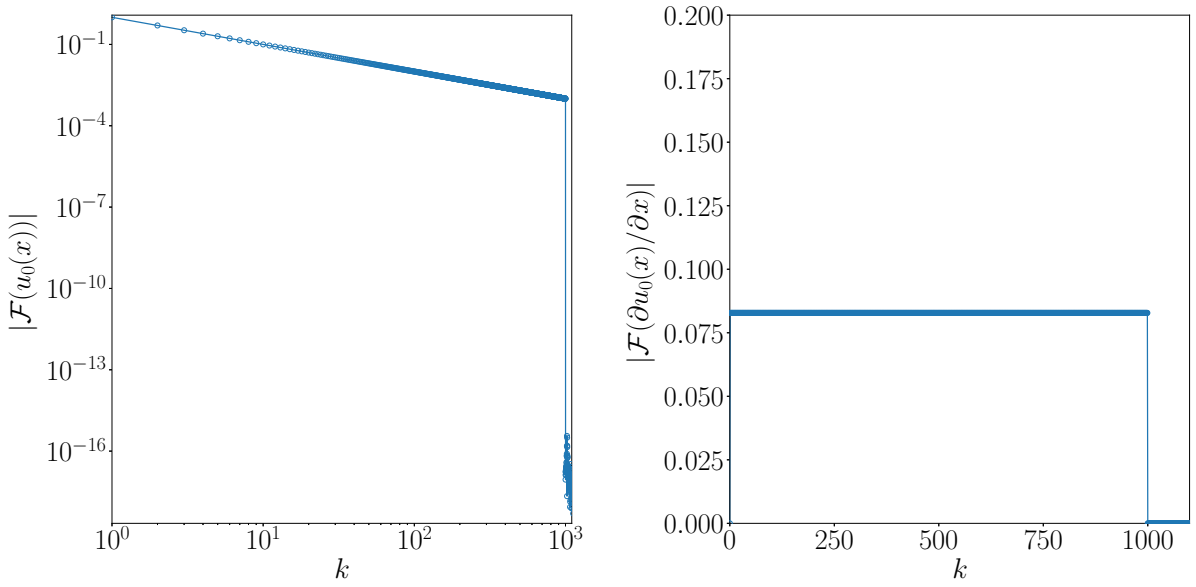

(a) $u_0(x)$ spectrum

(b) $\partial u_0(x)/\partial x$ spectrum

Figure 5.12: Initial spectra

the $\overline{E}(t) - \overline{E}_k(t)$ diagram is addressed. The paths followed barely diverge (see figure 5.15), the difference being due to the filter. In fact, the action of the filter is enhanced when considering non-ideal gases. This feature is visible from figure 5.16: the $\Delta\overline{E}_t$ doubles for a non-ideal gas. One might notice that the energy oscillations triggered by this initial condition are far more important than the ones observed in section 5.1. This behaviour was expected, since $u_0(x)$ has greater amplitude.

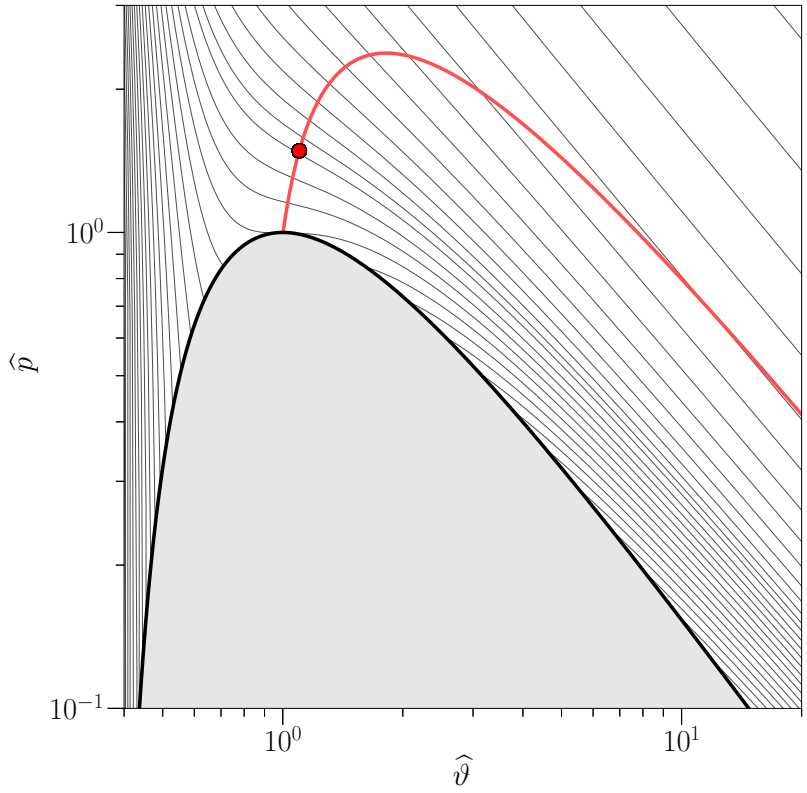

The isentropes are represented in light grey, the initial state is marked by the big red point. The red line corresponds to the iso-$\Gamma = 1$ line.

Figure 5.13: Initial state in the $\widehat{p} - \widehat{\vartheta}$ diagram

Let us draw attention to the specific-internal- and kinetic-energy oscillations: how does the ideal-gas case differ from the non-ideal-gas case? As a matter of fact, the third equation of system (5.17) states that, $\Delta\vartheta$ being the same, Δe is greater when the isentrope is steeper. We thus expect a larger Δe for the ideal-gas case. Does this imply larger oscillations of $e(x,t)$ at a given time?
At the same time, the second equation of system (5.17) can be recast as:

$$\frac{De_k}{Dt} = -\vartheta u \frac{\partial p}{\partial x} \tag{5.19}$$

and, quite similarly as before, De_k/Dt is expected to be greater when the isentrope is steeper. The *root-mean-square* is used to assess the amplitude of the oscillations in space of De_k/Dt and De/Dt at a given time, where the *rms* is defined as:

$$f_{rms}(t) = \sqrt{\frac{1}{N}\sum_{i=1}^{N}\left(f(x_i,t) - \overline{f}(t)\right)^2}, \tag{5.20}$$

N is the number of samplings and $\overline{f}(t)$ the space average. Figures 5.17 and 5.18 show the evolution in time of $(De_k/Dt)_{rms}$ and $(De/Dt)_{rms}$. Indeed, these two quantities are larger–almost at all times–in the ideal-gas case, since the isentrope is steeper. Because p sweeps a larger interval of values and $\Delta\vartheta$ is the same, the resulting specific-internal-energy derivative is greater

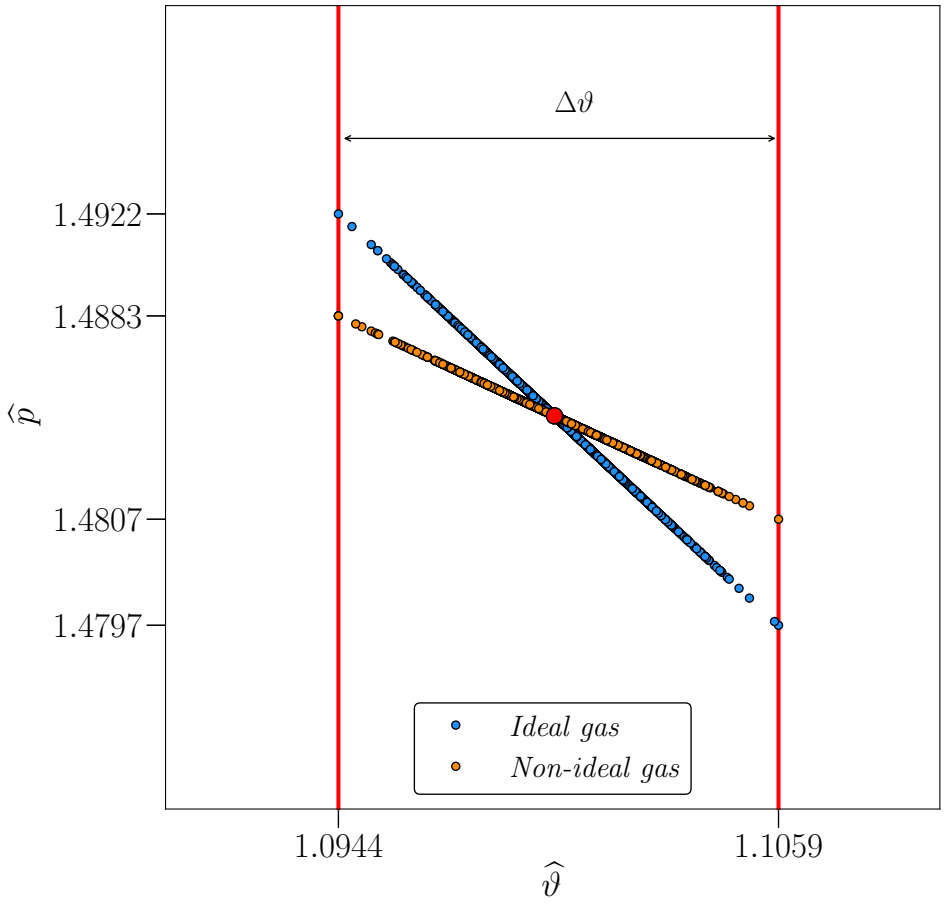

The thick red lines define the imposed $\Delta\vartheta$ at $t = \Delta t$. The big red point marks the initial state.

Figure 5.14: Thermodynamic states at $t = \Delta t$ in the $\widehat{p} - \widehat{\vartheta}$ diagram

for an ideal gas. The same reasoning applies to the specific-internal-energy derivative. But, does this imply that the internal and kinetic energy oscillate more around the mean value? As far as $e_{k,rms}$ is concerned, this is true–as figure 5.19 shows. On the contrary, when it comes to e_{rms}, the answer is no and the reason lies behind the van der Waals equation of state (see figure 5.20). In fact, the dimensionless specific internal energy is defined as:

$$e(T) = (\gamma - 1)T \tag{5.21}$$

for an ideal gas and:

$$e(T, \vartheta) = \frac{8}{3}(\gamma - 1)T - 3\vartheta \tag{5.22}$$

for a non-ideal gas. The second term on the right-hand side of equation (5.22) is accountable for the unexpected behaviour of the specific-internal-energy *rms*: although e of an ideal gas experiences more severe variations in time and despite the same initial condition, this does not translate into larger e_{rms}. Actually, it behaves in the opposite way.
Eventually, we notice that, the greater the initial speed of sound, the higher the frequency of the

oscillations; nonetheless–unlike what was observed in section 5.1–the frequency of the oscillations does not equal $2c_0$. Indeed, strong shock waves sweep the domain and the non-linear acoustics framework does not hold true.

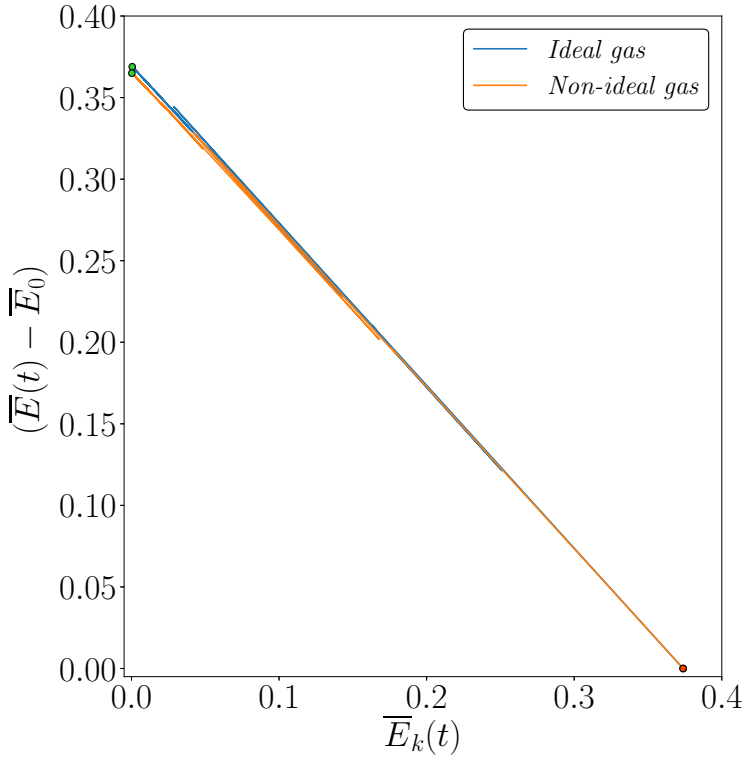

The starting point is pictured in red, the ending points in green.

Figure 5.15: Comparison of ideal and real gas: mean internal energy vs. mean kinetic energy, $t \in [0; 10]$

5.3 Viscous flows

In this section, viscous flows are addressed. In particular, the attention is drawn to the role of bulk viscosity while the shear viscosity is set to zero and the flow is adiabatic. For this particular case, the dimensionless version of the energy equations is:

$$\frac{\partial(\rho e_t)}{\partial t} + \operatorname{div}(\rho e_t \boldsymbol{u}) = -\operatorname{div}(p\boldsymbol{u}) + \frac{1}{Re_b}\left[\operatorname{div}(\boldsymbol{u}\operatorname{div}(\boldsymbol{u}))\right], \tag{5.23a}$$

$$\frac{\partial(\rho e_k)}{\partial t} + \operatorname{div}(\rho e_k \boldsymbol{u}) = -\boldsymbol{u}\cdot\operatorname{div}(p\boldsymbol{I}) + \frac{1}{Re_b}\left[\boldsymbol{u}\cdot\operatorname{grad}(\operatorname{div}(\boldsymbol{u}))\right], \tag{5.23b}$$

$$\frac{\partial(\rho e)}{\partial t} + \operatorname{div}(\rho e \boldsymbol{u}) = -p\operatorname{div}(\boldsymbol{u}) + \frac{1}{Re_b}(\operatorname{div}(\boldsymbol{u}))^2 \tag{5.23c}$$

where:

$$\mathrm{Re}_b = \frac{\rho_{ref} u_{ref} L_{ref}}{\mu_b}.$$

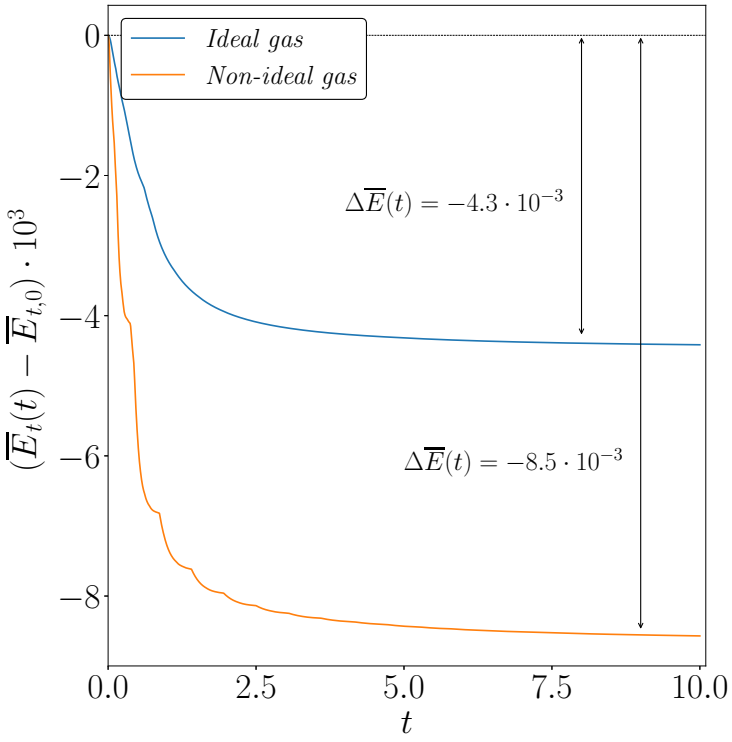

Figure 5.16: Ideal and non-ideal gas comparison: mean total energy as a function of time

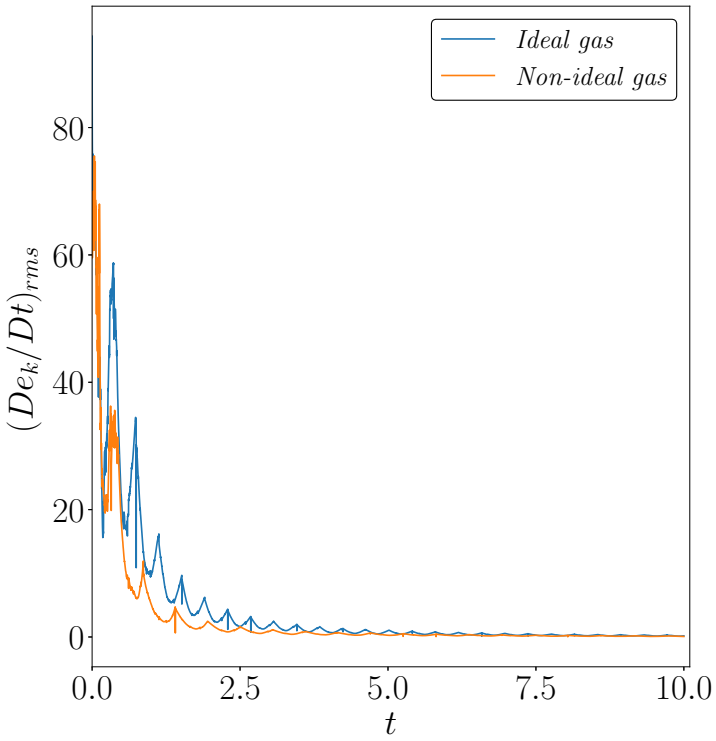

Figure 5.17: Ideal and non-ideal gas comparison: specific-kinetic-energy-derivative *rms*

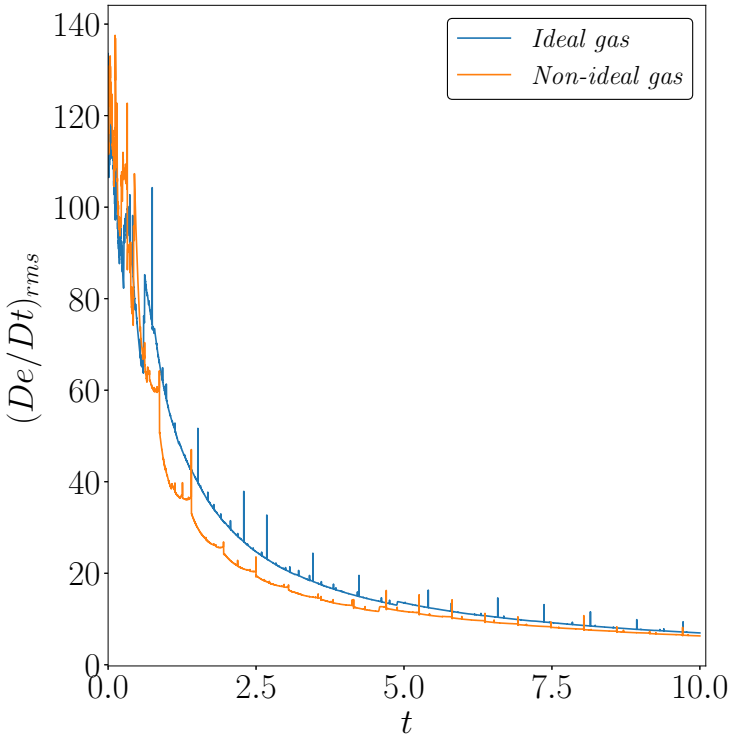

Figure 5.18: Ideal and non-ideal gas comparison: specific-internal-energy-derivative *rms*

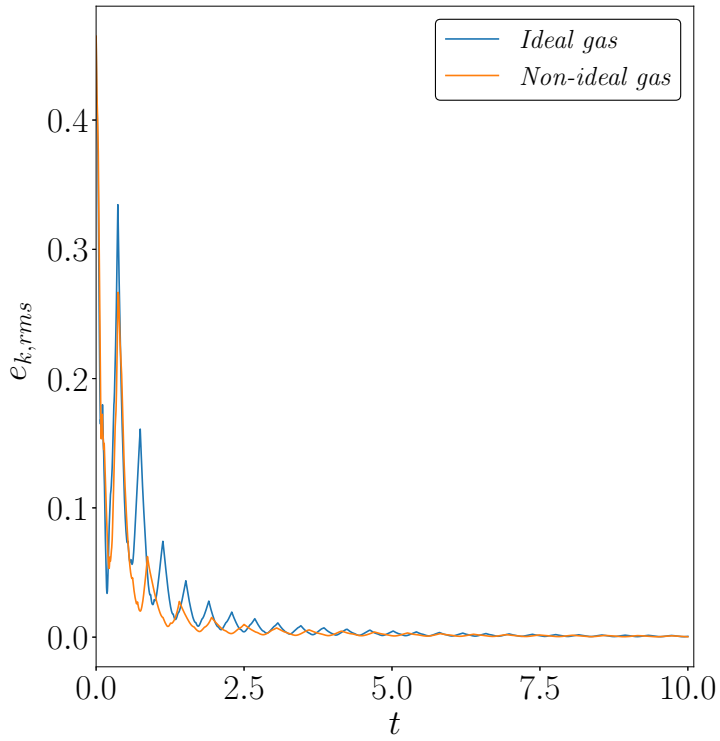

Figure 5.19: Ideal and non-ideal gas comparison: specific-kinetic-energy *rms*

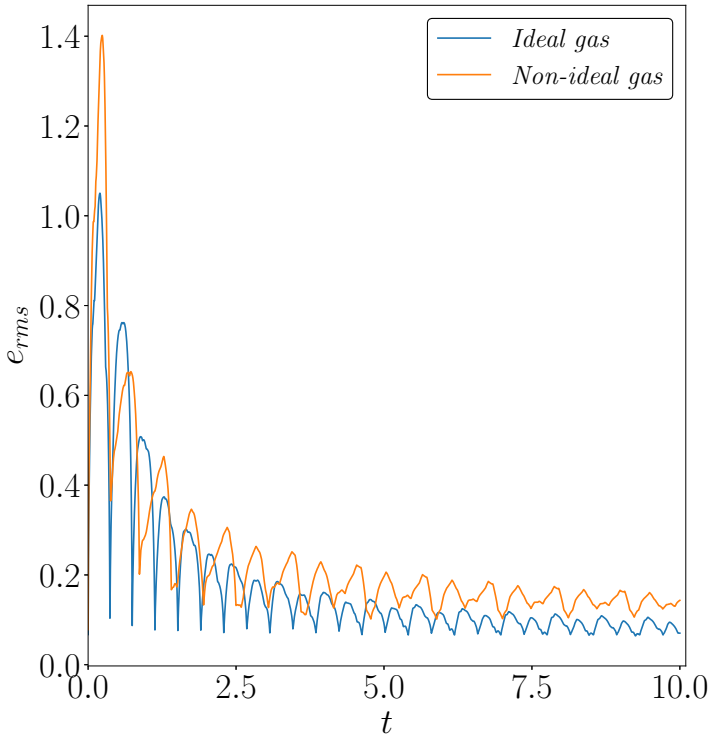

Figure 5.20: Ideal and non-ideal gas comparison: specific-internal-energy *rms*

In one dimension, the set of equations of system (5.23) is rewritten as:

$$\frac{\partial(\rho e_t)}{\partial t} + \frac{\partial}{\partial x}(\rho e_t u) = -\frac{\partial pu}{\partial x} + \frac{1}{Re_b}\left[\frac{\partial}{\partial x}\left(u\frac{\partial u}{\partial x}\right)\right], \tag{5.24a}$$

$$\frac{\partial(\rho e_k)}{\partial t} + \frac{\partial}{\partial x}(\rho e_k u) = -u\frac{\partial p}{\partial x} + \frac{1}{Re_b}\left(u\frac{\partial^2 u}{\partial x^2}\right), \tag{5.24b}$$

$$\frac{\partial(\rho e)}{\partial t} + \frac{\partial}{\partial x}(\rho e u) = -p\frac{\partial u}{\partial x} + \frac{1}{Re_b}\left(\frac{\partial u}{\partial x}\right)^2. \tag{5.24c}$$

The space average gives:

$$\frac{\partial\langle\rho e_t\rangle_x}{\partial t} = 0, \tag{5.25a}$$

$$\frac{\partial\langle\rho e_k\rangle}{\partial t} = -\langle u\frac{\partial p}{\partial x}\rangle_x + \langle\frac{1}{Re_b}u\frac{\partial^2 u}{\partial x^2}\rangle_x, \tag{5.25b}$$

$$\frac{\partial\langle\rho e\rangle_x}{\partial t} = -\langle p\frac{\partial u}{\partial x}\rangle_x + \langle\frac{1}{Re_b}\left(\frac{\partial u}{\partial x}\right)^2\rangle_x. \tag{5.25c}$$

To verify these energy balances, let us take *simulation 1B* of chapter 4–the very same case studied in section 4.3. The gas is non-ideal, while the fundamental derivative is negative and equal to

$\Gamma = -1$. A short interval of time $t \in [0; 10]$ has been chosen to better visualise the phenomena characterising the flow. Figures 5.21 and 5.22 depict the mean-kinetic- and mean-internal-energy balances for $Re_b = 10^4$. The viscous term adds up to the pressure term and together they balance out the left-hand side which accounts for the mean-internal-energy variations in time. Let us single out the mean-internal-energy balance: the viscous term–according to equation (5.25c)–is always positive. Its contribution lessens when Re_b increases, as it is shown by figure 5.23.

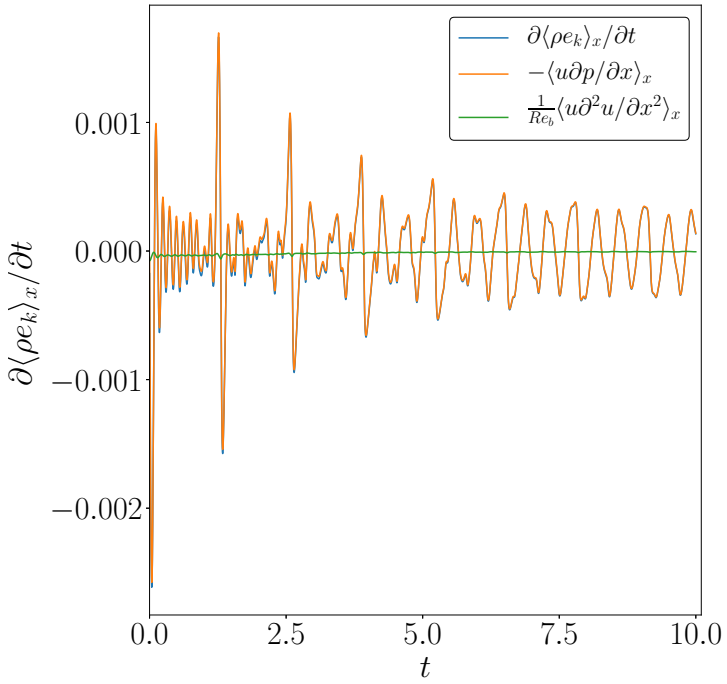

Figure 5.21: Mean-kinetic-energy balance for an ideal gas: contribution of each term

Two questions come to mind: what is the effect of bulk viscosity on the energy path and does Re_b affect the mean-kinetic- and mean-internal-energy oscillations?

Figures 5.24 and 5.25 answer to the first question. The energy paths differ because the action of the filter is enhanced at large Re_b, meaning low viscosity. The ending points are found on different total energy levels: the larger Re_b, the more it drifts downwards. Unlike section 5.1, the oscillations have not ceased yet, for a shorter time interval has been chosen. Consequently, if one let time pass, the ending points will drift towards an asymptotic position.

As far as the second question is concerned, figures 5.26 and 5.27 exhibit the impact of an increasing Re_b on the mean-kinetic- and mean-internal-energy oscillations. While the four curves slowly diverge because of the filter, the viscous term reduces the amplitude of the internal- and kinetic-energy oscillations. Indeed, let us rewrite the third equation of system (5.16) by adding the contribution of bulk viscosity:

$$\frac{De}{Dt} = -p_m \frac{D\vartheta}{Dt} \tag{5.26}$$

where p_m is the mechanical pressure defined as:

$$p_m = p - \frac{1}{Re_b}\mathrm{div}(\boldsymbol{u}) \tag{5.27}$$

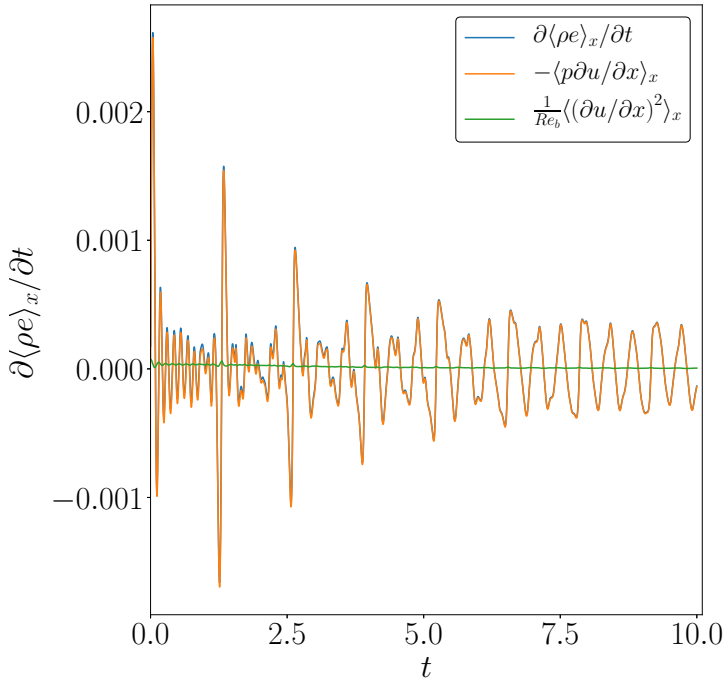

Figure 5.22: Mean-internal-energy balance for an ideal gas: contribution of each term

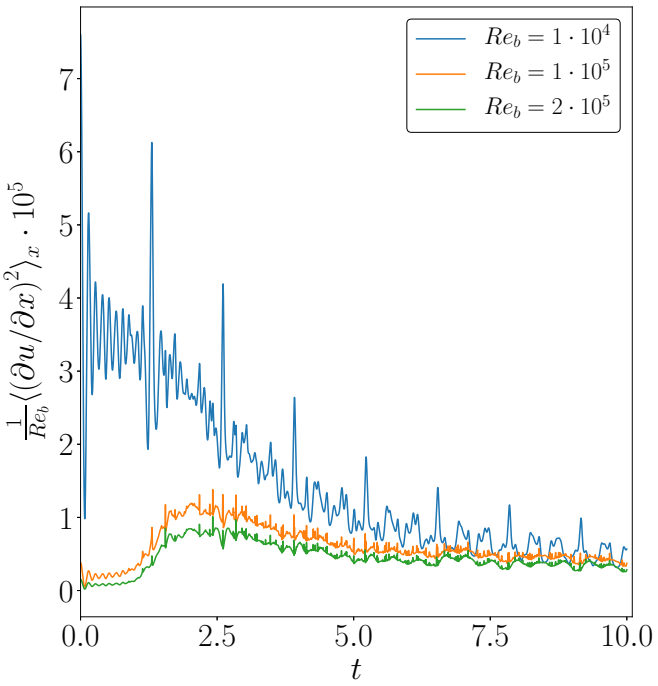

Figure 5.23: Viscous term for different values of Re_b

in one-dimension, equation (5.26) becomes:

$$\frac{De}{Dt} = \left(-p + \frac{1}{Re_b}\frac{\partial u}{\partial x}\right)\frac{D\vartheta}{Dt} \tag{5.28}$$

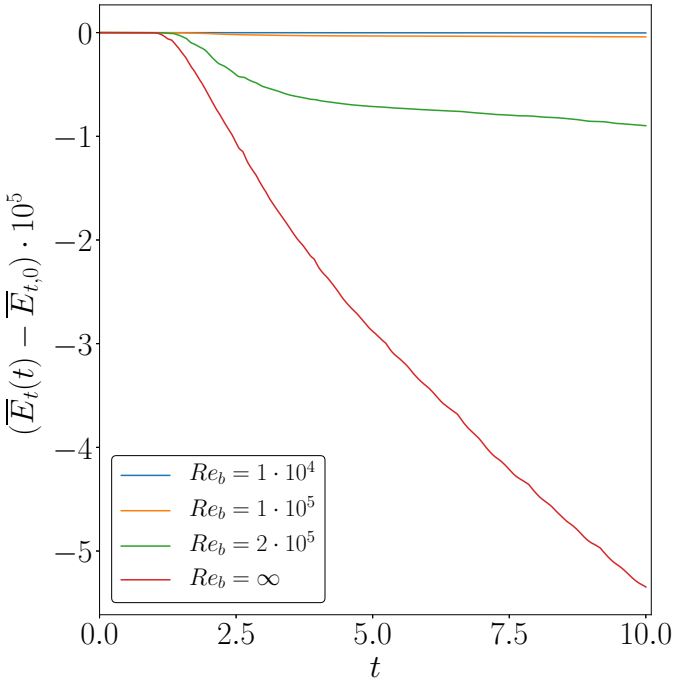

Figure 5.24: Mean-total-energy diminution in time for different values of Re_b

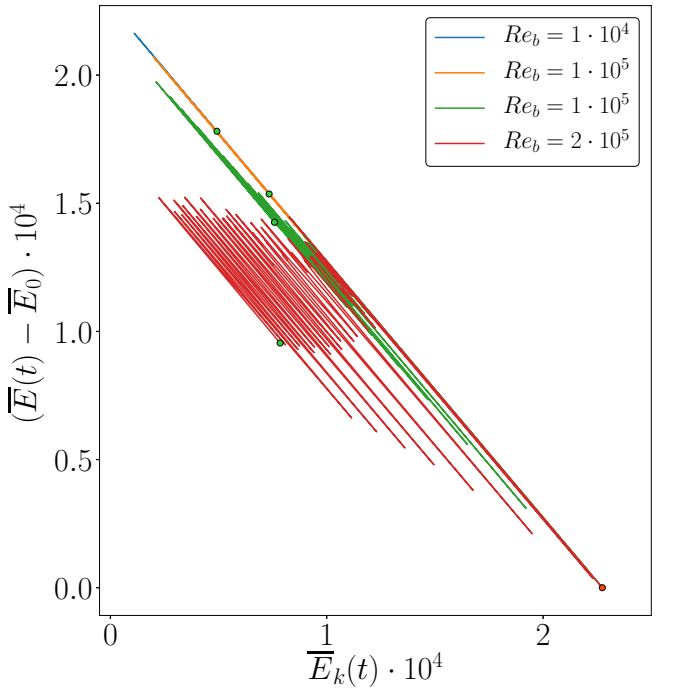

The starting point is pictured in red, the ending points in green. For the sake of better understanding, both the x and y-axes have been magnified by a 10^4 factor.

Figure 5.25: Mean internal energy vs. mean kinetic energy for different values of Re_b, $t \in [0; 10]$

The viscous term, whose contribution is always positive, and the thermodynamic pressure p add up. The oscillations triggered by a pure thermodynamic pressure are thus reduced by the bulk viscosity.

Eventually, we recall that the $x-t$ diagram showed a periodic interaction of shocks. Whenever the shock waves interact, the mean-kinetic energy experiences a local maximum. When the bulk Reynolds number decreases and the effect of viscosity is more intense (the shock waves are smoother), the local maximum will take lower values.

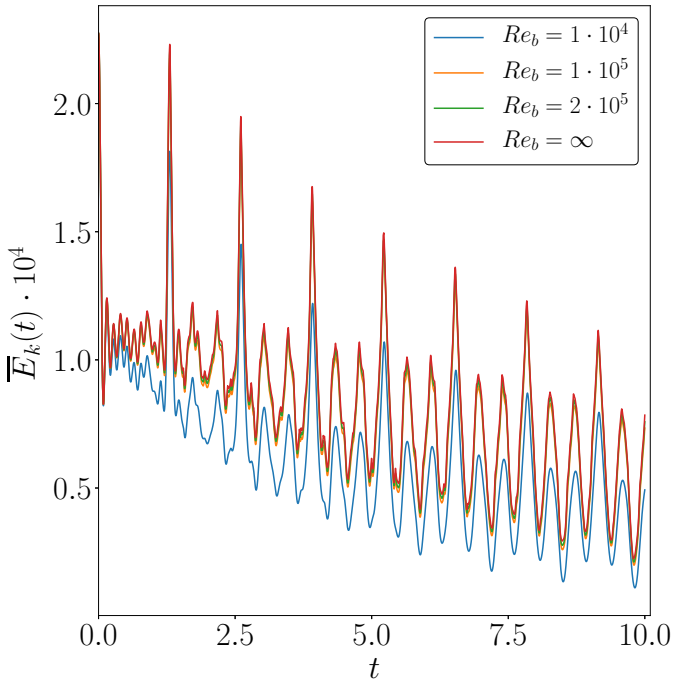

Figure 5.26: Mean kinetic energy as a function of time for different values of Re_b

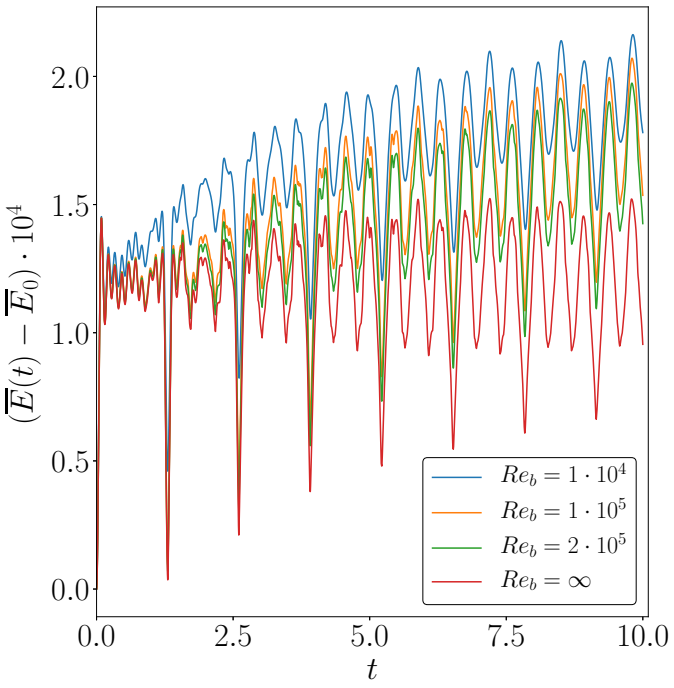

Figure 5.27: Mean internal energy as a function of time for different values of Re_b

Conclusion

This work showed different strands of one-dimensional flows of ideal and non-ideal gases. Particular emphasis was placed on the exchanges between kinetic and internal energy and the effect of bulk viscosity.

The Burgers equation provided a guideline for more complex cases if ideal or non-ideal gases were taken into account. Chapter 2 presented the main theoretical results concerning the Burgers equation. The Cole-Hopf transformation (see Hopf [2] and Cole [1]) led to a simpler heat equation whose exact solution is well-known. This allowed Burgers [3] to study the asymptotic sawtooth solution and Gotoh [5] to assess its energy spectrum, which was found to be proportional to $1/k^2$, as numerical estimations of the exact solution showed. When the value of viscosity was increased, the resulting velocity field formed smoother shock waves and the high-frequency content of the energy spectrum was filtered out. In addition, the evolution of the velocity field towards the sawtooth-shaped solution was confirmed by the phase spectrum that is equal to $\pm\pi/2$ at large times.

Chapter 3 pivoted on one-dimensional flows of ideal gases. Karpman [21] and Crighton [7] demonstrated the mapping between the one-dimensional Navier-Stokes equations and the Burgers equation under the assumption of small perturbation. After having described `Compreal` main features, initial-velocity disturbances and perturbations of the initial thermodynamic state were imposed to the flow. In both cases, the very same asymptotic solution was retrieved, namely, the aforementioned sawtooth. Therefore, the energy spectrum featured a proportionality to $1/k^2$, while the phase spectrum was found to align with $\pm\pi/2$. The mean spectrum was shown to decay as $1/t^2$.

Chapter 4 focused on non-ideal gases. Kluwick [10] proved that a mapping between the one-dimensional Navier-Stokes equations and the Burgers equation holds true for non-ideal gases and that the fundamental derivative of gasdynamics plays a major role. In fact, the velocity profile, regardless of the initial condition, was found to evolve, once more, towards the sawtooth for $|\Gamma_0| \gg 0$. When Γ_0 was imposed to be positive, compression shock waves were formed, whereas when Γ_0 was negative-valued, expansion shock waves swept the domain and the sawtooth was proven to be reversed. The energy spectrum was found to be proportional to $1/k^2$ and the mean spectrum to decay as $1/t^2$. On the other hand, when $\Gamma_0 \simeq 0$, the asymptotic solution presented both compression and expansion shock waves. Nonetheless, the spectrum remained proportional to $1/k^2$, whereas the mean spectrum did not decay as $1/t^2$ but rather as $1/t$: stronger discontinuities were found at large times.
As far as the phase spectrum is concerned, different behaviours were observed according to the initial value of the fundamental derivative: it was shown to align with $\pm\pi/2$ when Γ_0 is positive and with 0 and π when Γ_0 is negative; in contrast, for $\Gamma_0 \simeq 0$, the phase spectrum was found to be random.
Kluwick's research [10] inspired the discovery of a peculiar point in the thermodynamic diagram. Let us consider a van der Waals gas: when Γ_0 is zero, second-order terms lead to the formation of the first shock wave. Indeed, if one imposes the derivative of Γ with respect to ϑ to be null, the formation time of the first shock is delayed as much as possible. Numerical simulations performed with `Compreal` confirmed this reasoning.

The effect of bulk viscosity was investigated thereafter: it was shown to smooth out the discontinuities thus affecting the energy spectrum. High-frequency content was found to be filtered out and a greater value of μ_b to enhance this effect. The correction to the -2 exponent exhibited a strong dependency on the initial condition.

In the end, chapter 5 assessed the exchanges between kinetic and internal energy. The pressure-dilation term was proven to play a key role: in one-dimension, it causes internal- and kinetic-energy oscillations. Numerical simulations confirmed that an initial kinetic-energy perturbation triggers internal-energy oscillations and vice versa. In addition, the filter that was implemented in `Compreal` provoked a reduction of total energy, whilst it should have been conserved.
A specific input was designed thereafter in order to compare ideal and non-ideal gas behaviours. Despite having chosen a greater value of the speed of sound, the internal-energy oscillations triggered by the initial condition were less important for an ideal gas than for a non-ideal gas.
To conclude, when including bulk viscosity, the internal-energy equation can be rewritten: the mechanical pressure appears instead of the thermodynamic pressure. The internal- and kinetic-energy oscillations were found to be diminished by the bulk viscosity.

Bibliography

[1] Julian D. Cole. On a quasi-linear parabolic equation occurring in aerodynamics. *Quarterly of applied mathematics*, 9(3):225–236, 1951.

[2] E. Hopf. The partial differential equation $u_t + uu_x = \mu u_{xx}$. *Communication on Pure and Applied Mathematics*, 3(3), 1950.

[3] J. M. Burgers. *The nonlinear diffusion equation*. D. Reider Publishing Company, College Park, Maryland, 1974.

[4] S. Kida. Asymptotic properties of Burgers turbulence. *Journal of Fluid Mechanics*, 93, 1979.

[5] T. Gotoh. Statistics of decaying Burgers turbulence. *Physics of Fluids*, 5(445), 1993.

[6] Alexandre J. Chorin and Ole H. Hals. Viscosity-dependent inertial spectra of the Burgers and Korteweg– deVries–Burgers equations. *PNAS*, 102(11):3921–3923, 2005.

[7] David G. Crighton. Model equations of nonlinear acoustics. *Annual Review of Fluid Mechanics*, 11(1):11–33, 1979.

[8] D. G. Crighton and J. F. Scott. Asymptotic solutions of model equations in nonlinear acoustics. *Philosophical Transactions of the Royal Society of London A: Mathematical, Physical and Engineering Sciences*, 292(1389):101–133, 1979.

[9] I. P. Lee-Bapty and D. G. Crighton. Nonlinear wave motion governed by the modified Burgers equation. *Philosophical Transactions of the Royal Society of London A: Mathematical, Physical and Engineering Sciences*, 323(1570):173–209, 1987.

[10] A. Kluwick. *Nonlinear waves in real fluids*. Springer-Verlag Wien GMBH, Wien, Austria, 1991.

[11] A. Kluwick and E. A. Cox. Propagation of weakly nonlinear waves in stratified media having mixed nonlinearity. *Journal of Fluid Mechanics*, 244:171–185, 1992.

[12] M. S. Cramer and A. Kluwick. On the propagation of waves exhibiting both positive and negative nonlinearity. *J. Fluid Mech.*, 142, 1983.

[13] H. A. Bethe. *On the Theory of Shock Waves for an Arbitrary Equation of State*, pages 421–495. Springer New York, New York, NY, 1942.

[14] J Zeldovich. On the possibility of rarefaction shock waves. *ZHURNAL EKSPERIMENTALNOI I TEORETICHESKOI FIZIKI*, 16(4):363–364, 1946.

[15] P. A. Thompson. A fundamental derivative in gasdynamics. *The Physics of fluids*, 14(9):1843–1849, 1971.

[16] P. A. Thompson and K. C. Lambrakis. Negative shock waves. *J. Fluid Mech.*, 60:187–208, 1973.

[17] Mark S Cramer and R Sen. Shock formation in fluids having embedded regions of negative nonlinearity. *The Physics of fluids*, 29(7):2181–2191, 1986.

[18] Nicolas Alferez and Emile Touber. One-dimensional refraction properties of compression shocks in non-ideal gases. *Journal of Fluid Mechanics*, 814:185–221, 2017.

[19] A. Guardone and Argrow B. M. Nonclassical gasdynamic region of selected fluorocarbons. *Phys. Fluids*, 17:1–17, 2005.

[20] A. Guardone and Colonna P. Molecular interpretation of nonclassical gas dynamics of dense vapors under the van der Waals model. *Phys. Fluids*, 18, 2006.

[21] V. I. Karpman. *Non-linear waves in dispersive media*. Oxford, New York, 1974.

[22] W. D. Hayes. The basic theory of gasdynamic discontinuities. In H. W. Emmons, editor, *Fundamentals of Gasdynamics*, volume 3, pages 416–481. 1960.

[23] H. B. Callen. *Thermodynamics and an Introduction to Thermostatistics*. John Wiley and Sons, 1985.

[24] A. Guardone and L. Vigevano. Roe linearization for the van der Waals gas. *Journal of Computational Physics*, 175(1):50 – 78, 2002.

[25] P. A. Thompson and Lambrakis K. C. Existence of real fluids with a negative fundamental derivative γ. *Phys. Fluids*, 15:933, 1972.

[26] A. Guardone, N. R. Nannan, and P. Colonna. Critical point anomalies include expansion shock waves. *Phys. Fluids*, 26, 2014.

[27] A. Kluwick. Internal flows of dense gases. *Acta Mechanica*, 169(1):123–143, May 2004.

[28] P. A Thompson. *Compressible-fluid dynamics*. Mc Graw-Hill Book Company, 1993.

[29] Julian D. Cole. The energy spectrum of fronts: Time evolution of shocks in Burgers equation. *Journal of the Atmospheric Sciences*, 49(2):128–139, 1992.

[30] E. Touber. *Unsteadiness in shock-wave/boundary-layer interactions*. PhD thesis, University of Southampton, 2010.

[31] C. K. W. Tam and J. C. Webb. Dispersion-relation-preserving finite difference schemes for computational acoustics. *Journal of Computational Physics*, 107:262–281, 1993.

[32] C. Bogey and C. Bailly. A family of low dispersive and low dissipative explicit schemes for flow and noise computations. *Journal of Computational Physics*, 194:194–214, 2004.

[33] A. W. Cook and W. H. Cabot. A high-wavenumber viscosity for high-resolution numerical methods. *Journal of Computational Physics*, 195:594–601, 2004.

[34] S. Kawai and S.K. Lele. Localized artificial diffusivity scheme for discontinuity capturing on curvilinear meshes. *Journal of Computational Physics*, 227:9498–9526, 2008.

[35] H. Terashima, S. Kawai, and M. Koshi. Consistent numerical diffusion terms for simulating compressible multicomponent flows. *Computers & Fluids*, 88:484–495, 2013.

[36] S. Kawai, S. K. Shankar, and S. K. Lele. Assessment of localized artificial diffusivity scheme for large-eddy simulation of compressible turbulent flows. *Journal of Computational Physics*, 229(5):1739–1762, 2010.

[37] E. Johnsen, J. Larsson, A. V. Bhagatwala, W. H. Cabot, P. Moin, B. J. Olson, P. S. Rawat, S. K. Shankar, B. Sjögreen, H.C. Yee, X. Zhong, and S.K. Lele. Assessment of high-resolution methods for numerical simulations of compressible turbulence with shock waves. *Journal of Computational Physics*, 229(4):1213–1237, 2010.

[38] B. Osgood. *The Fourier Transform and its Applications.* Stanford, California, 2007.

[39] J. Bec and K. Khanin. Burgers turbulence. *Physics Reports*, 447(1-2):1–66, 2007.

[40] J. J. C. Nimmo and D. G. Crighton. Backlund transformations for nonlinear parabolic equations: the general results. In *Proceedings of the Royal Society of London A: Mathematical, Physical and Engineering Sciences*, volume 384, pages 381–401. The Royal Society, 1982.